Alma Mater Studiorum · University of Bologna

**School of Science**
**Department of Physics and Astronomy**
**Master Degree in Physics**

# RIPTIDE: a novel recoil proton track imaging detector concept

**Supervisor:**
**Prof. Cristian Massimi**

**Co-supervisor:**
**Dr. Patrizio Console Camprini**

**Submitted by:**
**Claudia Pisanti**

Academic Year 2021/2022

Pusilla res mundus est, nisi in illo, quod quaerat, omis mundus habeat.

---

*Seneca, Naturales Quaestiones*

# Abstract

A neutron detector with tracking capability is relevant in a variety of applications, spanning from environmental dosimetry to nuclear physics applications. In this thesis, the working principle and two preliminary studies for the development of a new detector for tracking fast neutrons are described. The detector consists of a plastic scintillator coupled with an optical system able to image the scintillation light generated along the path of recoil protons from elastic scatterings with neutrons. It is possible to link the length of proton tracks to the energy of incoming neutrons. In fact, the neutron energy can be reconstructed from a single elastic scattering, if the source position is given (and therefore the neutron direction). From a double elastic scattering, the neutron energy and direction can be obtained. Monte Carlo simulations of several neutron sources at different energies have been performed, and the resulting interaction have been analyzed. In addition, the signal produced by a first prototype made of a silicon photomultiplier coupled with the plastic scintillator has been studied in order to characterize the response of a light sensor while varying the wrapping material.

# Contents

# Introduction

Neutron detectors are essential tools for the development of basic and applied research.

Having no electric charge, neutrons cannot be detected via ionization. Therefore, the products of nuclear interactions, namely charged particles or electromagnetic radiation, need to be used to identify the presence of a neutron. Virtually, every type of neutron detector is a combination of a converter, whose purpose is to favor neutron reactions, and a charged particle or electromagnetic radiation detector (depending on the processes involved in the converters). Neutron-proton elastic scattering is one of the prevalent reactions used for fast neutron conversion. To date, neutron detectors can function as counters, which just give information on the number of interactions taking place in the detector, or as spectrometers, which provide data on the energy distribution of the incident radiation. The neutron's direction cannot be determined by any detector that is currently operational. In other words, proton-recoil track imaging is still at the cutting edge of neutron-detection systems, despite constant advancements in experimental techniques. More in detail, RPTI technique makes use of the recoil proton track's ability to reveal information about incident neutrons. If neutron source is known, with a single neutron-to-proton elastic scattering it is possible to reconstruct neutron energy (the direction being known); with a double neutron-proton elastic scattering it is possible to fully determine neutron momentum, even if the source position is not known.

In this thesis, the idea behind a novel recoil proton track imaging detector named RIPTIDE is described. In particular, RIPTIDE was conceived as a monolithic plastic scintillator cube coupled to three imaging devices with high photon resolution and fast response. In addition, a silicon photomultiplier is used to synchronize the three acquisition systems. Contrary to SiPM,PMT-scintillation systems, the diffused light in the scintillator represents a source of background. Therefore, to reduce image noise background, the scintillator must be wrapped with a photo-absorber material: a black aluminium foil commonly called Cinefoil. The plastic scintillator works both as a converter and as a charged particle detector: the high proton density of the scintillator enables neutron-to-proton scattering, and scintillation light is produced along the path of recoil protons, allowing its detection. Trough stereoscopic imaging, a 3D reconstruction of recoil proton tracks inside the scintillator is made possible. This configuration enables particle discrimination, a necessary prerequisite for neutron detection.

Different fields of applications could benefit from the availability of a detector with tracking capability. Because it should be able to detect neutrons in real time, it could be used as environmental control system in the facilities that require neutron dosimetry, mainly nuclear reactors and ion beam therapy centers. Its compact size would make it suitable for applications in space: they could be used for spaceships dose monitoring and study of solar neutrons. Moreover, these apparatuses might be incorporated to nuclear physics experiments that requires neutron detectors, as FOOT or n_TOF.

After a general overview of the possible applications in Chapter 1, and of the state of the art in Chapter 2; the RIPTIDE detector is presented in Chapter 3. Finally, Chapter 4 investigates neutron interaction inside the scintillator to establish the probabilities of neutron single and double scattering inside the scintillator, and Chapter 5 a characterization of the coupling of a silicon photomultiplier with the scintillator is provided.

# Chapter 1

# Scientific motivations

The construction of a neutron detector with tracking capability similar to RIPTIDE could play an important role in several fields of particle physics research and applications.

One of the fields that could benefit most from the construction of these kinds of detectors is ion beam therapy.

## 1.1 Ion beam therapy

In general, in radiotherapy techniques for cancer treatments, an amount of radiation ($\gamma$-rays, electrons or heavy ions) is delivered to the patient with the purpose of stopping the reproduction of cancer cells. However, during the treatment, especially in conventional radiotherapy (with $\gamma$-rays), a large portion or the whole patient body is exposed to radiation. This exposure could generate secondary radio-induced tumors. For this reason, many of current researches in this area concentrates on how to expose cancer while reducing the dose provided to healthy tissues.

Ion beam therapy is a relatively recent technique of cancer treatment that implies the use of fully ionized ions (protons and heavier ions up to $^{12}C$). The main feature of these heavy ions is to release the most of their energy at the end of their path (see figure 1.1). This allows to localize the radiation release in the cancer region. This technique is generally called hadrontherapy. So far, mainly carbon ions and more often protons are used for this kind of treatment. When based on protons, hadrontherapy is referred as proton therapy. In hadrontherapy, particle energies range between 200 and 400 MeV

This technique is mainly used for the treatment of deep-seated tumors or of tumors that are near organs at risk (OAR). In these cases, hadrontherapy is preferred to conventional radiotherapy for its ability of making a targetted and localized treatment.

In addition to decreasing the damage caused to the patient's healthy tissues, these new techniques showed higher efficacies on the local control rate[1] of several types of

[1]It is a parameter conventionally used in radiotherapy that gives information on the number of cases

cancer. A relevant example is Chondrosarcoma, whose control passed from 33% using radiotherapy to 88% when hadrons (both protons or carbon ions) are used [30].

## Hadrontherapy: principle of operation

The idea behind hadrontherapy is that of exploiting a particular behaviour of electromagnetic interactions of heavy charged particles with matter (the so-called Bragg curve) to increase dose deposition in the cancer and limit healthy tissues exposure to radiation[2].

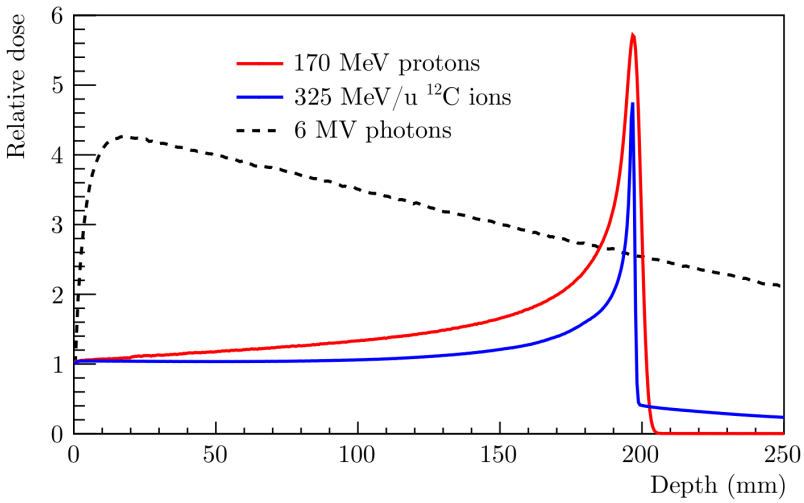


Figure 1.1: Depth-dose profiles of 6 MV photons (black dashed line), 170 MeV protons (red line) and 325 MeV/u carbon ions (blue line) in water. Differently than photons, whose dose deposition is higher at skin surface, ions release the most part of the dose at the end of the path. However, in the graph it is possible to see a tail beyond the carbon ion peak. It is due to projectile fragmentation (see Section 1.1.1) [52].

The most important information[3] that can be noticed from figure 1.1 is that the majority of the dose is released to the patient at the end of the path, and the tissue before and after the peak is preserved from excessive dose exposure. On the other hand, if we consider photon interaction with matter, the maximum of the deposited dose is located at the skin entrance followed by an exponential decline. In the treatment of deep tumoral masses, therefore, conventional radiotherapy implies an high amount of dose deposition to the healthy tissues.

in which the treatment was able to limit the reproductive capability of tumoral cells. In other words, it is an indication on whether the tumor is under control.

[2]The curve gets its name from sir William Henry Bragg, who discovered it in 1903.

[3]In order to not burden the discussion, the analysis and further considerations on Bragg peak has been included in the appendix A.

Moreover, the dose of protons released beyond the peak decreases sharply and quickly reaches the zero. In other words, after the peak, there is no dose deposited, and everything that is beyond the peak is safe from radiation. This aspect is particularly useful for the treatment of cancers that lay in the proximity of vital organs, the so-called Organs At Risk. In the spinal chord irradiation, for example, ion beam therapy allows one to concentrate the treatment on the spinal chord itself with small effects to the organs inside the rib cage (heath, lungs, etc.).

Another important characteristic of charged particle-matter interaction is that the depth that the beam travels across the matter, and thus the position of the dose peak, is related to the beam initial energy. Therefore, by changing the beam energy, it is also possible to change the beam penetration and deposit.

To appreciate more the capacity of hadrontherapy of reducing damage on the patient healthy tissues, we show an image of dose deposition in a cranio-spinal irradiation case (figure 1.2) made with conventional radiotherapy and proton therapy. The treatment with protons (on the left) is clearly more localized with respect to the treatment with photons (right): protons are strictly localized in the treatment region (e.g. the spine) while, differently than in radiotherapy, the region behind the peak (the organs of the rib cage) is kept practically unharmed.

### 1.1.1 Fragmentation

Although Coulomb collisions are dominant in hadrontherapy, they are not the unique kind of interaction that happens when charged particles traverse human body. In addition, nuclear interactions can take place as well.

In the energy region considered in hadrontherapy, nucleus-nucleus interactions could be elastic or inelastic. Elastic interactions on primary particles result in a modification of direction and beam energy. In other words, reaction products are the same as reagents. On the other hand, the effect of inelastic collisions is the change of the primary particles into smaller fragments. The energies involved in hadrontherapy are high enough to break apart the nucleus in its components (proton, neutrons and heavier fragments) but are too low to fractionate the nucleons (protons and neutrons must be considered as indivisible particles at this energies). The fractionation phenomenon, thus, only concerns nuclei with A $>$ 1, for example carbon and oxygen in human body. The same happens for the nuclei used as projectiles: beam fragmentation cannot take place with proton beam, while it occurs in the case where heavier-ions are used (e.g. $^{12}C$). It worth recalling that fragmentation of beam particles causes the tail after the Bragg peak in figure 1.1: these fragments are produced with directions and velocities comparable with that of projectiles and for this reason they overstep the peak and cause a dose release beyond. The most frequent nuclear reactions are peripheral collisions and are commonly described by the

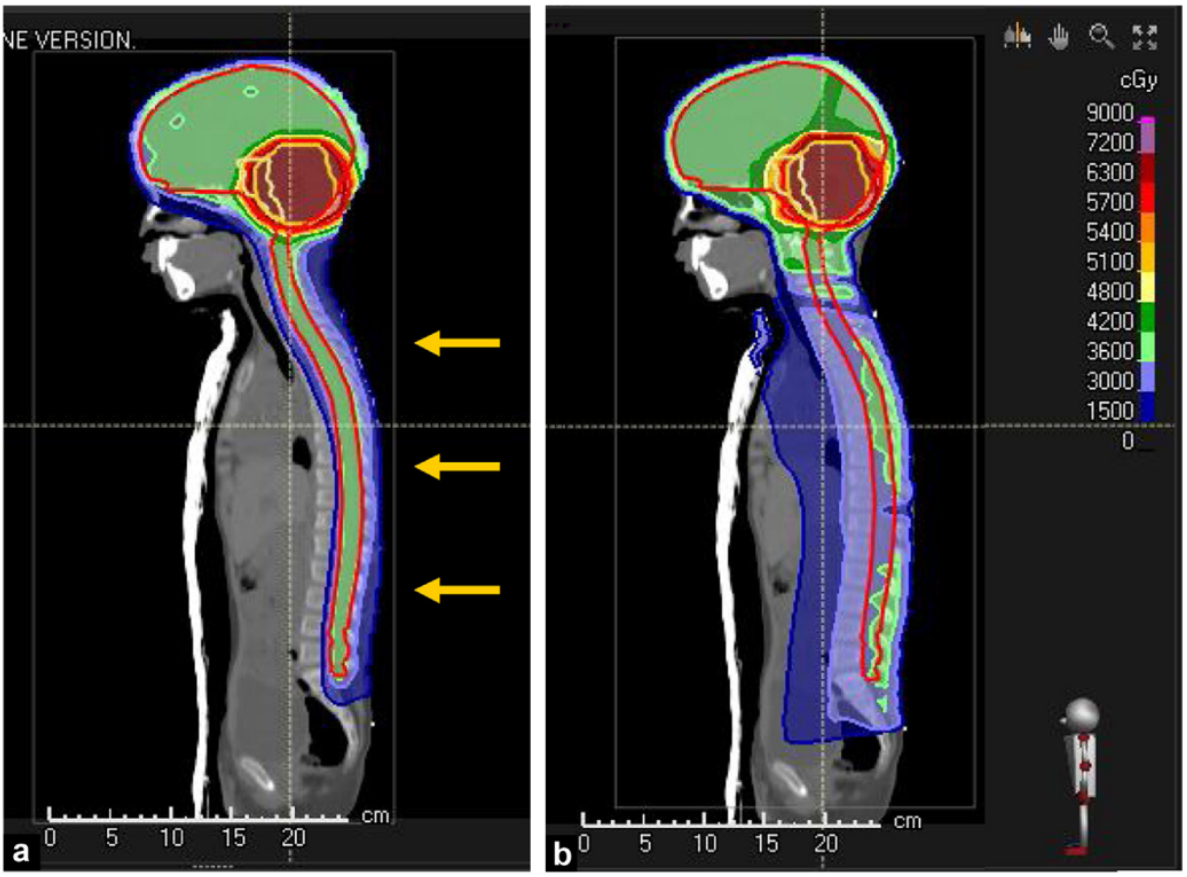


Figure 1.2: Comparison of radiotherapy (right) and proton therapy (left) dose deposition for a cranio-spinal irradiation. In the pediatric case that is shown in figure, it is a common practice to irradiate all the spinal chord to destroy all cancer cells with its possible metastasis. This is done in order to increase the chance of survival [13].

*abrasion-ablation model*[4].

A sketch of this model is provided in figure 1.3. In the model the target is initially at rest. Due to electromagnetic repulsion among the nuclei, the interaction is often peripheral. Fragmentation process can be divided in two steps.

In the first step, nucleons are abraded and form the hot reaction zone (fireball). Three fragments are produced: target fragments, projectile fragments ad the fireball. Because the projectile has an initial speed different from zero, projectile fragments are produced with a speed directed forward, while target fragments are produced almost at rest. The fragment called fireball is made of the nucleons nearby the impact position. Being closer to the impact region, these nucleons are more energetic than the other two

[4]The idea of peripheral collision and its model has been first described by Robert Serber in 1947 [57]

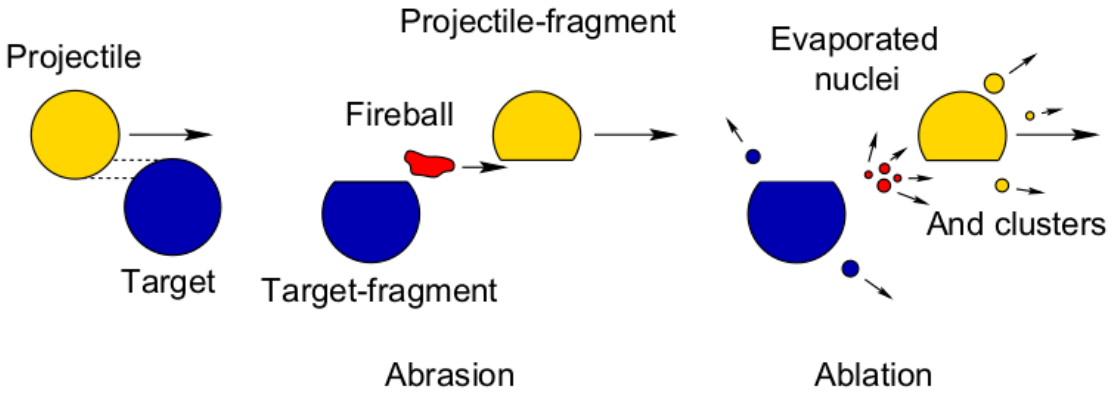


Figure 1.3: Abrasion-ablation model. In this model, ions interaction is described in two steps: first, in the abrasion the two particles interact peripherally (due to charge repulsion) with the production of a hot zone (fireball, created at the contact point. Then, the fragments thus produced (projectile fragments, target fragments and the fireball) de-excite with the emission of nucleons or small ions (evaporation) [24].

fragments. All three fragments are in an excited state. In the second step (ablation), the projectile and target fragments as well as the fireball de-excite with the resulting production of evaporated nucleons and light clusters. Those, emitted from the projectile fragments appear forward peaked in the laboratory frame. The projectile-like fragments continue travelling with nearly the same velocity and direction, and contribute to the dose deposition until they are completely slowed down or undergo further nuclear reactions. Neutrons and cluster from target-like fragments are emitted isotropically and with much lower velocities. The particles ablated from the fireball have a range which is in between the projectile and target fragments one. Nuclear fragmentation reactions lead to an attenuation of the primary beam flux and cause the production of lower-Z fragments with increased penetration depth. The lower-Z fragments have longer ranges than the primary ions because the range of particles (at the same velocity) scales with $A/Z^2$. Therefore, the depth-dose profile of heavy-ions beams shows a characteristic fragment tail beyond the Bragg peak [24].

Those secondary fragments contribute to the overall beam dose deposition. A thorough study on produced fragments (i.e. a study of the cross sections of the different interactions) is necessary to correct and eventually reduce unnecessary dose to the patient.

We already saw that projectile fragmentation is responsible for the dose deposited after Bragg peak, while target fragmentation has shorter ranges, remaining localized near the place where nuclear interactions occur. If those fragments are produced in a cancer cell, they contribute to its death. Conversely, if they are produced far from Bragg peak,

they could cause cell death of healthy tissues. It has been estimated [60] that target fragments contribute to approximately 10% of biological effect at the entrance channel, while this contribution fall to 2% when approaching Bragg peak. Finally, neutrons produced in the fragmentation process can travel longer distances and deposit the dose outside the planned target volume.

Multiple studies of beam-projectiles characteristics have been carried out, while we have almost no information of target fragmentation production. An estimation of neutron production has been made, for example, for carbon ion beam therapy [24]. In the article, it has been calculated that the dose deposited in the organs by neutrons is up to 955 mSv for 400 MeV/u C-ions and has the real potential to cause new cancers in the patient.

### 1.1.2 FOOT experiment

FOOT experiment aims to obtain cross-section measurements related to target fragmentation due to beam-targets interactions. In particular, the objective is to estimate with high accuracy which and how many fragments are produced in the interaction of protons with human body [6].

The basic principle of FOOT is similar to that of many cross section measurements: a particle beam is set against a target of a specific material, and, a series of detectors placed around the interaction point detect the particles produced.

The novelty brought by FOOT, however, is to be able to detect target fragments with low energy. The problem of their low range is overcome in FOOT by exploiting inverse kinematics. For instance, instead of studying the outcome of the interaction of a proton beam with a carbon target, it studies the outcome of a carbon beam on a proton target.

A further complication on this study lies in the impracticability of using pure hydrogen targets ($H_2$) due to the fact that it is gaseous at room temperature (it evaporates at $-252°$) and due to its high reactivity. This problem is solved exploiting cross section additive property: the cross section of a specific reaction (e.g. elastic scattering of protons with water $\sigma_{elastic}(p + H_2O)$) can be obtained by adding of the cross sections if its components ($\sigma_{elastic}(p + O) + 2\sigma_{elastic}(p + p)$). In the same way, if the cross sections of a reaction with a molecule is known, it is possible to obtain the cross section of one of the composing elements by subtraction:

$$\sigma_{elastic}(p + p) = \frac{1}{2}[\sigma_{elastic}(H_2O) - \sigma_{elastic}(O)]. \tag{1.1}$$

Therefore, for each interaction under study (e.g. $^{16}O$, $^{12}C$, etc.), measurements are performed twice: at first with a graphite target, solely composed of carbon atoms, and then with polyethylene, a plastic material uniquely made of carbon and hydrogen.

FOOT was designed for the study of charged particles. As mentioned previously, typical products of the fragmentation are also neutrons. A relevant upgrade of the

FOOT detection system would be obtained by complementing the setup with neutron detectors, possibly with tracking capability, as for example RIPTIDE (see Chapter 3 for details).

### 1.1.3 Real time dose monitoring

Another field in which neutron detectors similar to RIPTIDE could be used in ion beam therapy is that of beam monitoring.

Due to its high spatial accuracy, it is necessary, during the treatment, to be sure that Bragg peak is inside cancer region. Even millimetric displacements due to patient movement or breath or hearth beating should be taken into consideration in order to correctly positioning the beam inside human body. For this reason, it is necessary to include in the design and the construction of these irradiation machines one or more online irradiation control systems that could verify in real-time position of the beam.

One of the possible control systems under study is to use a Positron Emission Tomography system (PET). It is well known that, among the products of nuclear fragmentations, radioactive nuclei as $^{10}C$, $^{11}C$ from $^{12}C$ or $^{15}O$ from $^{16}O$ can be found. These fragments are unstable and decay with the production of a positron $\beta^+$ which, in turn, reacts with an electron annihilating with the production of two photons back to back with an energy of 511 keV.

The detection of these photons with a PET system allows one to estimate the position of the annihilation and therefore, the position of the production of the radioactive fragments and thus the position of the beam [34].

We already know that common products of nuclear fragmentation are neutrons. Therefore, a device able to detect them in real-time could be considered as an alternative or concurrent device for the monitoring of beam position.

### 1.1.4 Stray radiation dosimetry

RIPTIDE could be used for the evaluation of beam line stray radiation, i.e. the radiation that is produced in the interaction of the high energetic particle beam and the different components of the device (particle accelerator and beam delivery apparatus). The large dimension of ion beam therapy facilities require more efforts in the evaluation and shielding of stray radiation. Also in this case, fast neutrons, due to their high penetrability, must be taken in great consideration when radio-protection evaluation of the site is performed. RIPTIDE detector could be used also for this purpose.

## 1.2 Environmental radioprotection

Neutron detection is not only necessary in ion beam therapy facilities: highly energetic neutrons can be also found in cosmic rays and in the proximity of fission reactors.

### 1.2.1 Nuclear reactors

One of the most abundant artificial sources of neutrons are fission and fusion reactors [3].

In these facilities, a net amount of neutrons is produced. Some of them are shielded by the so called biological shielding, mainly made of concrete or water, some of them escape the shielding and contribute to the increment of the environmental dose. It is, thus, essential to monitor the environmental dose in the proximity of a nuclear reactor in order to protect facility workers and to promptly detect the presence of possible radiation leakages. RIPTIDE detector could be used for fast neutrons environmental control in these facilities.

### 1.2.2 Radioprotection in space

Cosmic neutrons dose gets non negligible at altitudes higher than 10 km. Thus, the estimate of this kind of radiation is important for people and electronic devices at that altitudes: airplane workers (pilots, hostesses and stuarts) and mostly astronauts.

One of the major impediments to spatial explorations is the lack of an adequate shielding to protect astronauts from the elevate doses of space radiation. Typical energies representing particles in space are peaked at about 700 MeV/u, much higher than the energies involved in hadrontherapy. There are three main sources of energetic particle in space.

- Solar particle events, produced by the Sun in coronal mass ejections, and solar flares, whose energy could reach energies of the order of GeV. The dose produced by these events is unpredictable and depends on solar activity (see chap 1.3).
- Galactic cosmic rays. They originate from supernovae explosions and they are mainly composed of atomic nuclei lighter than $^{56}Fe$ and with energies of 100-800 MeV/u.
- Finally, geomagnetically trapped particles: protons and electrons confined in Van Allen belts, a space region in which the electromagnetic field produced by the Earth trap charged particles coming from space.

The study of fragmentation products (with FOOT experiment, and thus with the use of RIPTIDE for neutron products of fragmentation) acquires a fundamental role in the

study of space radiation interaction with spaceship shieldings and internal components. When these highly energetic particles impinge into the nuclei of the spaceship, they could produce secondary fragments (including neutrons) that need to be considered for astronauts radio-protection studies. Moreover, as in the case of solar flares, also neutrons are produced (see next session). RIPTIDE small size made this detector usable also in spaceships.

## 1.3 Study of solar flares and solar neutrons

Another research area that could benefit from the development of neutron tracking detectors is the study of energetic particles produced by the sun.

The structure of the Sun and its energy and heat generation creates convective motions in the plasma of which it is composed. Plasma is the state of matter in which the temperature is so high that all electrons and positive ions are separated. Being constituted of charged particles, plasma rotation generates a magnetic field. This solar magnetic field and its variation are the cause of solar activity.

Solar activity phenomena are produced when oppositely directed magnetic field lines reconnect [5]. Surplus magnetic energy produced in the reconnection is transferred to solar particles that are able to escape from Sun gravity. Of course, Maxwell equations tell us that all the magnetic lines are always closed ($\vec{\nabla} \cdot \vec{B} = 0$). However, to modelize solar magnetic field, it is usual to talk about open field lines for the field lines that can conduct charged particles out from the Sun. These fiels lines are closed too but are driven far from the surface by coronal mass ejections or solar wind.

On closed magnetic loops, electron Bremstrahlung produces X-rays, which is seen from Earth as *solar flares*, on open field lines, *jets* can release electrons and ions into space (solar energetic particles (SEP) events). The energy of these expelled particles ranges from 10 keV to relativistic energies of several GeV and consists mainly of electrons, protons and light ions.

Magnetic reconnection can also lead to the ejection of large quantities of mass ($10^{14} - 10^{16}$ g), called coronal mass ejections (CME) [51].

From nuclear interactions of solar energetic particles thus spawned and the solar corona, various particles are produced, including neutrons. Being uncharged, neutrons clearly are not affected by the solar magnetic field and do escape more easily from the Sun, being able to reach the Earth. Neutrons produced in this way have been observed directly in space with energies ranging between 50 and 300 MeV.

After a half-life of 918 s, neutrons decay into a proton, an electron and an antineutrino

$$n \rightarrow p + e^{-} + \bar{\nu_e}$$

[5] "Don't cross the streams!" [53]

Approximately 70% of neutrons decay in the passage from the Sun to Earth. Even these neutron-decayed protons with energies of 5-200 MeV have been detected.

Therefore, solar escaped neutrons can be detected both in a direct (effective detection of neutrons) and indirect way (detection of a neutron-decayed proton).

Recoil Proton Track Imaging (RPTI) based detectors could be exploited to detect solar neutrons in a direct way. SONTRAC [7] (SOlar Neutron TRACking), for example, has been specifically developed for the detection of these particles. This detector has been designed to operate at the energy ranges of these astroparticles (20-250 MeV). Additionally, because to its compact size, this detector can be used in spaceships. Also RIPTIDE could be used for this purpose.

## 1.4 n_TOF facility upgrade

The n_TOF facility at CERN [46] has been developed to study neutron-nucleus interactions. It is able to work with a remarkably large span of neutron kinetic energies: from few meV to several GeV. Neutron cross section measurements are performed exploiting the time-of-flight method.

At the n_TOF facility, a pulsed neutron beam is generated via proton-induced spallation on a massive lead target. Initially, fast neutrons are moderated by a water slab in order to obtain the wide energy spectrum. Neutrons are collimated through the experimental areas, situated 185 m and 19 m respectively, (far enough to measure time-of-flight) from the spallation target. Finally, reaction products of the neutron-induced reactions on a target are identified by a set of dedicated detectors. In this way it is possible to find reaction probabilities as a function of incident neutron energy.

Recently, a proposal for the measurement of neutron-neutron scattering length was submitted [38]. This measurement is of interest for the determination of the magnitude of charge-symmetry breaking. The feasibility of the experiment critically depends on the availability of a neutron detector with tracking capability such as RIPTIDE.

# Chapter 2

# State of the art

The aim of this chapter is to provide an overview of the state of the art of neutron detectors, in order to highlight the novel configuration proposed with RIPTIDE.

## 2.1 Neutron detectors

The late discovery of neutrons (in 1932 by Chadwick [9]) is an indication of their detection complexity: it occurred thirteen years after the discovery of protons (1919) and thirty-five years after that of electrons (1897).

The design and construction of detectors for neutrons is complicated by their absence of electric charge. For instance, a simple ionization chamber, that exploits electromagnetic processes for charged particle detection, cannot detect them directly. Instead, neutrons can be detected only indirectly through the production of charged particles (or electromagnetic radiation) via nuclear reactions. In summary, neutron detectors involves the combination of a converter and a charged particle detector, as in the pioneering experiment by Chadwick. A variety of different reactions are used for neutron to charged particle conversion. The most used ones are presented in the following section. Since neutrons interact differently with matter at different energies, the design of the detector must consider also the energy range of the neutron.

Generally, neutron detectors can work as counters, i.e. they only indicate the number of interactions occurring in the detector, or as spectrometers and yield information about the energy distribution of the incident radiation. Recoil proton track imaging is an innovative technique that aims to determine also neutron direction. It will be described exhaustively in Section 2.2.

### 2.1.1 Neutron detection mechanisms

Neutrons are conventionally classified by their energies as thermal (with energy near 0.025 eV), epithermal (whose energies range from 0.025 eV to 1 keV), slow (from 1 keV to 100 keV), fast (between 100 keV and 20 MeV) and relativistic (with an energy larger than 20 MeV) [31]. In the epithermal region, reaction cross sections exhibit a particular feature known as resonances, and therefore this energy interval is also referred to resonance region.

Another common method to describe neutron detection mechanisms is to divide them into two broad categories: fast neutrons, having energies larger than 0.4 eV, and slow neutrons with energies lower than this value. The threshold for this discrimination is conventionally set as the value where the abrupt drop in absorption cross section of Cadmium is (called cadmium cut-off energy). Alternatively, the threshold energy is sometimes set to a few tens of keV (i.e. the threshold is conventionally set depending on the context).

Slow neutrons can either interact via elastic scattering or can undergo neutron-induced reactions. Slow neutron elastic scattering cannot be used for detection because the kinetic energy transferred to the recoil nuclei is too low. These interactions have, however, a fundamental role in slowing neutrons down to the thermal region (<0.025 eV) where radiative capture reactions are more probable.

In elastic scattering, part of the kinetic energy of neutrons is transferred to the recoil nuclei. That means that, after each interaction, neutrons lose energy and are thereby moderated by the medium. For each scattering with a generic nucleus with mass number A, it is possible to estimate the final energy of the neutron after the scattering. For an initial neutron energy equal to $E_0$, the neutron energy is expected to be [33]:

$$\left(\frac{A-1}{A+1}\right)^2 E_0 < E < E_0. \tag{2.1}$$

Therefore, if a neutron elastically scatters a proton, it could potentially lose all its energy ($0 < \mathrm{E} < E_0$), while hitting heavier nuclei, its energy after the scattering is higher than $\left(\frac{A-1}{A+1}\right)^2 E_0$. For instance, in the case of $^{12}C$ (A = 12), neutron energy after one elastic scattering will be in the range of $0.72\ \mathrm{E_0} < \mathrm{E} < \mathrm{E_0}$. This clearly suggests that the best neutron moderator is hydrogen (A = 1).

If neutron energy is sufficiently high, inelastic scattering can also take place. In this case, recoil nuclei are left in an excited state, and quickly de-excite with the production of $\gamma$-rays. These photons are an unwanted complication for the construction of detectors based on elastic scattering [29]. We now briefly describe the main interactions mechanisms exploited for the detection of neutrons [49].

**Exoergic reactions.** The word exoergic is used to define the case in which the mass of the reagents is higher than the mass of the products. That means that the reaction is spontaneous and some energy is released by the reaction. In other words: the Q-value is positive. One of the most used reaction for neutron detection is:

$$n + {}^{10}\mathrm{B} \rightarrow {}^{7}\mathrm{Li} + {}^{4}\mathrm{He} + \gamma$$

The neutron detector can be based either on the detection of the $\alpha$-particle or the $\gamma$-ray (with $\mathrm{E}_\gamma = 480$ keV). Boron is typically used for its relatively large cross section, falling as $1/v$. It is used mostly as a slow neutron detector. Other commonly used reactions with positive Q-value and large cross section are $^{6}$Li(n,$\alpha$) and $^{3}$He(n,p).

**Radiative capture.** Typically (n,$\gamma$) reactions feature a positive Q-value, and the cross section can be very high in some cases. For instance, one of the most used reaction of this type is:

$$n + {}^{157}\mathrm{Gd} \rightarrow {}^{158}\mathrm{Gd} + \gamma$$

the cross section at thermal being $2.4 \times 10^5$ barn. In addition, (n,$\gamma$) cross sections present resonances, this phenomenon can be seen at resonance condition. Depending on the atom used, it can be specific to different energy ranges.

**Fission nuclear reaction.** This mechanism exploits the characteristics of fissile materials: they are atoms that, when interact with neutrons, undergo fission. Fission products have high Z, and can be easily detected. Depending on the fissile nucleus used, it is possible to detect both fast and slow neutrons. Fissile materials, in which thermal neutrons induce fission, are $^{235}$U, $^{233}$U and $^{239}$U, while fissionable materials, that have a threshold for the reaction $\geq 400$ keV, are $^{232}$Th, $^{234}$U, $^{236}$U, $^{238}$U, $^{237}$Np and others.

Detectors based on fission have the advantage of being insensitive to $\gamma$-rays, so that they can be used in environments with intense $\gamma$-ray fluxes. Their drawback is related to $\alpha$-radiactivity of the source: it is dangerous, and in some cases it could also invalidate the detection efficiency.

**Elastic neutron scattering.** Finally, elastic neutron scattering is the most significant conversion process used for fast neutron detection. In this process (with Q-value=0), an incident neutron transfers part of its kinetic energy to a nucleus, giving rise to a recoil nucleus. Elastic scattering takes place also at low neutron energies, but typically the energy transferred in the scattering is too low to be detected. At higher energies, above the keV, recoil nuclei energy can be detected. Hydrogen is preferred as a target for

two main reasons. (1) neutron-proton cross section is relatively large and (2) incident neutrons can transfer up to all their kinetic energy to the recoil proton (see eq. 2.1). Therefore, recoil protons are relatively easy to detect, and most important, RIPTIDE is based on this detection mechanism.

### 2.1.2 Neutron detectors classification

Detectors can be also classified by their physical characteristics as gaseous, semiconductors, scintillators and passive detectors. We will see an example of each one in the application to fast neutron detection, that is the range of energies of RIPTIDE.

An example of *gaseous detectors* is the fission chamber: a gas detector filled with a $^{238}$U sample. In these types of detectors, neutron-induced fission produces charged fission fragments. Then, the detector works as a ionization chamber and identify the presence of the neutron by the detection of those charged particles.

*Semiconductor detectors* are exploited in combination with suitable converters ($^{10}$Ba and $^{6}$Li). Another fascinating material is the diamond detector whose main advantage is that of being made of carbon and thus of well simulating tissue-like response. However, these detectors have a bad response at energies lower than 5-6 MeV.

*Scintillator detectors* exploit the ability of certain materials of emitting visible photons (scintillation light) when excited by ionizing radiation. The detection of neutrons with these materials is made possible thanks to the presence of nuclei that have an high neutron cross section. In plastic scintillators, this mechanism is enhanced by the high proton density in hydrocarbons (see later in Section 2.1.3). Another atom that is commonly used in scintillation is $^{4}$He. Typically the poor light yield of this gas is enhanced up to 5 times by the addition of Xenon.

Finally, an example of *passive detectors* is that of photographic emulsion. In these systems, the presence of a neutron is given by the track of recoil proton or other reaction products inside the emulsion. The main disadvantages of this system is the complex scanning process.

A particular type of fast neutron detectors is worth mentioning is the spherical dosimeter, also called *Bonner sphere*, devised by Bramblett, Ewing and Bonner in 1960 [29]. It consists of lithium iodide scintillators, a commonly used slow neutron detector, placed at the centre of polyethylene moderating spheres of different diameters. A setup made of these spheres of different sizes allows one to build a simple (thus cheap) neutron spectrometer: the lithium scintillator inside the detector is only able to detect slow neutrons. Therefore, for a fixed layer of moderator, if a neutron is too energetic, it will not be decelerated enough to be detected. Vice versa, a neutron that is too slow would be completely stopped by the plastic material and will not be detected as well. These kinds of detectors have been used, for example, to measure neutron stray radiation at the Proton Therapy Center in Trento [19].

### 2.1.3 Scintillators for neutron detection

A more in-depth discussion must be reserved to scintillator detectors, due to the fact that RIPTIDE itself is based on that. As already mentioned, with the increasing of the energy, elastic scattering acquires more importance, and neutron detection based on scintillator exploits this mechanism.

A scintillator is a material that emits photons when it is crossed by ionizing radiation. Ideally, a scintillator detector should have the following characteristics: it should convert charged particle kinetic energy into visible light with an high scintillation efficiency and with a light production that is linearly proportional to the the particle energy; the medium should be transparent to the wavelength of the scintillation light and its index of refraction should be similar to that of glass ($\sim 1.5$), in order to allow efficient coupling with photomultipliers and optics; the decay time of photon production should be sufficiently short to allow fast signals to be detected.

Of course, no real scintillator has all the required characteristics mentioned above and the choice of one material rather than another is due to the needs of the experiment. Scintillators are commonly classified, based on the material they are made of, into organic and inorganic.

If a good light yield is required, inorganic based scintillators should be chosen (sodium iodide crystals (NaI) has the highest light yield). In the case of neutron detection, organic scintillators must be used due to their high hydrogen content, that is necessary for n-p elastic scattering. Moreover, organic scintillators light emission is faster compared with inorganic ones (with a decay time of the order of nanoseconds) and so they could be used for real time radiation detection.

**Organic scintillation mechanism.** We now briefly describe organic scintillator light emission mechanism.

In organic scintillators, radiative de-excitation processes arise from the transition in the energy level structure of the single molecule. This transition happen independently from the physical state (solid, liquid or gas). The majority of organic scintillators are based on a particular energy level configuration called $\pi$-electronic structure. This configuration energy level is sketched in figure 2.1. This configuration allows a series of singlet states (spin = 0), labelled in figure as $S_0$, $S_1$ and triplet states (spin = 1), $T_1$. The spacing between $S_0$ and $S_1$ is typically 3-4 eV. Each of these states is further subdivided into other closer energy levels (vibrational states), with a spacing of about 0.15 eV. We label each level with another index, therefore we will call ground state $S_{00}$, the subsequent level as $S_{01}$ and so on. At room temperature, this gap is large compared with the thermal energy (0.025 eV), therefore nearly all the molecules at room temperature are in the state $S_{00}$.

When a charged particle passes trough the material, it releases part of its kinetic energy to the surrounding electrons (see appendix A). As a consequence, these electrons

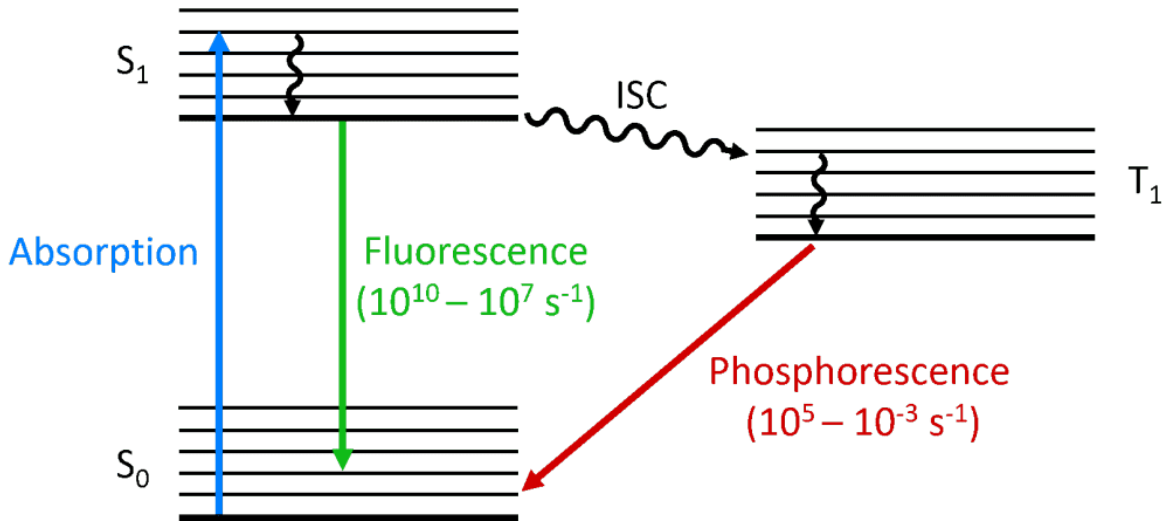


Figure 2.1: Sketch of scintillation mechanism for an organic scintillator.

will be upgraded to an excited state (the blue arrow in figure). The molecules thus excited are not in thermal equilibrium with the molecules in the ground state, therefore they lose quickly their vibrational energy via non-radiative de-excitation to the $S_{10}$ state. Therefore, after negligible short time, a population of molecules in the $S_{10}$ state is produced.

The de-excitation from these levels to one of the vibrational states of the ground electronic level can happen in two ways. First, via the direct radiative de-excitation, with the emission of a photon (*fluorescence*); second, with the passage to the triplet state ($T_1$), trough a transition called *intersystem crossing* (ISC) and the subsequent de-excitation to the ground state from this level (*phosphorescence*). The lifetime of $T_1$ is characteristically longer than that of the single state, therefore phosphorescence photons are delayed as compared to fluorescence one. Moreover, due to the fact that the energy level of $T_1$ state is lower than $S_1$, phosphorescence wavelengths are lower than fluorescence.

Organic scintillators are generally transparent to their own fluorescence emission. Also this characteristics can be deduced from energy level distribution. Molecule excitation is from $S_{00}$ state to generally one of the excited energy of the $S_1$ ($S_{11}$,$S_{12}$, etc), while fluorescence de-excitation will mostly happen from $S_{10}$ state to one of the vibrational states of $S_0$. Therefore (and it is clearly visible from the sketch above), photons emitted in the de-excitation will have lower energies than the minimum required for excitation. Emitted photons, thus, can travel all the material undisturbed.

There are many types of organic scintillators with the most disparate characteristics. Since the scintillation principle depends on the molecule, they work in the same way regardless the physical state: solid, liquid or gas-based scintillators has been devel-

oped [29].

**Neutron detection in organic scintillators.** As mentioned before, the use of scintillators for neutron detection requires the presence of hydrogen inside the scintillator material. All organic scintillators can be used, and Anthracene has the highest light yield. However, plastic scintillators are often used due to their relatively low cost and for the wide variety of sizes and shapes they can be tailored into.

The scintillator size should be defined in a way that (1) n-p elastic scattering probability inside the scintillator is sufficiently high (that means that the neutron free mean path inside the scintillator should be comparable to the scintillator thickness) and (2) that enough scintillator light can exit the scintillator without being absorbed by the material [29].

**Ideal and real recoil proton spectrum.** In equation 2.1, given a fixed neutron energy ($E_0$), proton energy is uniformly distributed between 0 and $E_0$. Therefore, for a monochromatic neutron source, the energy distribution of deposited neutron energy will be a step function as in 2.2 (a).

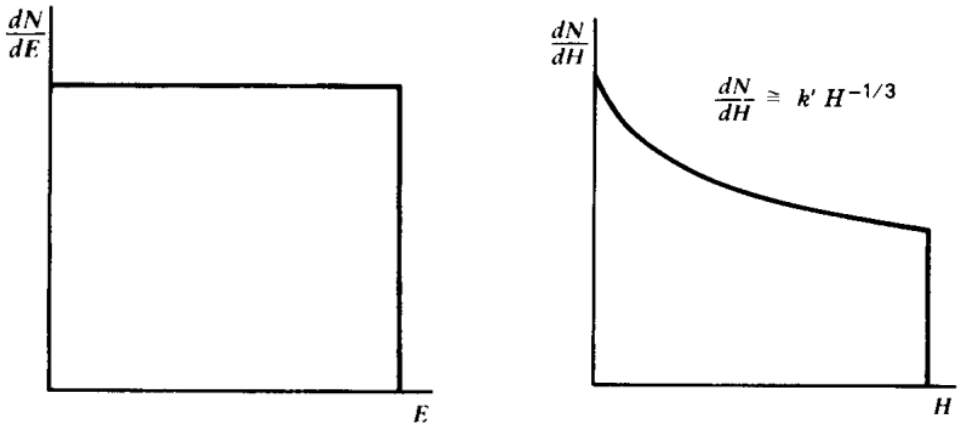


(a) (b)

Figure 2.2: Deposited energy by a monochromatic neutron source (a) compared with scintillation photon output (b). In n-p scattering, neutrons lose an amount of energy that is uniformely distributed between 0 and $E_0$ (it could lose all its kinetic energy in one scattering). The fact that photon yield is not linear with proton energy produces a light output as shown on the right figure.

However, there are several factors that do not allow one to obtain the recoil proton energy spectrum as in figure (a). One of them is that in many organic scintillators, the

light output (H) is not linear with respect to the proton energy, but it rather follows the relation

$$H = kE_p^{3/2} \tag{2.2}$$

with k constant. The pulse height distribution shape is therefore given by

$$\frac{dN}{dH} = \frac{dN/dE}{dH/dE} = \frac{constant}{\frac{3}{2}kE^{1/2}} = k'H^{-1/3} \tag{2.3}$$

The effect of the non linearity is to distort the ideal spectrum as in figure 2.2 (b).

**Proton scattering competing reactions.** Plastic scintillators are based on hydrocarbons, i.e. they are composed essentially of hydrogen and carbon atoms, generally in comparable quantities. The scintillator used in RIPTIDE is, for example, polyvinyl toluene, whose linear formula is $[CH_2CH(C_6H_4CH_3)]_n$ (or roughly 9 carbon ions every 10 hydrogens). It is thus essential, when considering the probability of n-p scattering, to also consider interaction probability with carbon[1].

Figure 2.3 shows a comparison of the cross sections of all the predominant interaction mechanisms of neutron with carbon. In the figure, it is also shown as a comparison n-p elastic cross sections, H(n,n)H. It is clearly visible that the dominant interaction is carbon elastic scattering that has a cross section that is comparable with that of hydrogen.

In this range, carbon scattering compete strongly with proton one. At higher energies, after certain thresholds, other neutron-carbon reactions could also take place. After 8 MeV, carbon total cross section (the solid line) overcome hydrogen scattering.

The effect of carbon interactions complicates neutron detection. Carbon inelastic reactions generate other particles which are not always possible to detect. With regard to elastic scattering, on the other hand, we saw in equation 2.1 the maximum energy given to carbon is lower than that given to hydrogen. Therefore, scattering from carbon ions does affect the detector response function because their kinetic energy is too low to be detected but they contribute to neutron moderation. We will see, moreover, that in the case of recoil proton tracking imaging, carbon scattering could invalidate the measure of neutron direction (see Section 2.2.1)

In plastic scintillators, photons are generated along the path of the charged particle. Therefore, if it is possible to use an optical device capable of obtaining an image of the scintillator in the instant following the passage of a particle, then it is also possible to reconstruct the particle track. If in a scintillator it is possible to detect a recoil proton track, then it is theoretically possible to fully determine neutron initial momentum. We explain the theoretical basis of this technique in the next section.

[1]Although other isotopes can also be present, here we consider essentially $^{12}C$ and $^{1}H$ because of their great natural abundance (for both is about 99% of all their isotopes.)

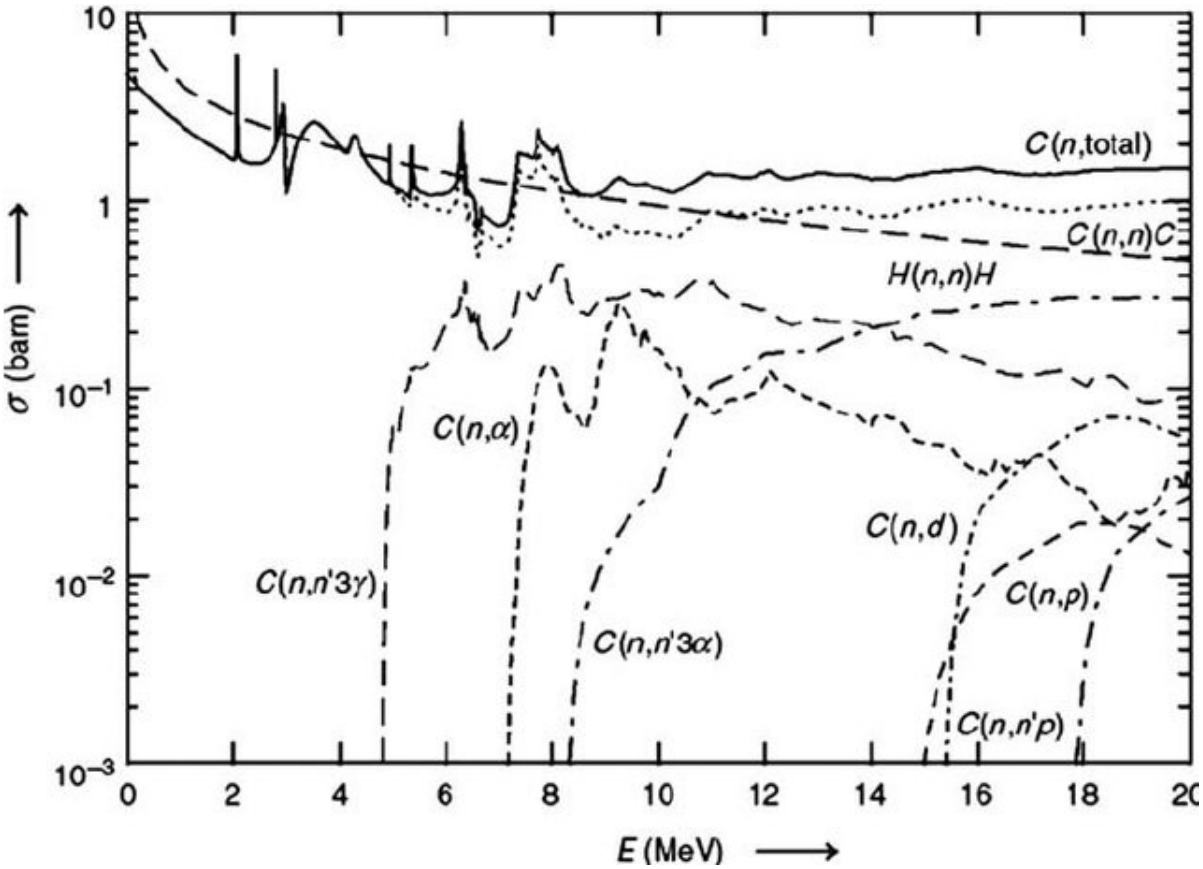


Figure 2.3: Elastic and inelastic neutron cross section with carbon. Neutron-to-proton elastic scattering is also reported as a reference [4]. It can be noticed that carbon total cross section is a concurrent reaction with respect to the hydrogen one.

## 2.2 Recoil Proton Track Imaging techniques

In recent years, increasing attention has been paid to a new technique of neutron detection. It takes the name of Recoil Proton Track Imaging (RPTI) and its purpose is to get information on neutron energy and direction from the proton track left on a scintillation medium.

This innovative detection technique needs two necessary elements: a neutron-to-proton recoil converter and a proton track imaging system. The first item is needed for neutron-to-proton elastic scattering, via the use of materials rich in protons (e.g. plastic); the other one is generally made of a scintillating material and a real time imaging device. The scattering needs to be elastic because RPTI technique requires the assumptions of momentum and energy conservation.

Several projects that make use of this technique have been proposed. They can exploit

single scattering to obtain only neutron energy (in this case neutron source position needs to be known), or multiple (double or triple) scattering to fully determine neutron momentum. In the following, we show the mathematical foundation behind these two techniques and the projects that have been developed to exploit them.

### 2.2.1 Multiple scattering

In principle, it is possible to fully determine neutron direction and energy if it is possible to detect all recoil nuclei of a triple scattering of neutrons with matter. To explain the idea behind, we will follow the analysis proposed in [68]. Wang and Morris showed that the information provided by a triple scattering recoil nuclei (it works for all nuclei species (p, C, Si, etc.)) is sufficient to fully determine incoming neutrons momentum.

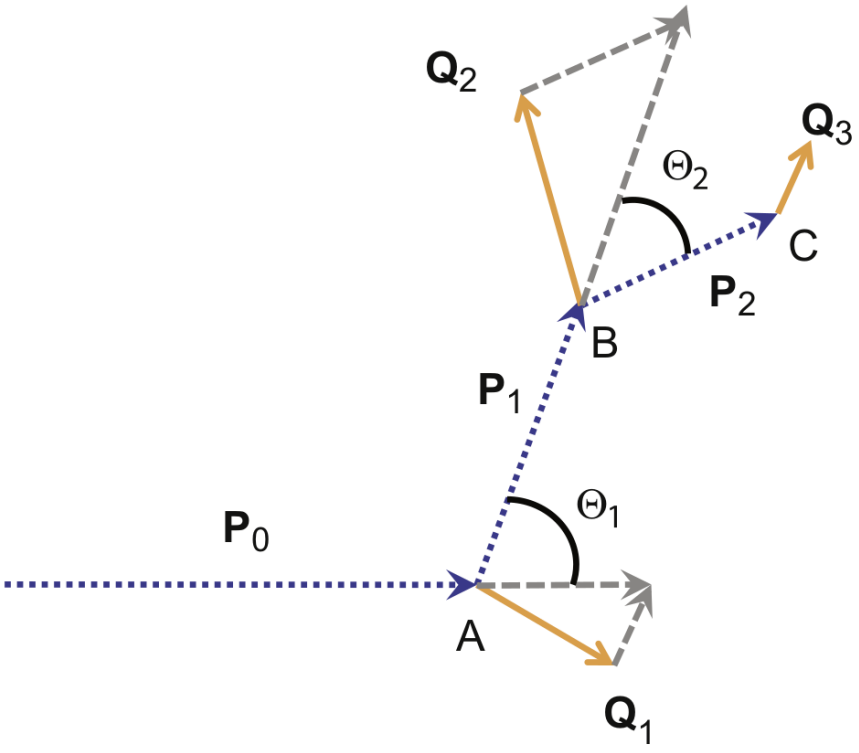


Figure 2.4: Sketch of multiple scattering. $P_0$, $P_1$, $P_2$ are neutron momenta during each step, $Q_1$, $Q_2$ and $Q_3$ are recoil proton momenta, $\Theta_1$ and $\Theta_2$ are neutron scattering angles [68].

With the notation as in figure 2.4, the momentum conservation imply:

$$\vec{P_0} = \vec{Q_1} + \vec{P_1} \tag{2.4}$$
$$\vec{P_1} = \vec{Q_2} + \vec{P_2} \tag{2.5}$$

Obviously, $\vec{P_0}$, $\vec{P_1}$ and $\vec{P_2}$ can be broken down into their scalar and versor component:

$$\vec{P_0} = p_0\hat{e_0} \quad \vec{P_1} = p_1\hat{e_1} \quad \vec{P_2} = p_2\hat{e_2} \tag{2.6}$$

The scalar product of $\hat{e_1}$ and $\hat{e_2}$ with 2.5 gives respectively:

$$p_1 = \vec{Q_2} \cdot \hat{e_1} + p_2\hat{e_2} \cdot \hat{e_1} \tag{2.7}$$
$$p_1\hat{e_1} \cdot \hat{e_2} = \vec{Q_2} \cdot \hat{e_2} + p_2 \tag{2.8}$$

From which, after a simple calculation, it is possible to obtain:

$$p_1 = \frac{\vec{Q_2} \cdot \hat{e_1} - (\vec{Q_2} \cdot \hat{e_2})(\hat{e_1} \cdot \hat{e_2})}{1 - (\hat{e_1} \cdot \hat{e_2})^2} \tag{2.9}$$

By substituting 2.9 in 2.5:

$$\vec{P_0} = \frac{\vec{Q_2} \cdot \hat{e_1} - (\vec{Q_2} \cdot \hat{e_2})(\hat{e_1} \cdot \hat{e_2})}{1 - (\hat{e_1} \cdot \hat{e_2})^2} \cdot \hat{e_1} + \vec{Q_1}. \tag{2.10}$$

From the relation above (2.10) it is clear that $P_0$ is fully determined if it is possible to measure the momentum of the first two recoil protons ($Q_1$ and $Q_2$) and the direction of the scattered neutron after the first and the second scattering ($\hat{e_1}$ and $\hat{e_2}$). $Q_3$ is necessary only to determine $\hat{e_2}$, obtained from the joining of the second and third scattering points ($B$ and $C$).

This technique, although theoretically simple, is experimentally complicated: the probability to see a triple scattering is quite a rare event for fast neutrons inside the typical dimensions of the scintillators involved in neutron detectors. Other techniques that imply the use of a lower number of scattering centers (1 or 2) should be considered.

### 2.2.2 Single proton recoil detection

If the neutron source position is known, this technique is able to determine, by observing a single recoil proton (single scattering), the neutron energy. It can be done by exploiting the relation:

$$E_n = E_p/cos^2(\theta) \tag{2.11}$$

with $E_n$ and $E_p$ respectively neutron energy before the scattering and proton energy after it, $\theta$ being the proton scattering angle (see figure 4.12). It is important to notice that this equation is valid only for proton scattering and it is not valid for elastic scattering with other nuclei (as, for example, carbon).

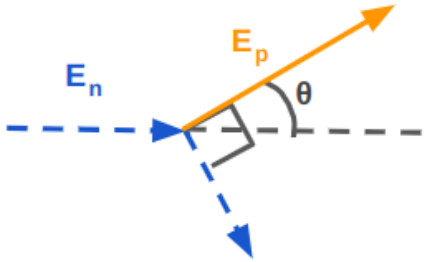


Figure 2.5: Sketch of single scattering. $E_n$ and $E_p$ are respectively neutron and proton energy, $\theta$ is the angle between neutron initial direction and recoil proton direction. If neutron position is known, with the information of a single scattering (proton energy and direction) it is possible to obtain neutron energy.

Neutron initial direction in this case is known and, by determining recoil proton track as in figure 2.5, it is possible to deduce also $\theta$.

Several detectors based on single scattering are under study. For example, an article dated 2018 shows a concept for a possible detector to be exploited in proton therapy [11]. Here, proton direction is found via 3 CMOS sensors and it is able to work in the 5-20 MeV range.

Another prototype recently proposed is FaNS-2 [32], that is developed to measure flux and spectrum of fast neutron energy from a few MeV to several GeV. It has been specifically designed for the study of low neutron fluxes such as cosmogenic neutrons at the Earth surface.

Finally, it is worth mentioning the work carried on by Hu and Liu [28]. They built a relatively simple neutron detector based on a fixed angle proton detection mechanism. In this article, a polyethylene foil has been used as scattering system and the proton detector, made of $CF_4$ gas scintillator, was placed at a fixed angle with respect to the neutron initial direction. This implied the disadvantage of a high efficiency loss (only protons emitted at a certain angle are detected. Proton tracks that came out in the scintillator was then acquired by a CCD camera. Because the detection occurred at a fixed angle, the only variable of the experiment was proton energy ($E_p$). Figure 2.6 shows recoil protons produced by neutrons at two different energies. $E_p$ was obtained

by measuring the length of proton tracks inside the scintillator. Heavy charged particle range ($R$) in matter, in fact, is related with its energy ($E$) via the formula:

$$R(E) = \alpha E^p \tag{2.12}$$

where $\alpha$ depends on the material, p on proton energy.[2] From the proton track length it is possible to obtain, therefore, proton energy. In the image below, protons have respectively 5.91 MeV and 6.30 MeV.

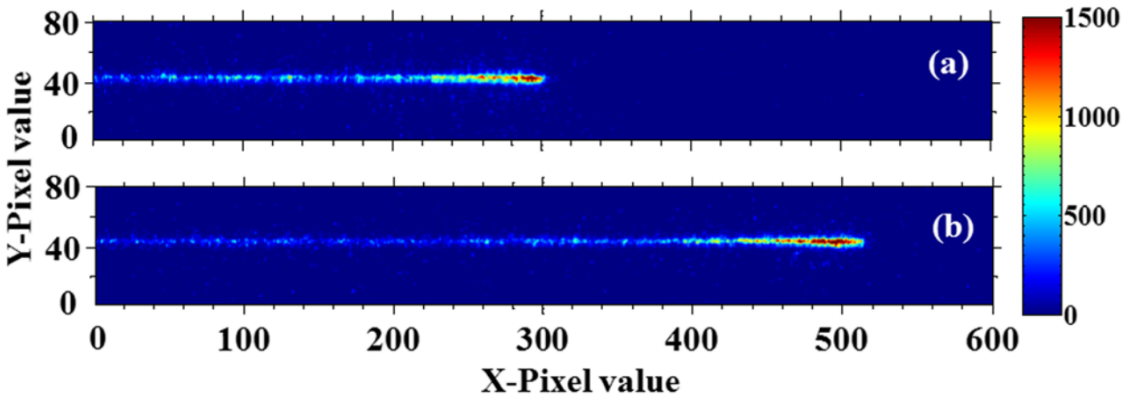


Figure 2.6: Proton tracks detected from a $CF_4$ gas scintillator. Protons have 5.91 (top) and 6.30 (bottom) MeV [28].

### 2.2.3 Double scattering

If it is possible to assume that neutrons interact twice with protons, it is then sufficient a double scattering (see figure 2.7) to fully determine neutrons energy and direction, with a resulting improvement in the detection efficiency. This assumption allows to use equation 2.11 to obtain ${p_1}^3$, while, the versor $\hat{e_1}$ is simply obtained as the connection between the two points of interaction $A$ and $B$. $Q_1$ is obtained from proton track detection. So, $P_1$ and $Q_1$ are fully determined. From conservation equation it is thus possible to obtain $P_0 = P_1 + Q_1$.

It is possible to make use of this method only by assuming that the interaction in $A$ and $B$ is a n-p elastic scattering. With regard to scattering in $A$, it is possible to verify that the recoil nucleus is a proton and that the interaction is an elastic scattering thanks

[2]For more information on Bragg peak see appendix A.

[3]Relation between proton energy and momentum is given from simple classical mechanics considerations.

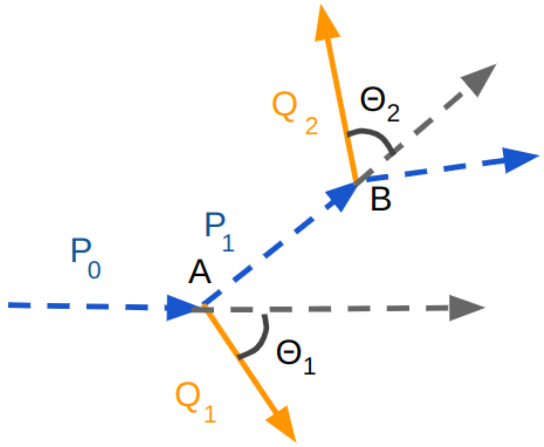


Figure 2.7: Sketch of double scattering $P_0$, $P_1$, $Q_1$ and $Q_2$ are neutron and proton momentum and $\Theta_1$ and $\Theta_2$ are the angle between incoming neutron and recoil proton.

to the 90° criterion (see appendix B): if $\vec{P_1}$ and $\vec{Q_1}$ are perpendicular, then $\vec{Q_1}$ must have the same mass of the neutron, therefore it must be a proton[4].

To date, there are two detectors that are trying to exploit neutron double scattering for the determination of neutron track. They are SONTRAC and MONDO.

**SONTRAC.** SOlar Neutron TRACking has been designed to operate between 20 and 150 MeV region, that is the energy range of neutrons produced in solar flares [39]. It is based on non-relativistic double elastic scattering of neutrons with the protons of the plastic scintillator.

Its hearth is based on a bundle composed of mutually perpendicular, alternating layers of parallel scintillating plastic fibers with a pitch of 300 $\mu$m, so that, when a sufficiently energetic neutron interacts with a proton inside the detector, the recoil proton is emitted with enough energy so to travel several fibers (at least three) before being stopped. The apparatus is $5 \times 5 \times 5$ cm$^3$ thick and for each side it is possible to obtain a grid of $150 \times 150$ pixels. In each fiber, the passage of the proton leads to the production of photons in a quantity proportional to the energy deposited. The fiber bundle is seen by two orthogonal photomultiplier tubes and by two orthogonal optics chains that include image tapers, image intensifiers and CCD cameras. These two cameras allow one to provide a stereoscopic view of proton tracks. As already mentioned in Section 2.2.1, from the detection of two proton tracks (double scattering), it is possible to reconstruct

[4]This criterion is also valid in the case of single scattering and allows one to define a cone of region of neutron emission after the interaction (the neutron will be emitted always at an angle of 90°) with respect to the recoil proton.

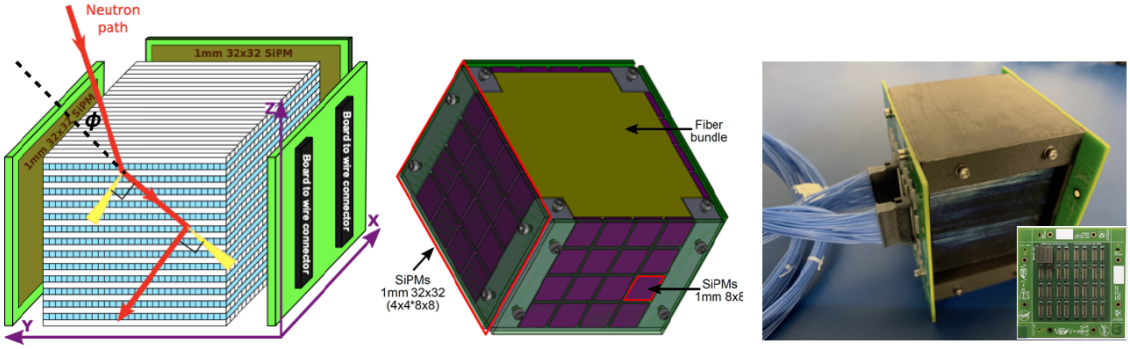


Figure 2.8: Left and center, SONTRAC sketch. In figure in left neutron double scattering has been shown. Right, SONTRAC prototype [14].

initial neutron energy and direction. In SONTRAC, energy and angular resolution of recoil protons have been determined to be $\delta E/E = 4.8\%$ and $\delta\theta = 4.6°$ at 35 MeV and they improve with energy [7].

It is worth to mention that SONTRAC obtained a 2D image of a n-p double scattering presented in an article in 1999 [55], proving the practical possibility to detect this phenomenon.

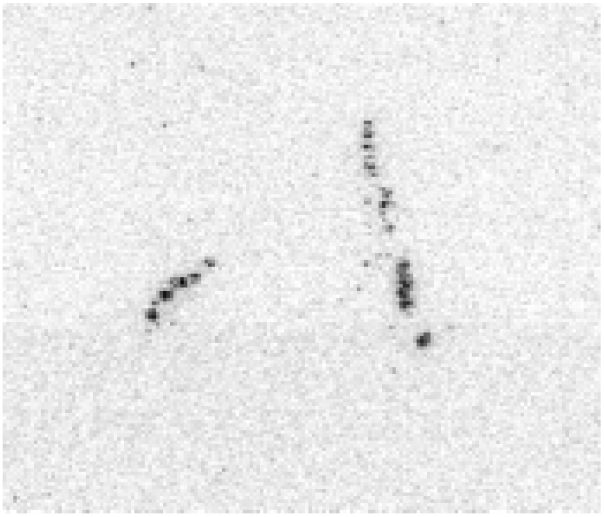

Figure 2.9: Raw CCD image of a double scatter of a 65 MeV neutron incident from the top obtained by the SONTRAC group [55].

**MONDO.** MOnitor for Neutron Dose in hadrOntherapy [62] has been designed with a similar configuration to that of SONTRAC.

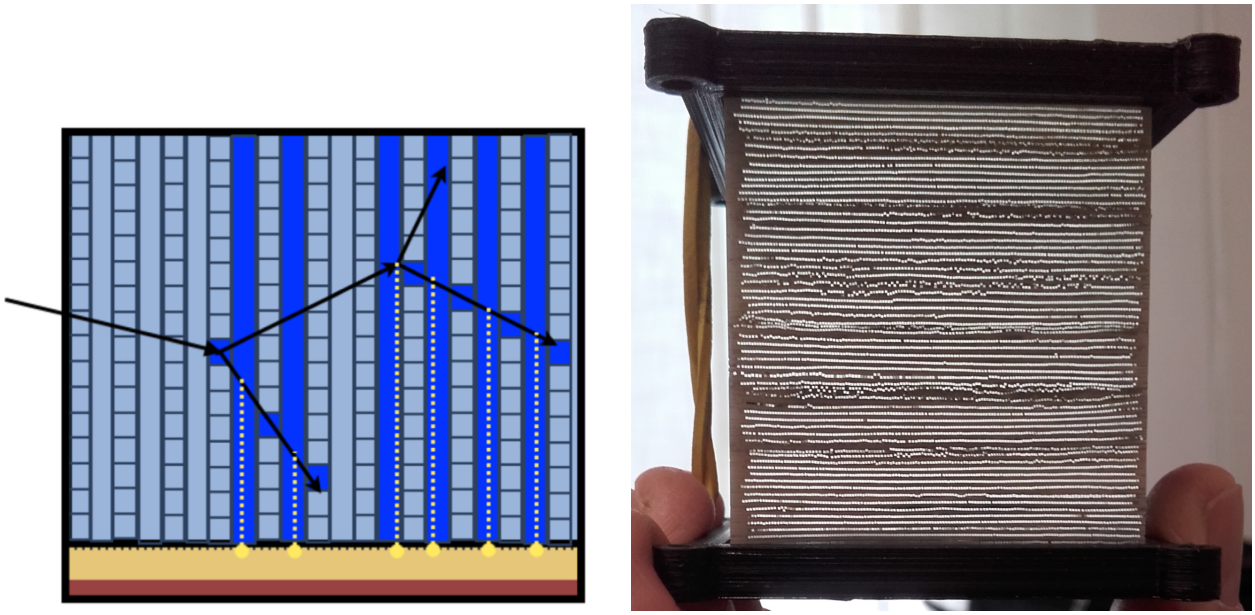

(a) (b)

Figure 2.10: (a) sketch and (b) picture of MONDO prototype

Again, a matrix of scintillating fibers constitutes the place of neutorn scattering and detection. The photons emitted by the scintillator are captured by an optical system. Differently than SONTRAC design, this detector has been designed to detect neutrons produced during particle therapy treatments, whose energies range from 20 to 600 MeV. Optical sensors used in MONDO consist of a signal amplifier, Gas Electron Multiplier (GEM) chamber was used for this purpose, and an acquisition system, a CMOS Single Photon Avalanche Diod (SPAD).

In 2018, a first simple prototype of the MONDO project, Penelope, has been developed [22] and its output result were compared with a Monte Carlo simulation. Penelope was made of a $4 \times 4 \times 4.8$ cm$^3$ cube of scintillating fibers and was tested for the detection of neutrons for both single and double scattering. A novel SPAD has been developed specifically for this detector, called SPAD Based Acquisition for the MONDO experiment (SBAM), with time and spatial resolution tuned specifically for the experiment (respectively $\sim$ 100 ps and $\sim 125 \times 250$ $\mu$m$^2$). Neutron energy resolution between 4% and 11% has been found for single scattering, while a resolution lower than $\sim$ 8% has been found (but still under investigation) for double scattering events.

# Chapter 3

# RecoIl Proton Track Imaging DEtector: RIPTIDE

This chapter provides a throughout discussion of the principle of operation and design of the RIPTIDE detector. The physical mechanisms that take place in the detection of a neutron with RIPTIDE are recapitulated in Section 3.2, and a description of its components is presented in Section 3.3.

## 3.1 RIPTIDE concept

In the previous chapter an overview of the state of the art of fast neutron detectors was presented. In addition, organic scintillators detection mechanism was discussed together with their use as neutron detectors. Details of recoil proton track imaging technique both in the case of single and sequential n-p scattering were discussed showing applications to neutron detection. We finally described the two most relevant detectors that have been proposed for double n-p scattering recoil proton detection: SONTRAC and MONDO. Here, the concept of the detector we aim to develop is discussed in detail.

RIPTIDE, RecoIl Proton Track Imaging DEtector, aims at detecting neutrons in both single scattering mode (when neutron source is known) and double scattering mode (with the determination of neutron track and energy). In Section 2.2 the simple mathematical foundations behind these detection mechanisms was illustrated. In the case of single scattering, if neutron source position is known, it is possible to obtain neutron energy from the relation $E_n = E_p/cos^2(\theta)$. Double scattering allows one to obtain also neutron initial direction, even if the source position is not defined a priori.

Differently than MONDO and SONTRAC, which are both based on a matrix of scintillating fibers, RIPTIDE consists of a cube of plastic scintillator. This implies a significant difference in recoil proton track detection and reconstruction. In other detectors, in fact, the proton track reconstruction is obtained from the detection of the

light produced by the scintillating fibers singularly. The dimension of the single fiber determines a physical constraint for the spatial resolution (e.g. for SONTRAC is 300 $\mu$m) and its photon intensity is linked with the amount of energy deposited in a fiber by the proton. Moreover, in order to reconstruct proton track, the particle should be enough energetic to travel through at least three different fibers. It should therefore have enough energy to pass 600 $\mu$m of scintillating material. We can roughly estimate that a proton range of 600 $\mu$m corresponds to a proton's energy of at least 6 MeV.

The light output is therefore pixelated, as it can be seen from figure 3.1, representing the data acquired by a prototype of SONTRAC. In the figure, the position of the Bragg peak can be clearly inferred.

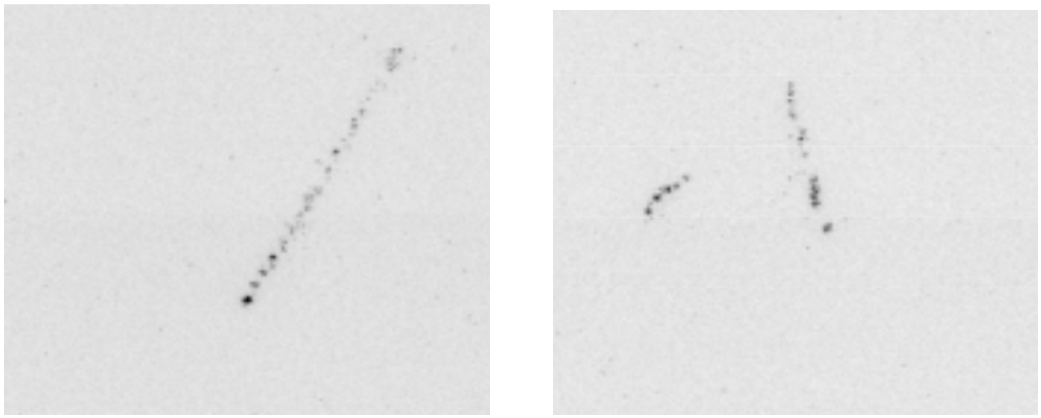

Figure 3.1: Single n-p (left) and double n-p scattering (right) obtained with a SONTRAC protoype. Proton tracks are pixelated because SONTRAC is made of scintillating fibers. It is also possible to observe that one end of each segment is brighter than the other. This is the effect of proton energy loss behaviour (Bragg peak) in the scintillation light output [55].

The use of a solid cube could overcomes these spatial resolution limits. In the case of RIPTIDE, in fact, photons are produced along the whole track. For instance, a proton inside a scintillator produces typically $10^3$ photons per MeV, and so a 3.5 MeV recoil proton produce approximately $10^4$ MeV distributed along a 0.2 mm track. [44] This represents the spatial resolution of RIPTIDE: 0.2 mm (200 $\mu$m). Moreover, track imaging inside the scintillator allows one to distinguish photons from neutrons. While neutrons are identified by the presence of recoil protons, photons induce the emission of scintillation light along the whole track.

However, the improvement in spatial resolution is counterbalanced by greater difficulty in the optical acquisition of photons. To tackle this problem, the use of two high-sensitivity optical systems is currently being evaluated. Once the optical system is defined, the idea is to use three of these optical systems, coupled to the scintillator, in

order to obtain a stereoscopic imaging. We aim to obtain a 3D reconstruction of proton tracks inside the scintillators.

In addition, a Silicon photomultiplier is included in the experimental setup to work as a trigger and to synchronize the three optical systems for the frame acquisition (it is necessary, for the three-dimensional reconstruction, that all the optical systems acquire the image at the same time). A sketch of the RIPTIDE concept is shown in figure 3.2. In the present chapter we will enter in detail of the characteristics of all the different elements of RIPTIDE.

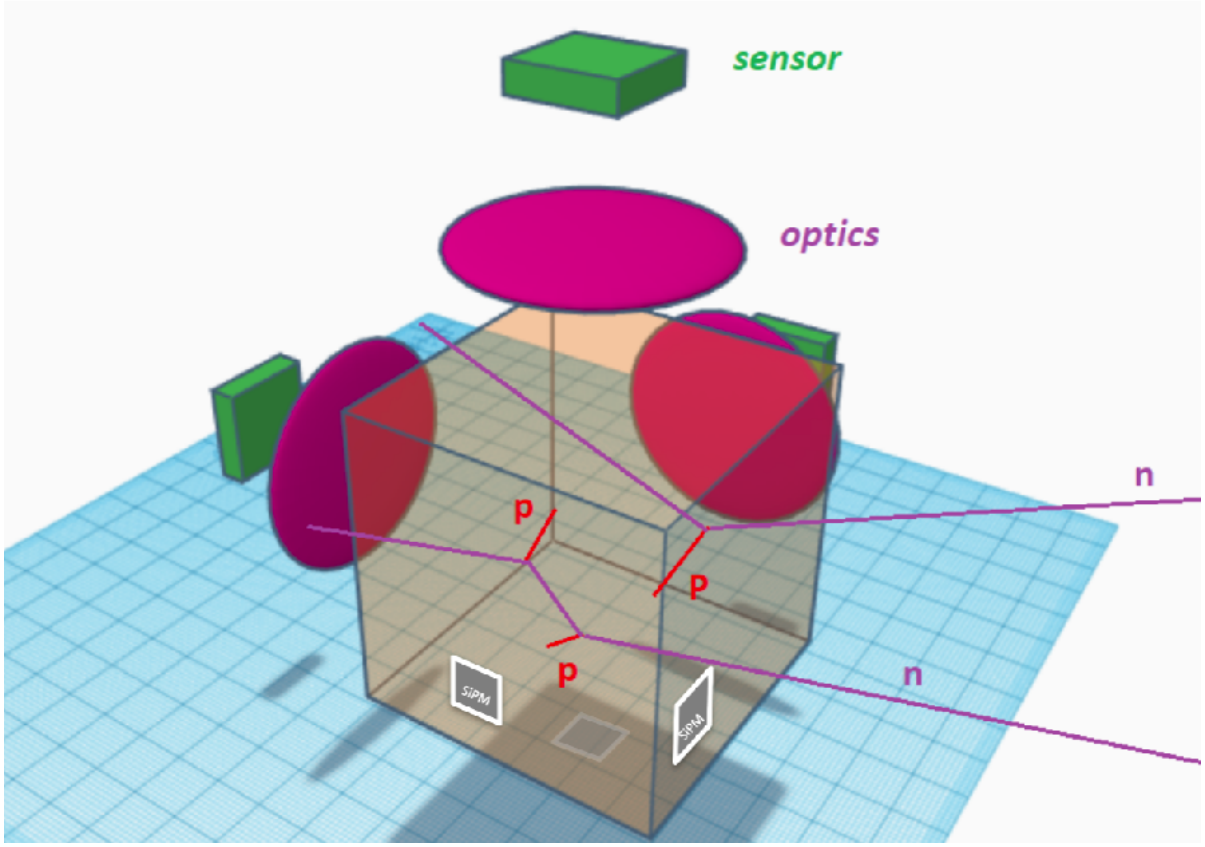


Figure 3.2: RIPTIDE working principle. A plastic scintillator is coupled to an optical system to acquire photons produced by recoil protons. A silicon photomultiplier will work as a trigger and synchronizer for the image acquisition from optical systems. [8]

Before that, it is worth mentioning an experiment that successfully obtained a 3D reconstruction of electrons inside a scintillator [20]. With the use of mirrors and lenses, they coupled a $4 \times 4 \times 4$ mm plastic scintillator with a photon detector build specifically for the experiment, Hybrid Photon Detector (HPD). HPD has both high spatial and temporal resolution (respectively 6 $\mu$m and 10 ns) and single optical photon detection

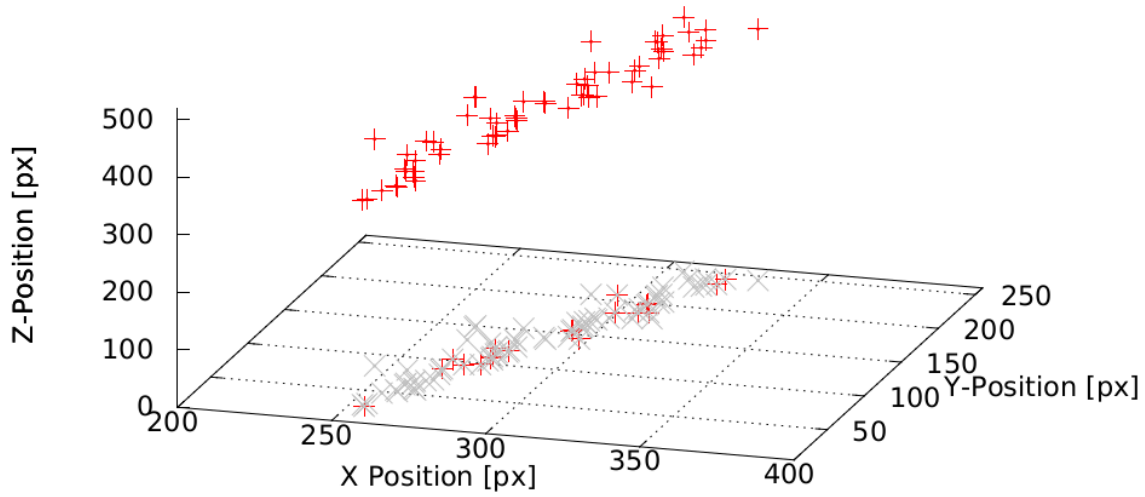


Figure 3.3: 3D reconstruction of 5 GeV electron track inside a plastic scintillator [20].

peaked in the blue/violet spectral range ($\sim$ 390 nm). Filipenko et al. were able to reconstruct in three dimension the tracks of 5 GeV electrons. They used two orthogonal imaging devices to obtain the track showed in figure 3.3.

RIPTIDE was conceived to be useful for a variety of applications as mentioned in chapter 1. Table 3.1 summarizes the requirements that need to be achieved in different fields. A compromise in performances can be accepted in some cases, though.

| | Energy region of interest (MeV) | Expected efficiency (%) | S-o-A (%) | Time resolution | Energy resolution (%) | Angular resolution (degrees) |
|---|---|---|---|---|---|---|
| Nuclear Physics (n_TOF) | 10-100 | 10-60 | - | 1-10 ns | 2-20 ns | 0.5 |
| Astrophysics (space env.) | 10-1000 | 10-50 | 10-30 | 1-100 ms | 10-50 | 1 |
| Particle Therapy (FOOT) | 20-400 | 1-30 | 1-2 | 1-10 ns | 5-20 | 0.5 |
| Environmental n-tracking | <20 | 10-90 | - | counter | - | 1-5 |

Table 3.1: Requirements and expected region of interest in the different application fields. S-o-A is the state of the art of the different efficiencies.

## 3.2 RIPTIDE working principle

As already anticipated, a neutron must interact with the scintillator to be detected. Interacting via the strong nuclear force, the probability of interaction is small: the majority of neutrons cross the entire thickness of the scintillator undisturbed and are not detected. (In Section 4, with a Monte Carlo simulation, these probabilities has been provided).

The active volume in RIPTIDE is a $6 \times 6 \times 6$ cm$^3$ plastic scintillator, almost uniquely made of carbon-12 ions and protons[1]. Neutrons interact in the scintillator both with a proton and with a carbon ion according with their cross sections (see figure 2.3).

At the energies of interest for RIPTIDE, i.e. 3-50 MeV in the first feasibility study, neutrons and protons can scatter elastically, while a neutron can interact with carbon either via elastic scattering, or nuclear reactions, whose probability increases with the increasing of neutron energy. Above 10 MeV, carbon elastic scattering cross section becomes larger than proton scattering.

In the collision, neutrons transfer part of their energy to the nucleus that is involved in the interaction. The amount of energy transferred to the nucleus depends on the atomic number ($A$) of the nucleus itself: it is uniformly distributed between $(\frac{A-1}{A+1})^2 E_0$ and $E_0$, where $E_0$ is neutron energy before the interaction (see Eq. 2.11). In n-p elastic scattering, the neutron can lose up to all its energy, which is transferred to the proton; in the case of n-$^{12}C$ elastic scattering, carbon ions could only acquire up to 28% of neutron energy. Therefore, for the same neutron energies, recoil protons have generally higher energies compared with recoil carbons. In addition, the range of a certain particle in a certain material is linked to the proton range in the same material via the equation $R_{nucleus} = M/Z^2 R_{proton}$ (see equation A.4 in the appendix), where M is the mass of the particle (compared to proton mass) and Z is the unit charge (of course for protons M = 1, Z = 1). In the case of $^{12}C$, M = 12 and Z = 6, a carbon ion range is only about a third of the range of a proton with the same energy. The combination of these effects implies that the kinetic energy of the recoil carbon and its range are generally too low to be detected.

The fact that the experimental signature of n-C elastic scattering is below the detection threshold has an effect on the detection efficiency. For example, a neutron could interact with a carbon ion before interacting with a proton. In the first interaction it changes the kinetic energy and direction of the neutron. As anticipated, this first interaction could not be seen by the optical system, while the second does. The double scattering could be mistaken with a single scattering with the consequent miscalculation of neutron initial energy (see next chapter for a quantitative description).

The miscalculation of neutron energy due to carbon scattering is graphically explained in figure 3.4.

[1]Other elements and isotopes as $^{13}C$, deuterium or tritium are present only in small quantities.

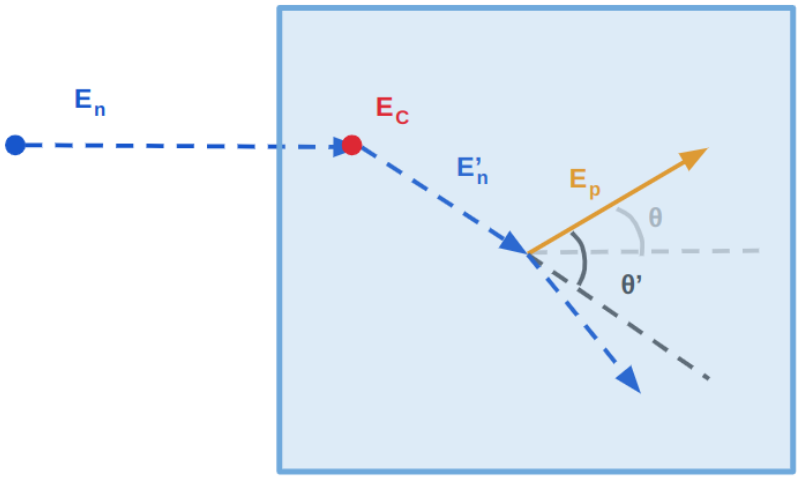


Figure 3.4: Sketch of a double scattering in which the first interaction is with a carbon ion while the second interaction is with a proton. Experimentally this event cannot be disentangled by a single scattering. $E_n$, $E_p$ and $E_C$ are neutron, proton and carbon energy. $\theta'$ is the real scattering angle between recoil proton and the neutron before the impact, $\theta$ is the scattering angle if a single scattering is considered (the source position is far if compared to the scintillator dimension).

Suppose that the source position is known and is far from the scintillator; in good approximation neutron direction is fixed (horizontal in the sketch). However, nor the neutron neither the carbon are "visible", and proton track (in orange) can be recorded (see figure 3.5).

This is, however, exactly the same signal that is visible in the case of single scattering (figure 2.5): in summary, the two events are indistinguishable. The miscalculation of neutron energy arises from the fact that the scattering angle of the recoil proton is different. In figure 3.4, $\theta'$ is the angle between scattered neutron (after carbon scattering) and recoil proton, while $\theta$ is the angle between the unscattered neutron (from the source) and the proton. As it can be seen from the figure, these two angles are different. Neutron energy miscalculation arises from the fact that the relation between neutron and proton energy depends on the scattering angle ($E_n = E_p/cos^2(\theta)$). Therefore, a miscalculation of the angle between the neutron and the proton implies a miscalculation on the neutron energy. The effect of energy loss due to n-C scattering is a side effect with respect to the error caused by the miscalculation of the angle because the maximum energy loss by the neutron is 28% of initial neutron energy.

Sometimes (for higher neutron energies), it can happen that the energy of this ion is sufficiently high that the light produced by its track is high enough to be detected

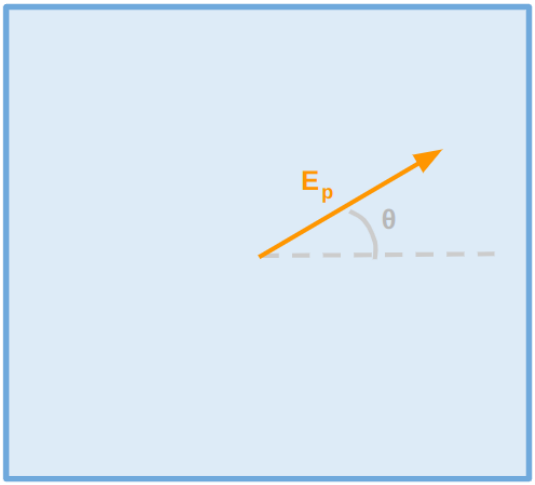


Figure 3.5: The detected signal for both a single scattering and a double scattering in which the first recoil nucleus is a carbon atom.

from the readout system. Consider a recoil proton and a recoil carbon ion with the same energy. Both carbon and proton release all the energy inside the scintillator but proton path is longer than carbon one. The scintillator output is proportional to the energy released from the particle in the medium, therefore both carbon and proton track will emit a comparable amount of photons. Because the range of a carbon ion is shorter, emitted photons from this track will be more dense. The output of a recoil carbon in the readout system, if it can be seen, will be a small bright spot that cannot be used for track reconstruction.

If the neutron interact once or twice with protons, neutron energy and direction can be determined, as discussed in Section 2.2. Stereoscopic imaging is used to obtain proton track. In figure 3.6 an illustration of a neutron having a double scattering inside the scintillator is provided. Right angles between proton and neutrons have been drawn.

All the information necessary for RPTI can be obtained from proton tracks. They consist of a segment with an end brighter than the other, that give information on where the proton is pointing at. As already mentioned, proton energy is obtained from the length of the tracks (equation A.3).

## 3.3 Detector components

Having defined the principle of operation of RIPTIDE, we can now focus on the different components.

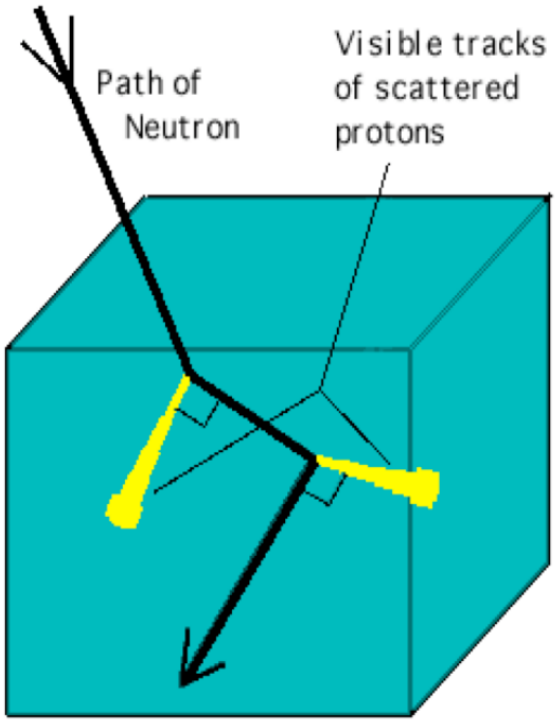


Figure 3.6: Double elastic n-p scattering inside a plastic scintillator cube. Neutrons and Protons are scattered with a 90° angle. Only the yellow tracks produce a signal [7]

### 3.3.1 Scintillator

We already introduced the physical characteristics of plastic scintillator detectors and their use as neutron detectors (Section 2.1.3). Therefore, we can now introduce the specifics of the plastic scintillator we chose for our detection needs.

Specifically, BC-408 was used, that is a plastic scintillator made of polyvinyl toluene similar to the ones in figure 3.7. This scintillator has a good time resolution with low rise and decay time (0.9 and 2.1 ns) and light output of 64% with respect to Anthracene. Moreover, it has a proton to carbon ratio favorable, approximately equal to one. Scintillator emission light is peaked at 430 nm in the violet spectral range. It is important to consider this last information when considering the coupling with the optical system. The spectrum of emission (in figure 3.8) and the spectrum of acquisition of the readout system must overlap. A deeper analysis on this issue will be proposed in Section 3.3.2.

The size of the scintillator has been chosen in order to both maximize probability of neutron scattering and minimize recoil proton escape in the neutron range under study: between 3 and 50 MeV [12]. We chose to use a cubic scintillator with a size of $6 \times 6 \times 6$ $cm^3$, approximately corresponding to twice the range of 50 MeV protons

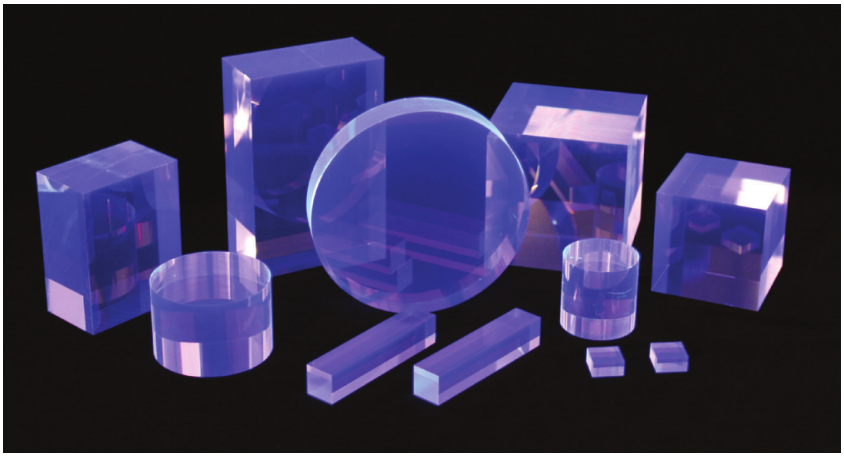

Figure 3.7: A set of plastic scintillators of different sizes and shapes is shown. Their blue-violet color is the characteristics scintillation emission light. Being composed of a plastic material, they can be produced with a large variety of different dimension and shapes [59].

in the scintillator. In figure 3.9 it is reported proton range as a function of its energy inside BC-408 plastic scintillator. In chapter 4, neutron efficiency has been evaluated quantitatively for the detector geometry we used.

**Scintillator wrapping.** In conventional scintillator detectors, it is required to decrease photon losses as much as possible. Therefore, to enhance the number of photons detected, it is a common practice to cover all the scintillator with a wrapping (typically Teflon is used) that has the purpose of increasing internal reflection of the photons inside the scintillator. Since we are interested in the optical acquisition of the track, these reflected photonsproduce a background on the image acquired by CMOS cameras, making the track reconstruction more complicated. Therefore, to reduce photon reflection (instead of increasing it), the plastic scintillator has been wrapped with a black aluminium paper commonly called Cinefoil[2] that has the ability of absorbing a great quantity of the impinging photons in the visible region.

### 3.3.2 Detector readout

At this stage, the optical system is one of the most critical topic for the construction of this type of detector: very high spatial resolution and photon detection efficiency is required. For this purpose, two complementary readout systems are being currently

[2]As the name suggests, this material has been developed for cinema application, but its photon absorption properties in the wavelength range of our interest makes it suitable in scientific experiments that require good photon absorption properties.

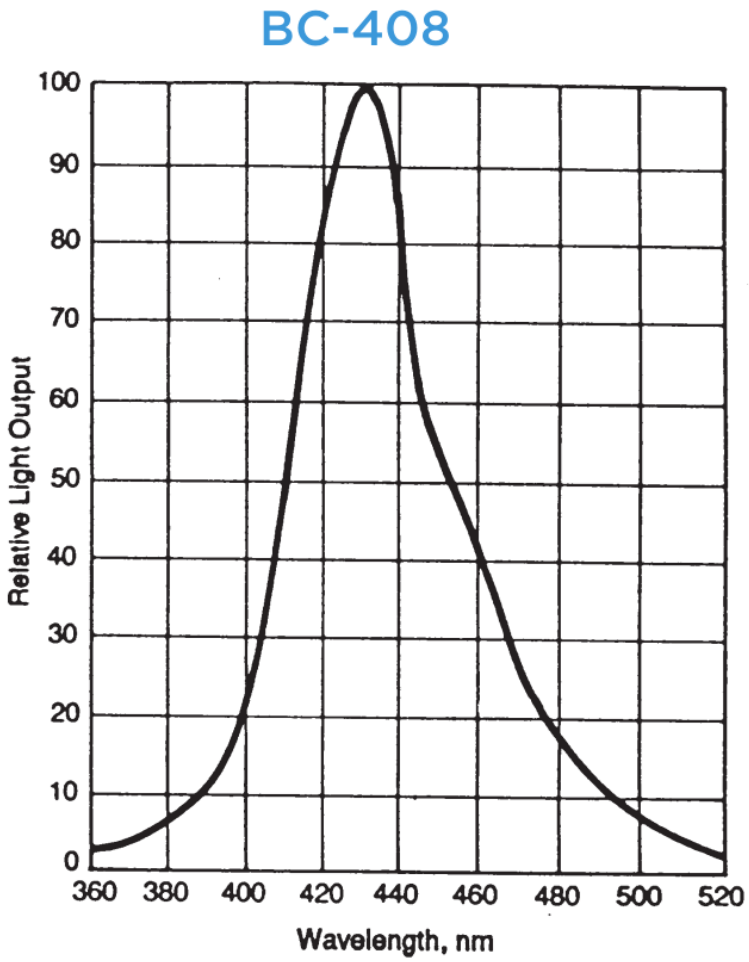


Figure 3.8: Emission spectrum of BC-408 plastic scintillators. The spectrum is peaked around 430 nm, in the blue-violet region [12].

studied: (1) back illuminated, high efficiency, low noise CMOS devices and (2) high conversion efficiency photocathode coupled to MCP coupled itself with pixel sensors such as TIMEPIX or MIMOSIS [37].

**CMOS sensor based device.** Only recently the primacy of CCDs is being surpassed by CMOS sensors for visible and ultraviolet wavelength image acquisition in scientific research.

CCDs consist of a pixelated metal oxide semiconductor whose structure is basically that of a series of closely spaced electrodes separated from an underlying semiconductor substrate by a thin insulating oxide layer [67]. Each pixel is essentially an electrode.

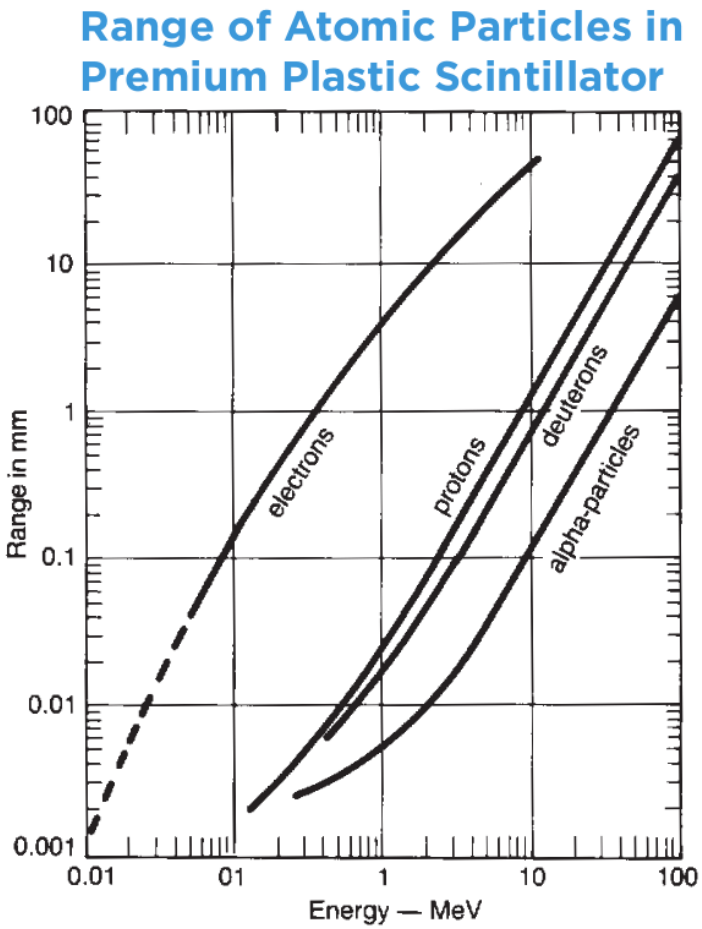


Figure 3.9: Range of different particles in BC-408 plastic scintillator. In our range of interest, proton range is between 0.2 and 30 mm [12].

When a bias voltage is applied, a depletion region is formed in the semiconductor and an amount of charge can be stored.

When exposure is complete, CCDs transfer each charge packet to a common output structure sequentially. This structure converts the amount of charge into a voltage and sends it off-chip. It is thus possible to associate the amount of charge stored into each pixel, which can be linked to the amount of light that the pixel received, to an image grey level. This camera was used, for example, in the SONTRAC experiment to obtain the images of figure 3.1.

CMOSs (complementary metal oxide semiconductors) have recently re-emerged as sensors. They promise a more compact, lower power and more radiation tolerant camera compared to CCDs. Differently to CCDs, moreover, the charge-to-volt conversion takes


Figure 3.10: First optical apparatus that will be studied as detector readout for RIPTIDE. An ASI 294MM PRO camera (right) [69] will be coupled with E30 F3.5 Macro optics (left) [58].

place in each pixel simultaneously. In a CMOS sensor, the single pixel is constituted of a photodiode and three transistors: the first one is to pre-charge the photodiode, the second one is to sense the signal voltage, the third one is to select the row. Back illuminated CMOS sensors coupled with optics are currently being studied. They are exposed to light from the back of the silicon substrate. The result is a dramatic improvement in photographic performance, including approximately double the sensitivity with respect to front-illuminated CMOS.

The first optical system under study, therefore, will make use of a back-illuminated CMOS sensor. The optical system will consist of an ASI 294MM PRO camera [69] coupled with E30 F3.5 Macro optics [58] (Figure 3.10). Having an high quantum efficiency performance in the wavelength range of emission of the scintillator (see figure 3.11), it can be used in combination with BC-408 without an important loss in the efficiency.

**MCP based device.** The complementary optical system that is planned to be studied is based on microchannel plates (MCPs), which combine suitable spatial resolution (10-100 $\mu$m) with large detection surface. A configuration which is similar to the one that will be proposed in RIPTIDE has been used to obtain the track reconstruction of electrons in [20].

These devices can be also used for real time acquisition, having a time resolution of 100-200 ps. Concerning light detection efficiency, two different photocathodes could be investigated: TIMEPIX and MIMOSIS, two high spatial and high contrast pixel readout that can also work in single photon counting mode.

A sketch of the working principle of this device is shown in figure 3.12. It consists of a photon to electron converter, an electron amplifier and an electron readout system.

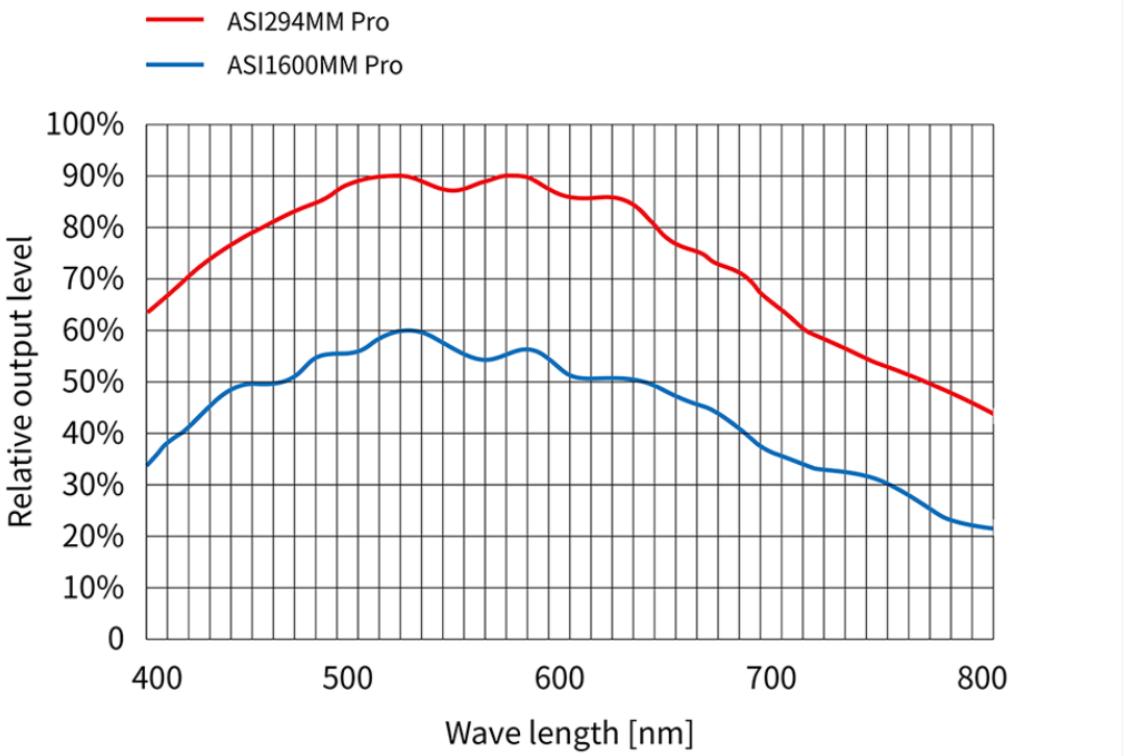


Figure 3.11: Quantum efficiency the CMOS camera as a function of the wavelength. If compared to the emission spectrum shown if figure 3.8, the wavelength of maximum emission from the scintillator correspond to 75% of quantum efficiency of the camera [69].

For photons in the visible-UV light spectrum, a photocathode is used to convert the incoming photon to an electron, while the amplifier is a microchannel plate (MCP).

MCP is essentially constituted of a set of miniaturized electron amplifiers. The single plate is made of hundreds or thousands of pores (channels) with a diameter of 5-10 $\mu$m. Each pore internal surface is covered with a semiconductor material and an high voltage (of the order of the keV) is applied to the whole plate. When a single electron enter on a pore, it perceives the potential difference and is accelerated. Each time the electron hits the channel surface, a certain amount of electron is produced. From a single electron, an electron cloud is obtained. In the MCP, the single electron is amplified to $\sim 10^3 - 10^7$ electrons with a relatively low spatial resolution of $\sim 7\mu$m.

The electron cloud is then collected by various types of readout anodes. For RIPTIDE experiment, TIMEPIX [61] and MIMOSIS [16] are being considered.

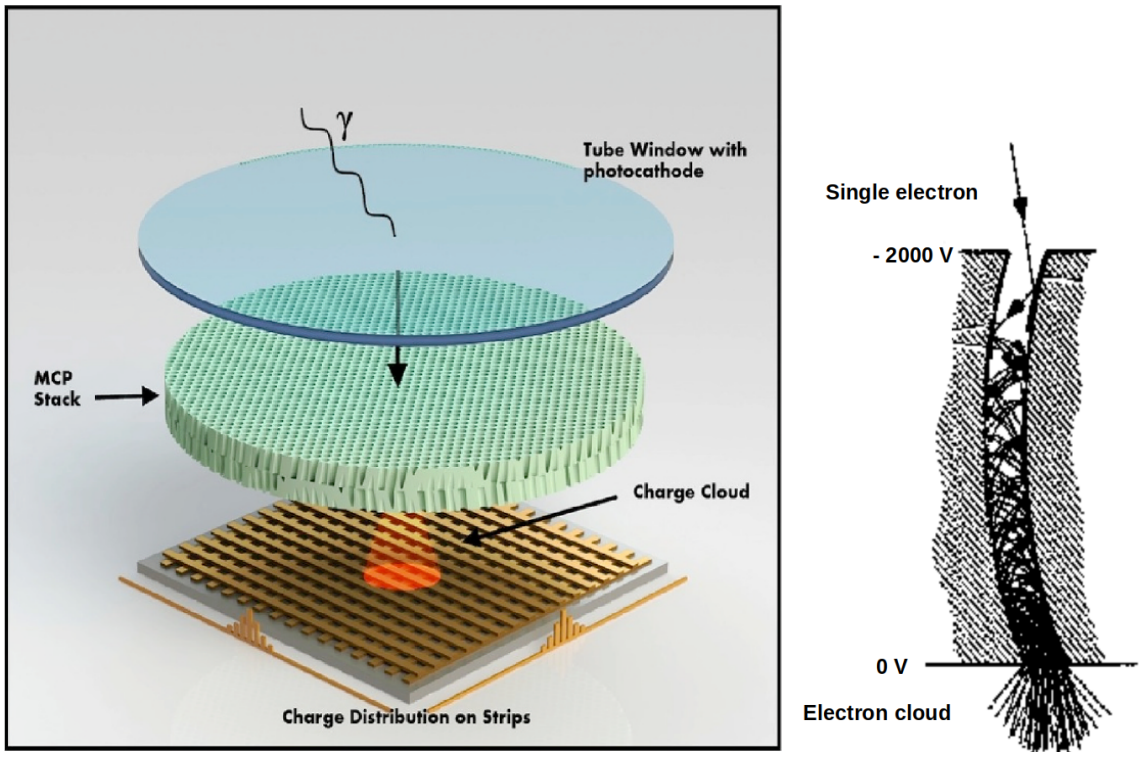


Figure 3.12: On the right, sketch of the readout system setup that could be studied for RIPTIDE. A photocathode converts the incoming photon in the visible-UV spectrum to an electron that is amplifies by the microchannel plate. The electron cloud thus produced is detected from TIMEPIX or MIMOSIS detector [61]. On left, the working principle of the single channel of a MCP is shown. From a single electron up to $10^3 - 10^7$ electrons are produced [66].

### 3.3.3 Silicon photomultiplier

Finally, a silicon photomultiplier will be used as an external fast trigger as a time reference to synchronize the cameras used to obtain the stereoscopic image. For instance, S13360-3025CS silicon photomultiplier from HAMAMATSU can be used [27].

It is a Multi-Pixel Photon Counter made of multiple Geiger mode avalanche photodiode (APD) pixels.

The single avalanche photodiode consists of a thin silicon wafer where high voltage is applied. As in conventional SiPMs, incident light generates an electron-hole pair. The application of a high reverse bias voltage, however, enable an internal current gain effect. In other words, conventional photodiodes simply convert radiation into detectable signals; avalanche ones also have an intrinsic amplification effect. Our silicon photomultiplier has specifically a photosensitive area of 3×3 mm with a pixel pitch of 25$\mu$m and 14400 pixels. It has moreover a gain of $7.0 \times 10^5$.

In Chapter 5 a systematic analysis of the functioning of the SiPM with the scintillator and the wrapping in Cinefoil is exhibited.

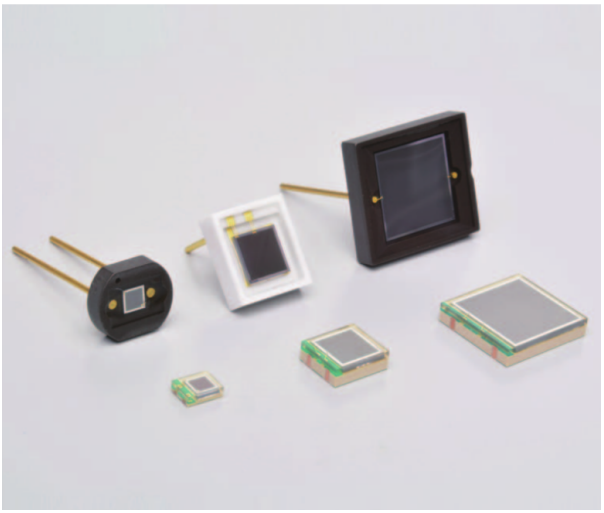

Figure 3.13: S13360 series MCCP silicon photomultipliers from HAMAMATSU [27].

# Chapter 4

# Neutron interactions in RIPTIDE scintillator: Monte Carlo simulations and analysis

In this chapter the analysis of Monte Carlo simulations of five different neutron sources at five different energies is presented, and neutron interactions inside the scintillator are described quantitatively.

## 4.1 Objectives of the analysis

In Section 2.1.3 and 3.2 we already discussed the necessity to know whether the neutron is able to interact inside the scintillator and which kind of interaction it undergoes. The small size of the scintillator implies that the majority of neutrons pass through the scintillator undisturbed. Moreover, the scintillator composition (carbon and hydrogen ratio is almost equal to one and these elements have comparable cross sections) implies that the neutron has comparable probabilities to scatter with protons or with carbon ions. It is important to make a quantitative analysis of these events because, the interaction with carbon could invalidate the measured neutron energy and direction.

A simplified version of the detector setup (including the scintillator and the neutron source) has been virtually built in Geant4. The scintillator consists of a cube of polyvinyl toluene with density 1.023 g/cc. As for the source, five different energies were simulated: 5, 10, 20, 50, and 100 MeV. Neutrons have been shot perpendicularly to the scintillator surface, in the center.

The probability of the different interactions of neutrons with the scintillator material was studied at different energies. In addition deposited energy was recorded. Figures 4.1 and 4.2 show examples of the interactions of 20 simulated neutrons inside the scintillator respectively at 5 and 50 MeV. The scintillator is centered at the origin of the frame of

reference of the system and has a side of 6 cm (spanning from -30 mm to 30 mm in each direction). The source is placed at the centre of one of the scintillator faces, just above the scintillator surface and neutron direction is perpendicular to the surface. At 5 MeV, n-C and n-p interactions are only elastic scattering. At 50 MeV, also n-C reactions occur. The products of these reactions are not visible by eye, and could be identified by the presence of a photon (in yellow). In particular, in figure 4.2 it is possible to see an event in which a neutron scatters with a carbon ion, and is then scattered with a deuterium (which is the purple line in the graph), then it made a reaction with another carbon ion with the production of a Boron-11 ion (which is not visible) and a photon (the long yellow line). Neutron-deuterium scattering is a rare event because of its poor concentration of this isotope (99% of hydrogen nuclei consist of protons, and less than 1% is $^2$H).

## 4.2 The Monte Carlo simulation

The simulation has been developed with Geant4. This software has been properly developed to study particle-matter interactions [2]. It contains all the physics models that are essential for a vast range of different types of particles interaction with matter and it can be adapted to a wide range of possible applications.

The virtual setup developed was simple: a polyvinyl toluene cube with a side of 6 cm was placed at the center of the simulation frame of reference so that the centre of the cube coincided with the origin of the system. The neutron source, on the other hand, was monochromatic and point-like, and was placed at the centre of one of the cube faces immediately out of the scintillator. Neutron initial momentum was set so to hit the scintillator perpendicularly. In this way, a non-interacting neutron would pass exactly all the thickness of the scintillator undisturbed. The simulation was performed at 5 different energy values: 5, 10, 20, 50 and 100 MeV. For each energy, $10^6$ neutrons have been simulated.

In a nuclear physics Monte Carlo simulation it is possible to store a set of information such as energy, position of the interaction, type of particle, etc. Each simulated neutron, with all its interactions inside the scintillator is called *event*. For each event, it is common to store the information of the different tracks and steps. With the name *track*, we mean the path of a single particle; with the name *step*, we mean the segments forming the path of the track. For example, an event of a neutron that is produced from the source, scatters with a proton and exits from the scintillator is made of two tracks (the neutron and the recoil proton) and three steps, one for the proton and two for the neutron (one from the source to the point of interaction, the second from the point of interaction to the point where the particle exits from the scintillator). Obviously, we are interested only on the steps and tracks that occur inside the scintillator; initial and final position of each step and the type of particle has been used to obtain the graphic visualization

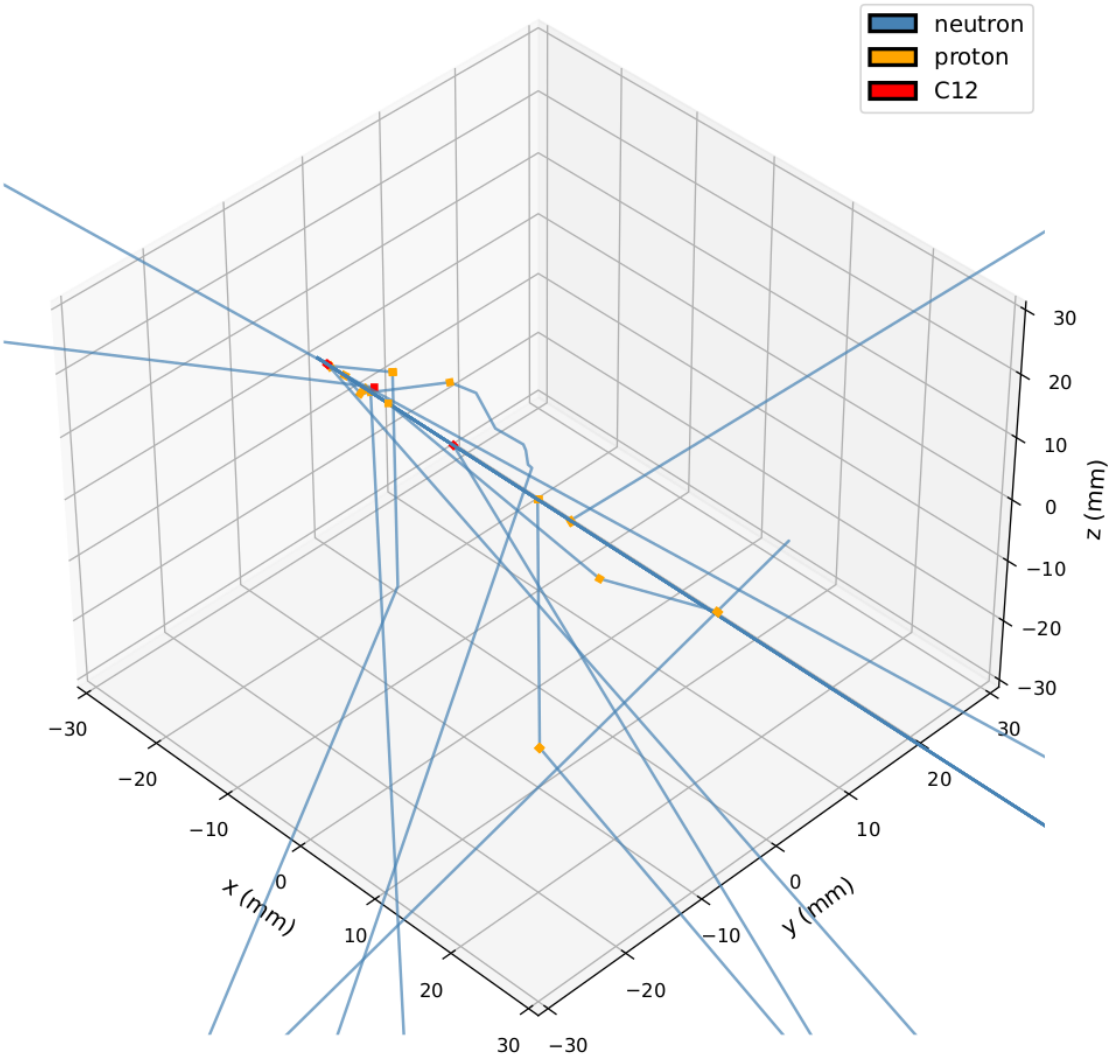


Figure 4.1: 5 MeV monochromatic neutron source through a plastic scintillator cube of 6 cm side. At these energies only elastic scattering with protons and carbon ions occurs. Among 20 source neutrons, 11 made some interactions inside the scintillator.

of the different types of event that can be seen, for example, in figures 4.1 and 4.2.

For each track, event number, track number, type of particle (neutron, proton, etc), parent and energy released along the path and flag to indicate whether the particle exits or not from the scintillator have been stored. The usefulness of the latter quantity is explained in Section 4.3.3. The parent, i.e. the particle from which the current particle is generated, was necessary to identify the interaction. The neutron from the source were labeled with parent=0, all the particles that are generated from scattering or reaction with these source neutrons are labeled as parent=1 (see figure 4.3).

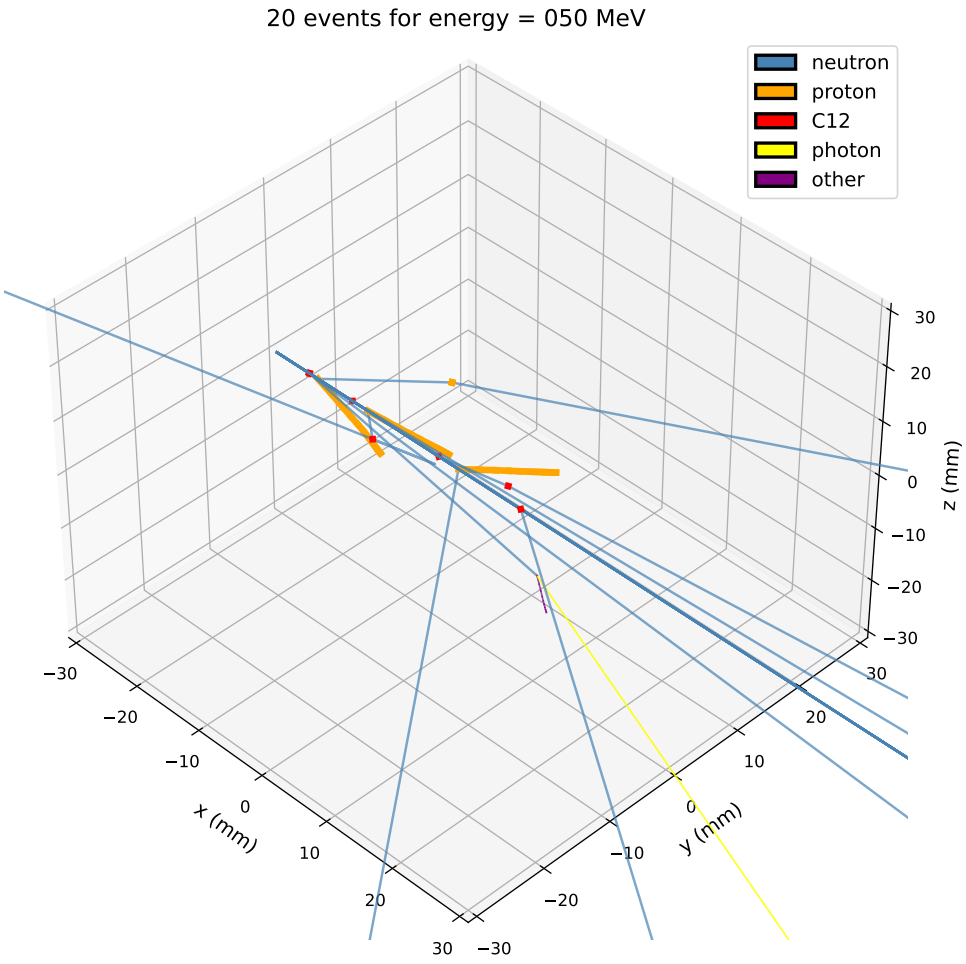


Figure 4.2: 50 MeV monochromatic neutron source through a plastic scintillator cube of 6 cm side. At these energies scattering with protons and carbon ions and n-C reactions occur. Among 20 neutrons, 8 made some interaction inside the scintillator. Note that the recoil proton tracks are longer if compared to the tracks of the 5 MeV simulation.

With these information it is possible to determine all the different types of interaction of the neutron inside the scintillator. To find a double scattering, for example, we have to search for an event in which there are three tracks, the first one is the source neutron

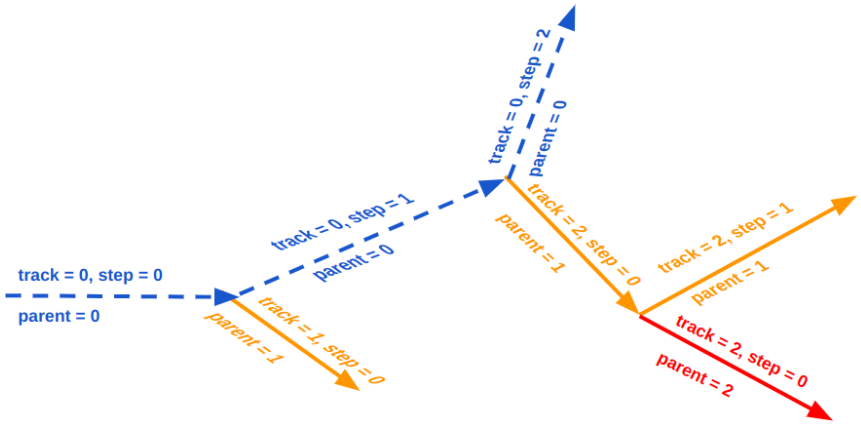


Figure 4.3: An example of track, step and parent labels as given by Geant4.

and the second one and third ones are both protons. This type of event could be both a neutron double scattering or a neutron that scatters with a proton scattering with another proton. To distinguish these two events, we must add the constraint that both protons are generated after a scattering with the source neutron (parent = 1). Other types of interactions that we studied can be found as a combination of these parameters.

## 4.3 Analysis

### 4.3.1 Types of interaction

The first information that was obtained from Monte Carlo simulations was the evaluation of the different probabilities of interaction.

As already mentioned several times, however, RIPTIDE detector aims to obtain neutron's track and energy from a single or double scattering. Therefore, our analysis focuses on these interactions and n-C scattering reaction.

Here we provide a brief description of the terminology used to classify the different interactions. Below a deeper explanation of the different types of interactions that have been studied is provided.

- **no scattering**: the neutron passes the through scintillator without interaction;
- **single, double, multiple scattering**: the neutron interacts respectively once, twice or multiple times inside the scintillator exclusively with protons;
- **fake-single scattering**: the same neutron interacts first with a carbon ion and then with a proton;

- **fake-double scattering**: the neutron interacts with a carbon ion and two protons. The sequence of interaction could be carbon-proton-proton or proton-carbon-proton;
- **other interactions**: all the other interactions that may occur (for example, single, double, multiple scattering with carbon ions, n-C reactions, etc).

In table 4.1 the probability of the different interactions that has been considered is shown as a function of the different source energies. The same data has been graphically represented in figure 4.4.

| | 5 MeV | 10 MeV | 20 MeV | 50 MeV | 100 MeV |
|---|---|---|---|---|---|
| no scattering | 0.430 | 0.534 | 0.585 | 0.740 | 0.858 |
| single scattering | 0.164 | 0.127 | 0.079 | 0.034 | 0.018 |
| double scattering | 0.071 | 0.036 | 0.015 | 0.004 | 0.001 |
| multiple scattering | 0.037 | 0.016 | 0.005 | 0.001 | 0.000 |
| fake-single scattering | 0.031 | 0.013 | 0.010 | 0.003 | 0.001 |
| fake-double scattering | 0.021 | 0.007 | 0.003 | 0.001 | 0.0 |
| other interactions | 0.246 | 0.267 | 0.303 | 0.213 | 0.122 |

Table 4.1: Probability of the different interaction of the neutron inside the scintillator at different energies. *no scattering* means that the neutrons do not interact with the scintillator; in *single*, *double* and *multiple scattering* only n-p interactions respectively with one, two or more protons are considered; for *fake single* and *fake double scattering* we mean the events that produce a signal similar to a single or a double n-p scattering, but the neutron undergoes also interaction with a carbon ion (we described these situation more deeply in Section 4.16). *Other interactions* include all different interactions that have not been mentioned above (e.g. single or multiple n-C scattering, n-C reactions, etc.) that are not useful for neutron track reconstruction.

**No scattering.** As expected, the dominant event is that of a neutron passing through the scintillator undisturbed. It increases with the increasing of the energy, from 43% for 5 MeV neutrons up to 86% at 100 MeV.

**Single, double and multiple scattering.** These terms refer to single, double and multiple (three or more) neutron-to-proton elastic scattering. The neutron, in other words, interacts only with protons, then it escapes the scintillator. From table 4.1 and figure 4.4 it is clear that, as expected, single n-p scattering is more probable than double and multiple. Moreover, for all the three types of event, the probability decreases with the increasing of the energy. Figures 4.12, 4.13 and 4.14 show an example of each different

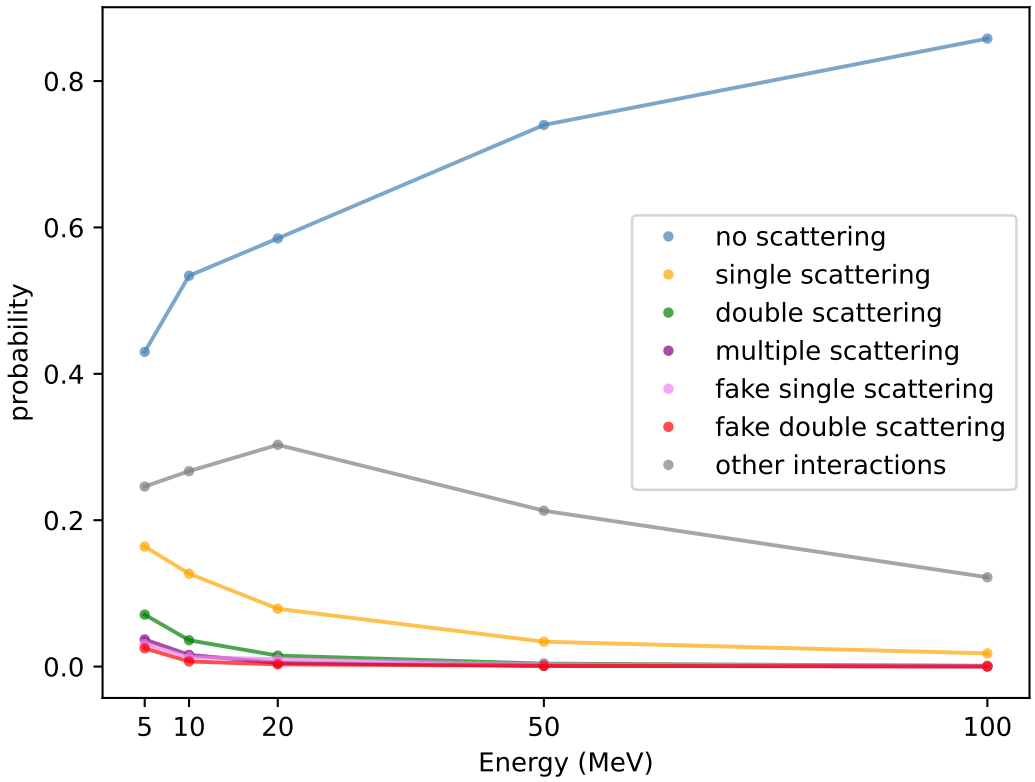


Figure 4.4: Probability of interaction as a function of neutron energy. The probability of no interaction increases with the increasing of neutron energy, while all the other decrease.

event type. From them (it is more evident in image 4.13) it can be noticed a fundamental property of n-p elastic scattering: the angle between scattered neutron and recoil proton is always right (90°) (see appendix B).

It is worth noticing that summming up the probability of single and double scattering, the efficiency can be as high as 20% near 10 MeV.

**Fake single scattering, fake double scattering.** In neutron to carbon scattering, the neutron transfers a lower amount of energy to the ion and neutrons change direction. The recoil carbon track produced from n-C scattering is often too small to be detected by the detector readout. For *fake-single scattering* we mean the case in which a neutron has a double scattering, first with a carbon ion and then with a proton. For *fake-double scattering* we mean a triple scattering with a carbon ion and two protons and the carbon

scattering is not the third event. An example of these two event are shown in figure 4.15 and 4.16.

Since the carbon track in most cases is not visible, these events could be confused with single and double scattering respectively, with a consequent error in the measurement of energy and direction of the proton (see Section 3.2).

**Other interactions.** It represents the interaction, e.g. nuclear reactions, not mentioned. Above certain thresholds, nuclear reactions with carbon could also take place. The lighter ions produced in these reactions the most of the times cannot be easily detected from the readout system because of their submillimetric range. All these events cannot be used to obtain neutron energy and track reconstruction first because equation 2.11 is valid only for protons and second because, almost always, their tracks are too small to be detected from the readout system. Some of the interactions that have been included in this class are, for example, n-C single, double and multiple scattering, n-C reactions with the formation of different products (as, for example, C(n,p)B that could be found at energies higher than 20 MeV). Of these reactions, neutron to carbon elastic scattering is the dominant event (from figure 2.3 it can be seen that the elastic scattering has the highest cross section).

### 4.3.2 Misclassified single and double scattering

Fake single and double scattering events can be exchanged by the readout system for single and double scattering respectively. It is appropriate, therefore, to estimate how many events that are classified as single and double scattering are effectively single and double scattering. These probabilities are calculated as follows:

$$Effective\ single\ scattering = \frac{single\ scattering}{single\ scattering + fake\ single\ scattering} \tag{4.1}$$

$$Effective\ double\ scattering = \frac{double\ scattering}{double\ scattering + fake\ double\ scattering} \tag{4.2}$$

The result of this calculus is shown in table 4.2. The probability to correctly classify an event, both for single and double scattering, gets higher with the increasing of the source energy. Single scattering has worse result than double scattering, especially at lower energies (at 5 MeV only 73% of the events that would be labelled as single scattering were effectively a single scattering, while at the same energy double scattering borders on 80%).

| | effective single scattering | effective double scattering |
|---|---|---|
| 5 MeV | 0.839 | 0.772 |
| 10 MeV | 0.907 | 0.822 |
| 20 MeV | 0.888 | 0.829 |
| 50 MeV | 0.919 | 0.877 |
| 100 MeV | 0.968 | 0.843 |

Table 4.2: Results of equations 4.1 and 4.2. It is the probability that an event that is detected by the detector readout system as a single (or double) scattering is effectively a single (double) scattering and not a fake-single (double) scattering.

### 4.3.3 Escaped protons

Since the proton range is related to its energy with the increasing of neutron energies also recoil proton energy increases and therefore the proton can exits from the scintillator. This is an unwanted effect because it prevents us to measure the proton energy, and thus neutron energy: if the proton is not completely stopped inside the scintillator, then it is not possible to determine its full range and thus its energy.

To obtain these probabilities, for each track it has been stored a further feature that said whether the particle ended its path inside or outside the scintillator. Then the amount of escaped protons has been counted for both single and double scattering:

$$\frac{\#\ escaped\ protons\ in\ single\ scattering}{all\ single\ scattering} \tag{4.3}$$

$$\frac{\#\ escaped\ protons\ in\ double\ scattering}{all\ double\ scattering} \tag{4.4}$$

| | single scattering | double scattering | |
|---|---|---|---|
| | | single escape | double escape |
| 5 MeV | 0.003 | 0.001 | 0.0 |
| 10 MeV | 0.008 | 0.004 | 0.0 |
| 20 MeV | 0.023 | 0.018 | 0.0 |
| 50 MeV | 0.106 | 0.017 | 0.001 |
| 100 MeV | 0.403 | 0.795 | 0.015 |

Table 4.3: Probability that recoil protons escape from the scintillator for single and double scattering. For the double scattering the probability that one and both protons escape is shown. The escaping probability increases with the energy.

These data has been reported in table 4.3. As expected, with the increasing of the energy, a larger fraction of protons is able to escape from the scintillator. For

single scattering this phenomenon gets important at 50 MeV. For what regards double scattering, both the probability that one and two protons escaped is provided. A single escape in double scattering is not significant until 100 MeV (out from the RIPTIDE detection range). At our energies, a double proton escape is undoubtedly negligible. In general, escaped protons are a side problem compared to other phenomena, such as scattering with carbon ions (fake-single/fake-double scattering), especially at lower energies. In fact, these events can be tagged experimentally.

### 4.3.4 Energy distribution of recoil nuclei

The subsequent step of our analysis was to study the energy distribution of the particles produced after the neutron interaction. In the following we show the behaviour of recoil protons and carbon ions. Concerning protons, we compared the behaviour of the first recoil protons interacting with the neutron and the following ones (second, third interaction, etc).

#### Energy distribution of recoil protons.

As already mentioned, the energy transferred from a neutron to a proton can range from zero to the entire neutron kinetic energy.

The energy distribution of the recoil protons produced after the first neutron interaction is similar to that in figure 2.2: uniformly distributed between 0 and the energy of the monochromatic source. This is confirmed for all the five energy values of our Monte Carlo simulations showed in figure 4.5. The distribution is more uniform for 5, 10 and 20 MeV. For 50 and 100 MeV other effects take place. For example, an higher amount of protons escaping the scintillator causes a deviation from the uniformity of the plot. This is more evident at 100 MeV: highly energetic protons exit from the scintillator before they lose all their kinetic energy (see Section 4.3.3) and for this reason the recoil proton energy recorded is at about 90 MeV.

In the case of multiple scattering, the distribution of the energy deposition of recoil protons is not uniform, and the probability of low energy deposition increases.

In figure 4.6 the difference between recoil proton energy distribution from single and multiple scattering is shown: as long as only the first proton scattering is considered, the energy distribution is uniform; when all the recoil protons are considered, the distribution gets exponential (with more events at lower energies).

#### Energy distribution of recoil carbon ions.

As we said, n-C interaction involves an exchange of energy lower as compared to protons. From equation 2.1, we can estimate the maximum energy of a carbon ion ($E_C$) at each energy of our simulations:

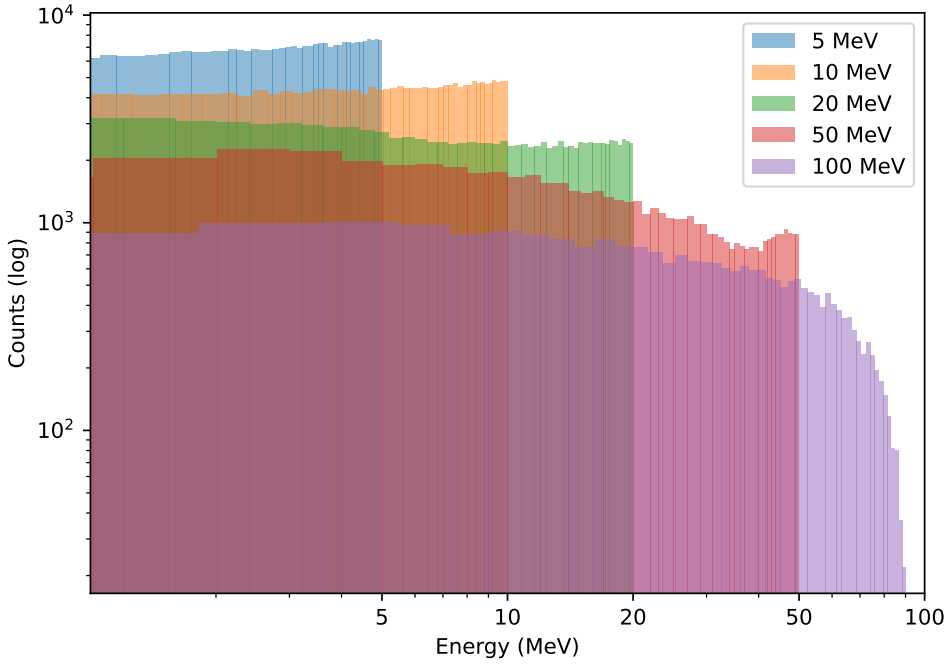


Figure 4.5: Energy distribution of recoil protons from single scattering. The energy is uniformly distributed between 0 and the neutron energy source.

- for 5 MeV neutrons, $E_C \in [0, 1.42]$;
- for 10 MeV neutrons, $E_C \in [0, 2.84]$;
- for 20 MeV neutrons, $E_C \in [0, 5.68]$;
- for 50 MeV neutrons, $E_C \in [0, 14.2]$;
- for 100 MeV neutrons, $E_C \in [0, 28.4]$.

Figure 4.7 shows a comparison of the energy distribution of all recoil carbon ions and protons for a monochromatic source of 5 MeV. The maximum of carbon energy is 1.42 MeV, as expected. A structure can be seen in the figure. It is associated to the n-C interaction.

### 4.3.5 Impact of an experimental threshold

When the energy is small, the corresponding tracks are too short and therefore they cannot be detected by the readout system. To take this into account, a threshold at 3.5

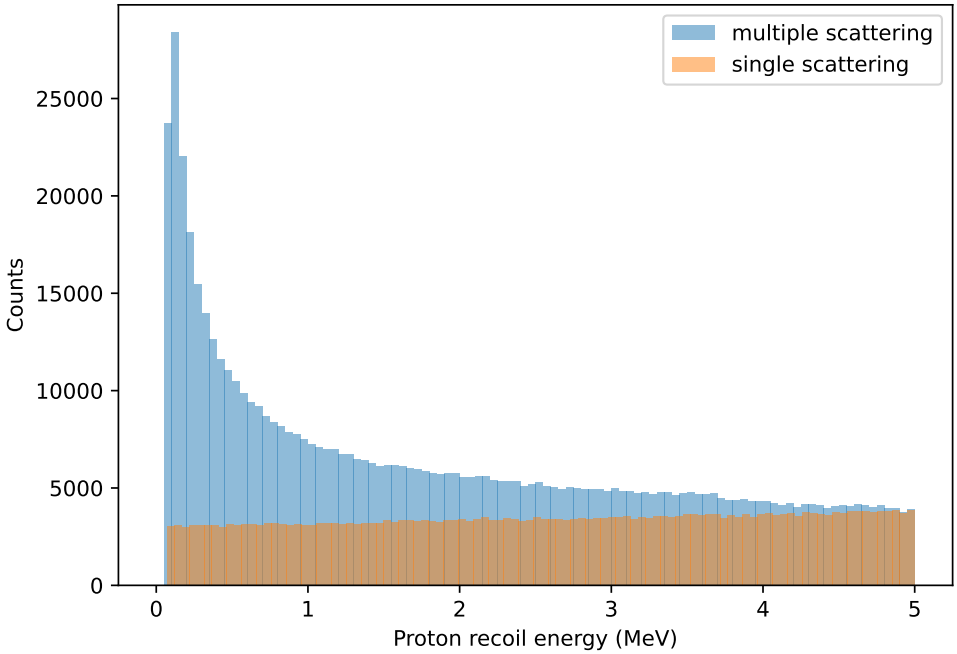


Figure 4.6: Comparison of the energy distribution of recoil protons from single scattering (orange) and multiple scattering (blue). This is the case of a monochromatic source of 5 MeV.

MeV for proton energy was included. This detection threshold corresponds to approximately 0.2 mm lenght (see figure 3.9). The resulting probability of each event to happen is shown in table 4.4.

As expected, the energy threshold strongly limits the amount of available events, especially for 5 MeV neutrons, where the range of proton energies is limited between 3.5 and 5 MeV. The effect of imposing an energy threshold is less important at higher energies. Figure 4.8 is a comparison of the different types of events with and without the energy threshold.

From the plot, it is possible to argue that the effect of the threshold is more important at lower energies. For what regards single scattering, for example, at 5 MeV the amount of protons with an energy higher than 3.5 MeV is less than 30% than all single scattering. At 20 MeV, this value reaches almost 80%.

In the case of double scattering, it is useful to count also the amount of times that only one of the protons is higher than the threshold. If the first recoil proton exceed the threshold, then this event could be used as a single scattering; if the second recoil

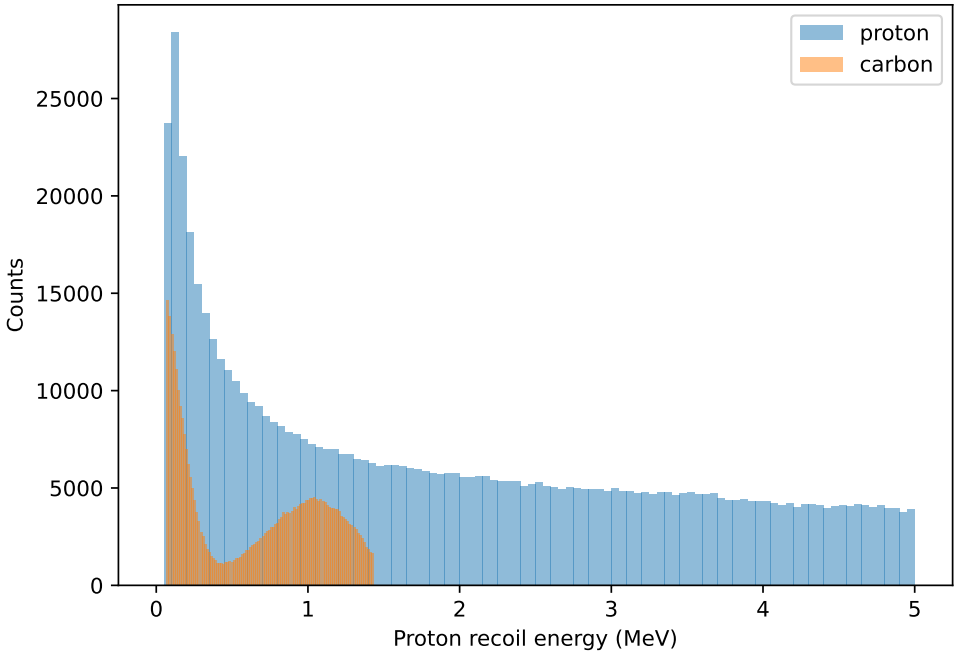


Figure 4.7: Energy distribution of recoil carbon in a comparison recoil protons. The structure in carbon energy distribution could be associated to the n-C cross section resonance between 2 and 8 MeV (see figure 2.3).

proton does, the event must be rejected. Because neutron energy is always higher for the first scattering, we expected (and found) that the first situation is more probable. In double scattering, the probability that both protons exceed 3.5 MeV threshold is also calculated. As expected, we found that the probability that the first proton exceeds threshold energy is higher than the probability that the second one does, which is itself lower than the probability that both protons are emitted with an energy larger than 3.5 MeV.

For multiple scattering, the probability that the first or that the first two protons reach the desired energies has been calculated (see table 4.4).

### 4.3.6 Including temporal information

In this last session of our analysis, we aim to study the issue from a slightly different point of view. Until now, all the events have been classified by their interactions: a neutron interacting only with a proton was a single scattering, a neutron interacting with two protons was defined as a double scattering, a neutron interacting first with a

| | 5 MeV | 10 MeV | 20 MeV | 50 MeV | 100 MeV |
|---|---|---|---|---|---|
| single scattering | 0.130 | 0.078 | 0.063 | 0.030 | 0.016 |
| double scattering | | | | | |
| $1^{st}$ proton | 0.003 | 0.028 | 0.013 | 0.003 | 0.001 |
| $2^{nd}$ proton | 0.002 | 0.006 | 0.005 | 0.001 | 0.001 |
| both protons | 0.0 | 0.002 | 0.004 | 0.001 | 0.001 |
| multiple scattering | | | | | |
| $1^{st}$ proton | 0.016 | 0.013 | 0.005 | 0.001 | 0.0 |
| $1^{st}$ & $2^{nd}$ proton | 0.0 | 0.001 | 0.001 | 0.0 | 0.0 |
| fake-single scattering | 0.005 | 0.007 | 0.008 | 0.002 | 0.001 |
| fake-double scattering | 0.0 | 0.001 | 0.001 | 0.0 | 0.0 |

Table 4.4: Probability to observe a certain event with proton energy higher than 3.5 MeV. For double and multiple scattering also the probability that the first , second and the first two protons have an energy larger than 3.5 MeV is considered.

carbon ion and then with a proton and then escaped the scintillator was a fake-single scattering, and so on. In this way, each event could be classified under one and only one type of interaction and the sum of the different events probabilities was equal to one (for each energy, the sum of all the lines in table 4.1 is equal to one). In other words, time information is added to the analysis.

However, the entire issue could be seen from a different point of view. RIPTIDE aims to obtain, from a neutron scattering with one or two protons, the direction and energy of the proton itself. If the neutron source is known, it is sufficient a single scattering with a proton to estimate the energy of the incoming particle. If the source position is not known, it is necessary that the neutron interacts at least twice with the scintillator protons. If the position of the source is known, then, we are only interested in the first *scattering center*, if the source position is not known, we want to know the first two scattering centers. This implies that, for example, an event in which a neutron collides with a proton and then makes an inelastic reaction with a carbon ion can be used to define the position of the source. Similarly, the first proton of a double or multiple scattering can also be used to determine the neutron energy when the source is known. Instead of distinguishing the various types of events, it is therefore possible to focus only on the nature of the first three scattering centers. It should be noted that in this way it is no longer possible to consider the various types of interactions as disjoint sets because, in this way, the same event can, for example, be counted for both single and double scattering. Below we report an analysis that focuses on the first, the first two and the first three scattering centers. Focusing only on the *first scattering center*, all the events in which a neutron interacted at least with a nucleus inside the scintillator, have been classified into:

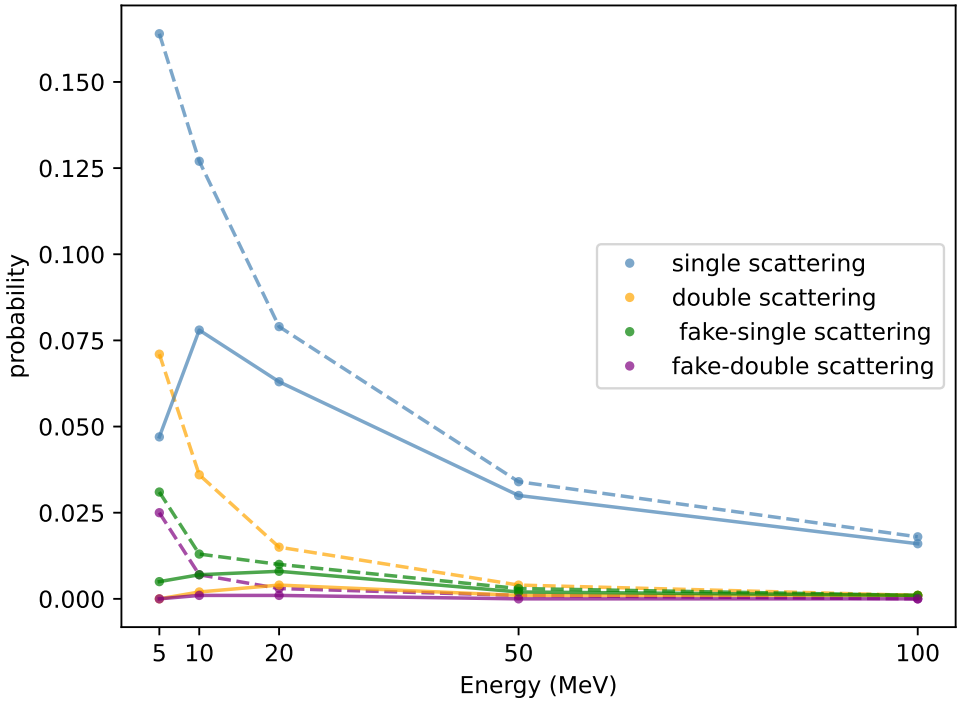


Figure 4.8: A comparison between the probability of having a type of scattering without (dashed line) and with (solid line) imposing a threshold for proton energies at 3.5 MeV. In case of double scattering and fake-double scattering both protons were required to be at energies greater than 3.5 MeV.

- **p-events**, in which the first neutron scattering is with a proton;
- **c-events**, in which the first neutron scattering is with a carbon ion. Note that these events does not necessary imply that the interaction is an elastic scattering. Also n-C reaction are included.

A comparison of the amount of proton and carbon scattering was performed and was compared with cross-section from JANIS-website databases [1]. Moreover, the effect of an energy threshold at 3.5 MeV has been studied.

Focusing only on the *first* and *second scattering centers*, of all the events in which a neutron interacted at least with two nuclei inside the scintillator, only two has been studied:

- **pp-events**, in which the neutron interacts twice with protons;

- **cp-events**, in which the neutron interacts first with a carbon ion an then with a proton.

Another possible event could be an interaction first with a proton and then with a carbon ion (*pc*). We are not interested in counting these events because they have been already counted as *p-events*. *pp-events* correspond to what we previously called double scattering, *cp-events* correspond to what we previously called fake-single scattering.

The study of the *third scattering center* had the only purpose of identifying:

- **cpp-events**, a neutron that interacts at least with three nuclei of which the first is a carbon ion and the second two are protons:
- **pcp-events**. a neutron that interacts at least with three nuclei of which the first and the third are protons and the second is a carbon ion.

Both these events correspond to what has been called previously a fake-double scattering.

**First scattering centre.**

We first focused only on the first scattering centre. We counted how many times the neutron collided with a proton and how many with a carbon ion. This evaluation has been done without imposing a lower limit to proton energy so that it was possible to compare these results with neutron-to-proton and neutron to carbon cross section. The result, in figure 4.9 (a) could be compared with cross section values from JANIS website [1]. n-C cross section has been taken from ENDF database [18], while n-p cross sections are from [36], in figure (b).

These interaction probabilities are also provided in table 4.5. In the table also the probability to find a proton with an energy larger than 3.5 MeV is shown. The similarity of the two graphs are clear.

| | p-events | p-events (Energy > 3.5 MeV) | c-events |
|---|---|---|---|
| 5 MeV | 0.342 | 0.112 | 0.226 |
| 10 MeV | 0.221 | 0.149 | 0.133 |
| 20 MeV | 0.127 | 0.101 | 0.179 |
| 50 MeV | 0.067 | 0.058 | 0.130 |
| 100 MeV | 0.040 | 0.037 | 0.057 |

Table 4.5: Probability to have an event in which the first scattering centre is a proton, or is a carbon, or is a proton with energy larger than 3.5 MeV

As for single, double and multiple scattering, a comparison of single scattering with and without threshold is provided (figure 4.10). It can be noticed, as for single scattering, that the limitation of the threshold is greater at lower energies.

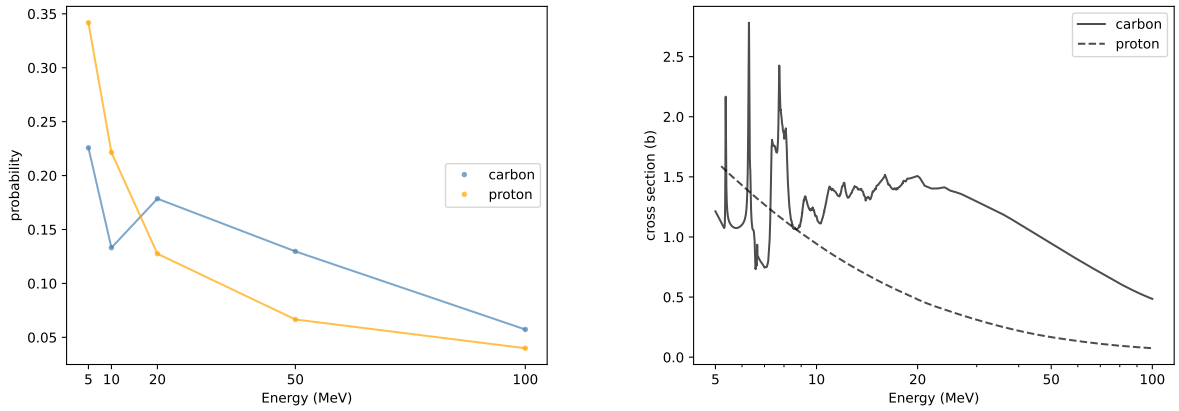


(a) (b)

Figure 4.9: (a) Probability that a neutron interacts with a carbon ion VS Probability that e neutron interacts with a proton in the first scattering center. (b) As a comparison, n-C and n-p cross sections from JANIS website databases are also provided.

In order not to be redundant, the analysis of the successive scattering centers is done by imposing the threshold on the energies of the protons. In other words, all protons are required to have energy greater than 3.5 MeV.

In the analysis of the first two scattering centers, two different cases have been studied: (1) the neutron scatters with two protons (pp) and (2) the neutron first scatters first with a carbon ion and then with a proton (cp). The events with at least three scattering have been taken into account only to identify the events that have been called in the previous section *fake-double scattering*. Two different situations are possible: the neutron sequentially collides with a proton, a carbon and a proton (pcp), and the second, in which the interaction sequence is carbon-proton-proton (cpp). The probability to find these events are shown in table 4.6. Having *cp*, *cpp* and *pcp* it is possible to evaluate effective single and double scattering. In table 4.6 these quantities are also provided.

### 4.3.7 Summary

In this chapter, we evaluated the probability to detect single and double n-p scattering inside a plastic scintillator of 6 cm side for neutron energies between 5 and 100 MeV. It resulted that the majority of the neutrons does not interact with the scintillator, and the elastic scattering probability decreases with the increasing of the energy.

It has been found that for both single and double scattering more than 77% of the events labeled as single or double scattering are effectively single and double scattering.

In addition, it was evaluated the fraction of protons escaping the scintillator. This

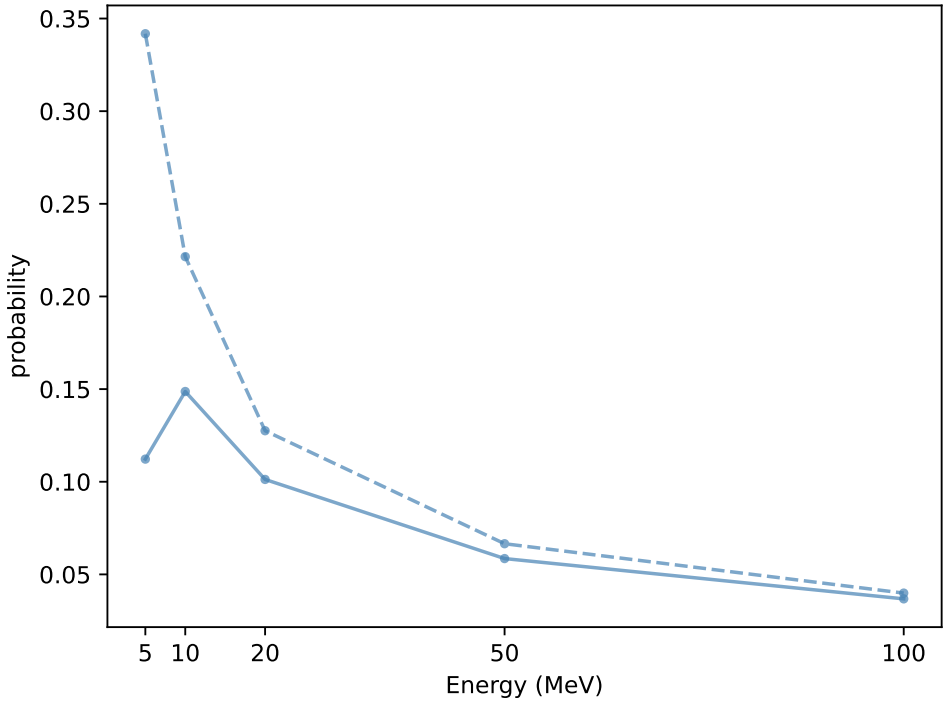


Figure 4.10: Effect of an energy threshold of 3.5 MeV on the probability that an event has a recoil proton in the first scattering centre (p-events).

| | interaction probabilities | | | | effective scattering | |
|---|---|---|---|---|---|---|
| | p-events | pp-events | cp-events | cpp/pcp-events | $\frac{p}{p+cp}$ | $\frac{pp}{pp+cpp+pcp}$ |
| 5 MeV | 0.112 | 0.0 | 0.009 | 0.0 | 0.873 | 0.0 |
| 10 MeV | 0.149 | 0.004 | 0.013 | 0.001 | 0.921 | 0.927 |
| 20 MeV | 0.101 | 0.007 | 0.012 | 0.001 | 0.897 | 0.900 |
| 50 MeV | 0.058 | 0.002 | 0.004 | 0.0 | 0.931 | 0.906 |
| 100 MeV | 0.037 | 0.002 | 0.001 | 0.0 | 0.969 | 0.962 |

Table 4.6: On left, probability to obtain the various events. On right effective single and double scattering. Note that the events thus provided si overlappano.

phenomenon was found to be a side effect up to 20 MeV energies.

Moreover, energy distribution of recoil nuclei was studied. It has been shown that the first scattered proton energy spectrum is uniformly distributed between 0 and the kinetic energy of the neutron source (figure 4.5). This is valid only for the first recoil protons because the neutron loses part of its energy during the scattering. For this reason, energy

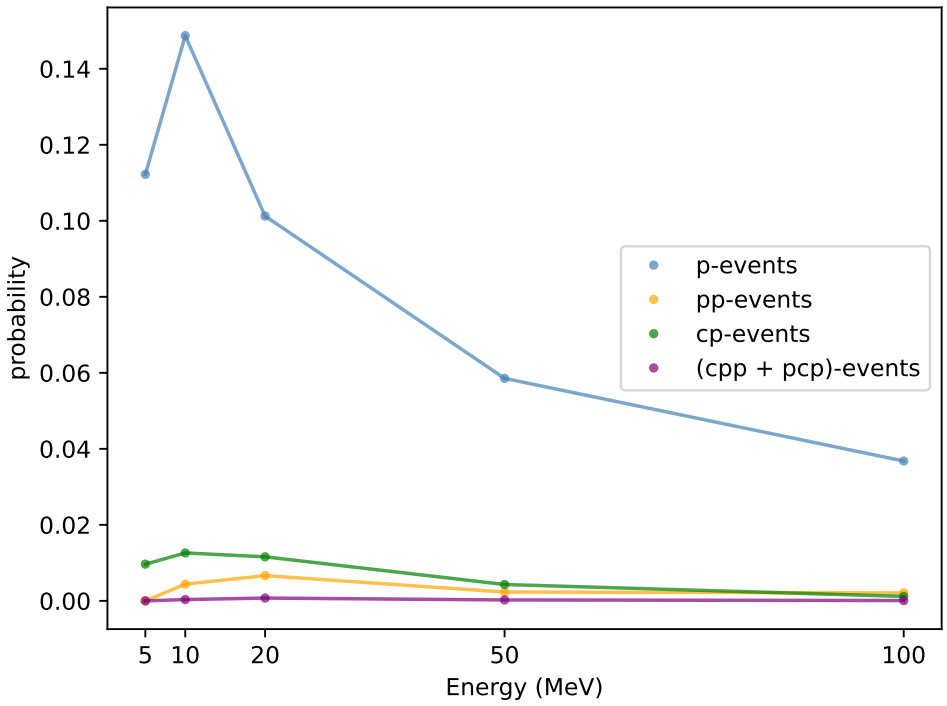


Figure 4.11: Probability of interaction as a function of the energy The label are defined as in Section 4.3.6. All protons were required to have an energy larger than 1 MeV.

transferred to the subsequent protons is lower (figure 4.6).

Concerning carbon scattering, on the other hand, it has been shown that the maximum amount of kinetic energy is limited in the region defined by equation 2.1.

Furthermore, the effect of a threshold of 3.5 MeV was studied. The probability of the different types of event (single, double, multiple scattering, fake-single and fake-double scattering) has been re-evaluated, including the probability that an event classified by the detector readout as a single(double) scattering corresponds effectively to a single(double) scattering (relations 4.1, 4.2).

Finally, the same analysis has been performed considering only the first, the second and the third scattering center: instead of looking only at single scattering, all the events in which a neutron scatter at least once inside the scintillator and in which the recoil nucleus is a proton have been considered ($p$-event); instead of looking only at double scattering, all the events in which a neutron interacts at least twice inside the scintillator and the two recoil nuclei are both protons has been considered ($pp$-event). This reasoning allows to increase the quantity of events that can be used for neutron energy and track

determination. While $p$-events probability exceeds 10% for neutron energies lower than 20 MeV, $pp$-events are particularly affected by the energy threshold, and they never reach 1% probability.

The probability to incorrectly identifying an event as $p$ or $pp$ has been finally calculated. An improvement on the classification has been found.

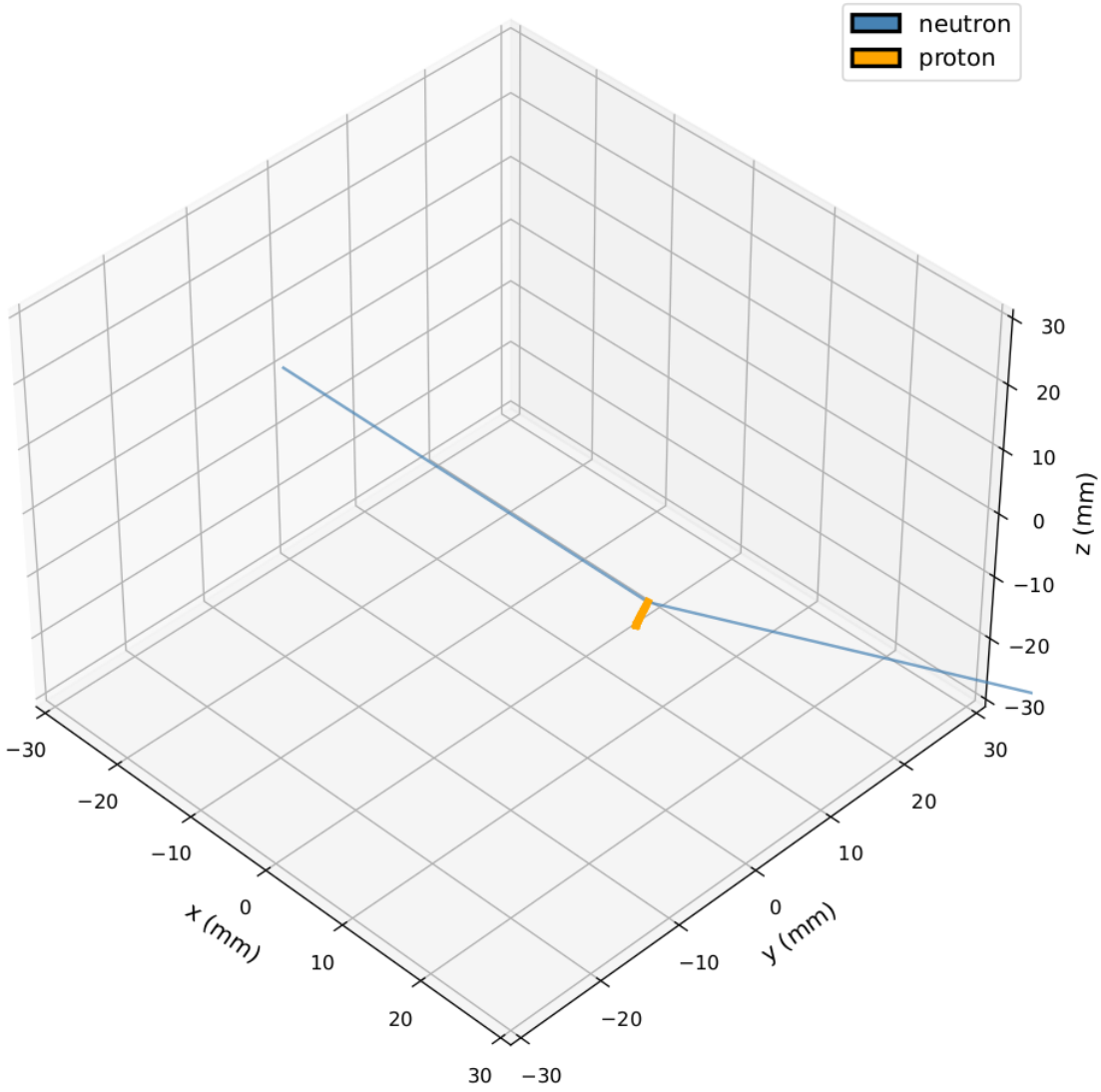


Figure 4.12: An example of single scattering.

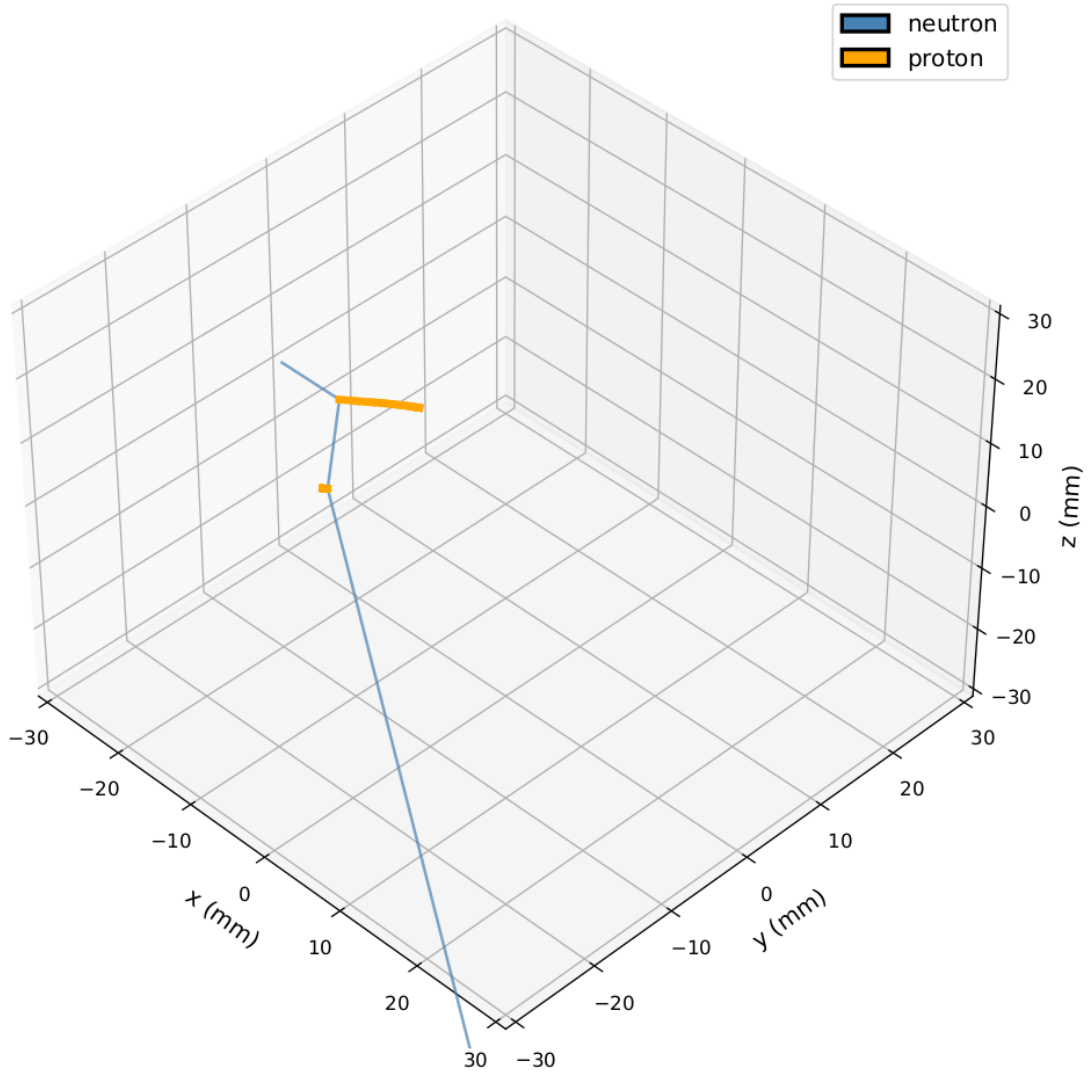


Figure 4.13: An example of double scattering. Here the 90° angle between scattered neutron and proton is visible.

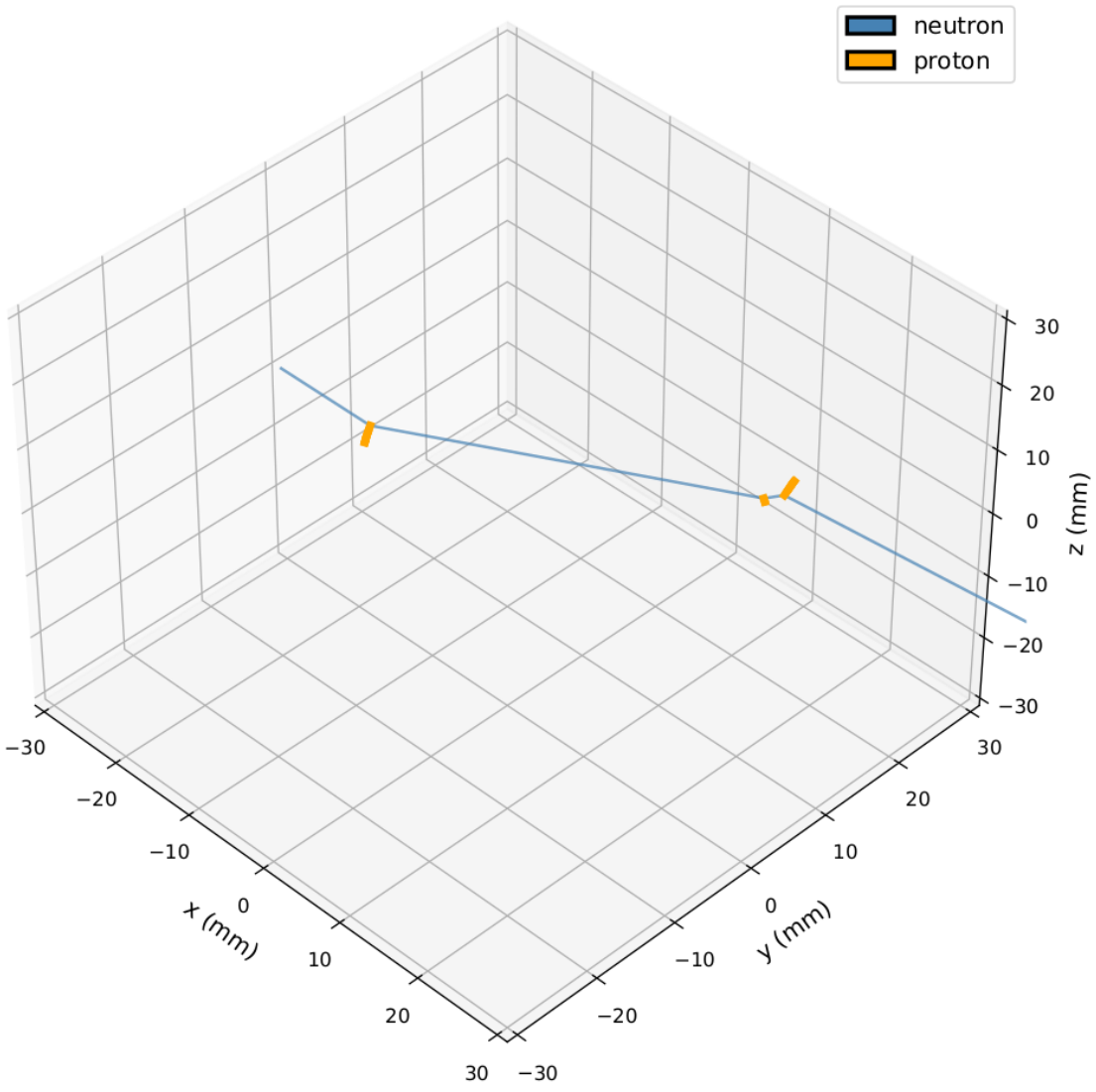


Figure 4.14: An example of triple scattering (multiple scattering)

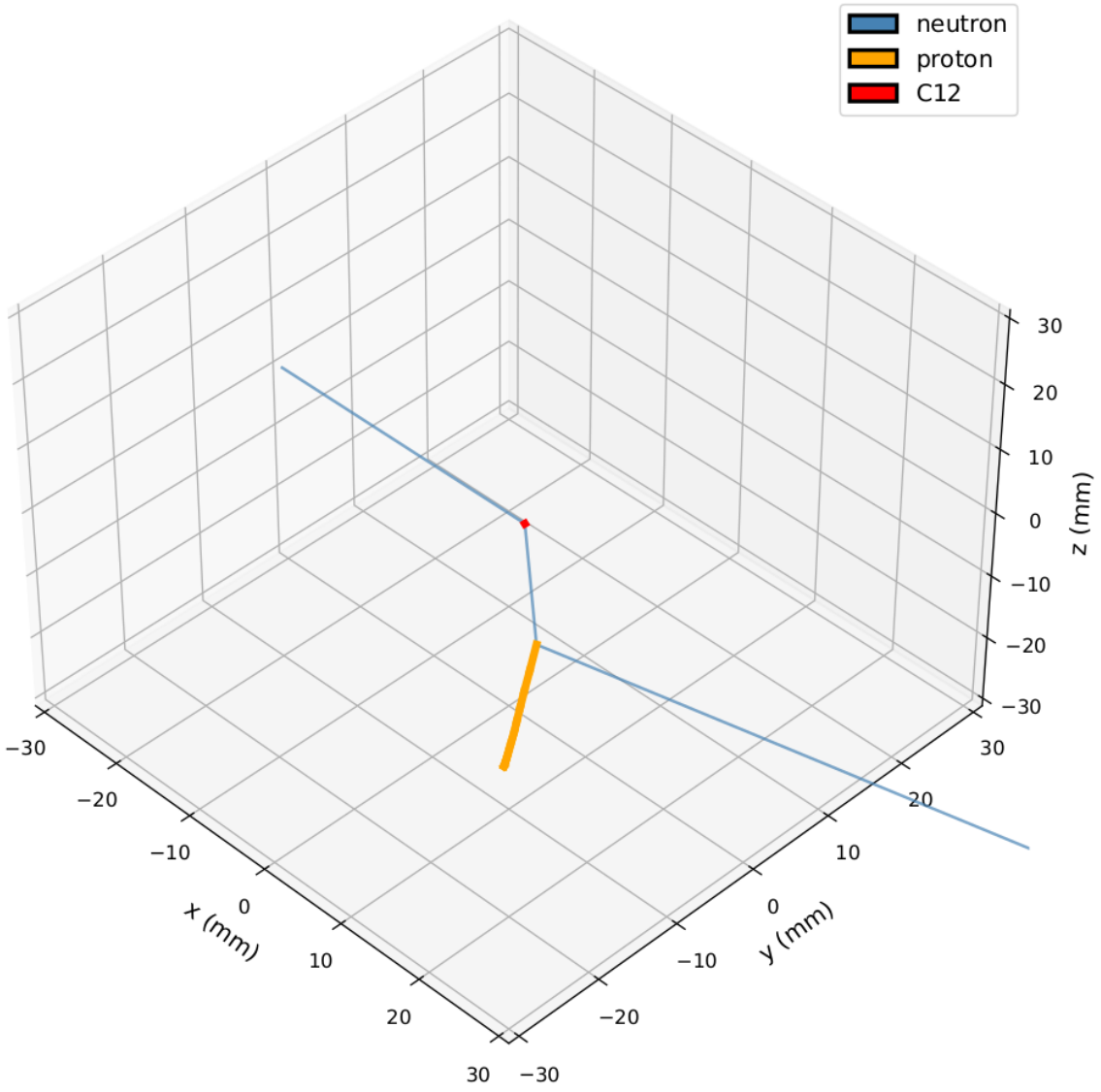


Figure 4.15: An example of fake-single scattering: the neutron first interacts with a carbon ion and then it interact with a proton. The carbon is not seen, therefore this type of event could be mistaken for a single scattering.

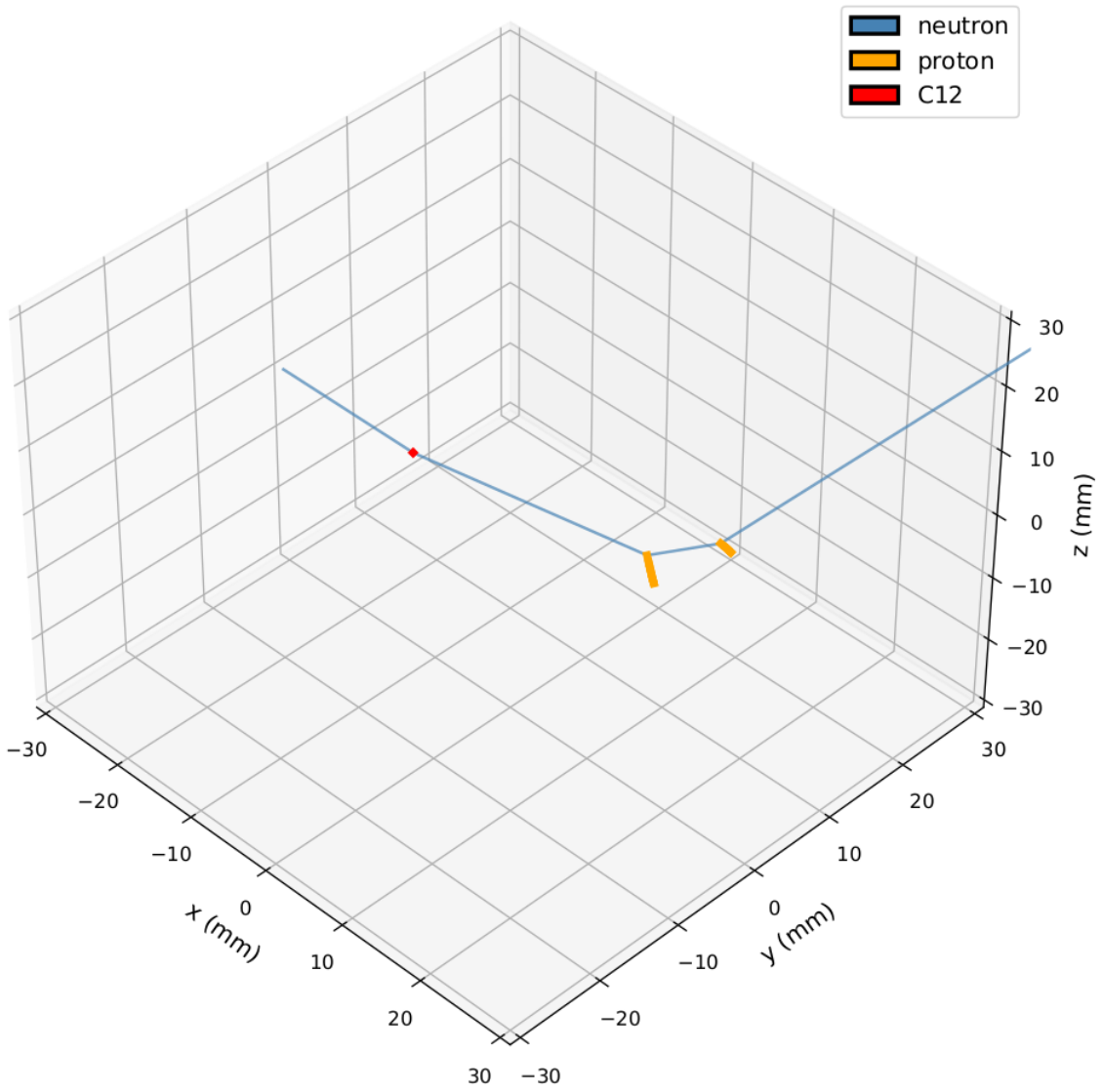


Figure 4.16: An example of fake-double scattering. The neutron interacts with a carbon ion before interacting with two protons. Generally, the carbon ion is not detected, therefore the event is misclassified as a double scattering.

# Chapter 5

# Characterization of the SiPM-scintillator system

In Chapter 3, we described the whole setup configuration of RIPTIDE detector, we outlined its neutron detection working principle, and specified the characteristics of the single components: the plastic scintillator wrapped with Cinefoil, the optical system and the silicon-photomultipliers. The achievement of this project depends on a number of aspects that must be studied: single and double n-p scattering inside the scintillator should be non-negligible, scintillation light produced by recoil protons should be detected both by the SiPM and the optical system, the response of the whole system should be sufficiently fast to permit real-time detection. In the previous chapter, neutron interaction processes inside the plastic scintillator have been studied to estimate fast neutron single and double scattering probability within the scintillator thickness. The aim of this chapter is to verify whether the SiPM can detect scintillation light in RIPTIDE configuration (with Cinefoil) and whether the signal is sufficiently fast to allow real-time detection. Future research will focus on the characterisation of the optical system.

## 5.1 Experimental setup

A simpler prototype consisting of BC-408 plastic scintillator coupled with a silicon photomultiplier, was assembled. The SiPM HAMAMATSU A13360-3025CS with a photosensitive area of 3×3 mm was placed at the center of one of the BC408 scintillator faces. An optical coupling gel was used in order to reduce photons loss due to surface discontinuities. The SiPM-scintillator system was firstly wrapped with Teflon, and after a measurement in this configuration, it was wrapped with Cinefoil and the measurement was repeated. The experimental setup is sketched out in figure 5.1. The principal characteristics of the scintillator and the SiPM were presented in Chapter 3

To detect the signal, the SiPM was connected, via a circuit board specifically prepared

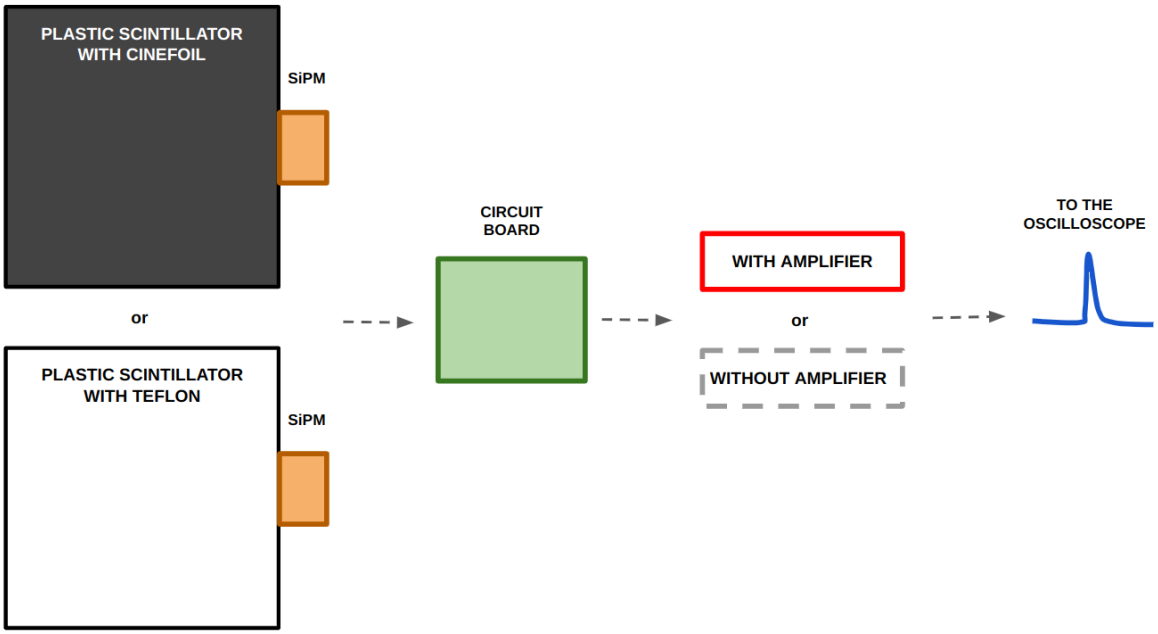


Figure 5.1: Sketch of the experimental setup in the four configurations (with Cinefoil or with Teflon, with or without the amplifier).

for the experiment, to a 5 GHz oscilloscope. A bias voltage of 57.4 Volts was set. A threshold in voltage has been set to trigger the signal acquisition. For each event, the oscilloscope showed the amplitude (Volts) as a function of the time (nanoseconds) and saved the waveform of each event in a different file.

LaNA HF Barebones by Nooelec [45] was used for the amplification of the signal. These amplifiers are able to tenfold the signal without great distortions, and invert the polarity. (see figure 5.2).

As already mentioned it is necessary to reduce photon reflection as much as possible because it increases the background in the image. Therefore, the scintillator was wrapped with a black aluminium paper called Cinefoil. In this chapter, we compare signals obtained with Cinefoil wrapping with signals obtained with a reflective coating, i.e. Teflon. Furthermore, the effect of a fast signal amplifier was studied. Signal acquisition was, thus performed in four different configurations: with Cinefoil or Teflon wrapping and with or without the amplifier. The aim of the measurements was to demonstrate that SiPMs are able to detect the passage of charged particles in a sufficient fast way so to work as a trigger for the acquisition system. In the rest of the chapter, the different setups will be identified by the following abbreviations:

- **TNA:** the scintillator is wrapped with Teflon and the signal is not amplified;

- **TA:** the scintillator is wrapped with Teflon and the signal is amplified;
- **CNA:** the scintillator is wrapped with Cinefoil and the signal is not amplified;
- **CA:** the scintillator is wrapped with Cinefoil and the signal is amplified.

The characterization of the SiPM-scintillator setup has been performed using cosmic muons. Since their discovery in 1911 [47], cosmic rays have been used as an always available source for high energetic particles in almost all physics laboratories, and the majority of cosmic charged particles reaching sea level are muons.

The setup (scintillator and cosmic muon source) was then reconstructed with the Geant4 toolkit. To simulate cosmic muons, the CRY library was used [26]. The purpose of the simulation was to study the energy deposited by cosmic muons inside the scintillator. In this way, it was possible to compare signal amplitudes (Volts) experimentally measured with the energy deposited by the muons in the scintillator (MeV).

In the following paragraph, we present a brief overview of cosmic muons characteristics useful to understand energy deposition inside the scintillator and to clarify the analysis we made of the muon source generated with CRY.

### 5.1.1 General characteristics of cosmic muons at sea level

Muons are the most abundant energetic charged particles at sea level. They are produced at an altitude of 15 000 meters, and reach sea level with an average energy of 4 GeV [23]. Their intensity has a dependence on the zenit angle that goes like:

$$I = I_v cos^2\theta_z \tag{5.1}$$

where $I_v$ is the intensity of muons reaching Earth surface perpendicularly and $\theta_z$ is the zenit angle, i.e. the angle of inclination with respect to the vertical direction.

Muons are secondary cosmic rays produced by the interaction of primary cosmic radiation (mainly protons, $\alpha$ particles and heavier nuclei) and the atmosphere. More specifically, these interactions produce mainly pions ($\pi^0$, $\pi^+$ and $\pi^-$), whose decay products are muons. More in detail:

$$\pi^+ \rightarrow \mu^+ + \nu_\mu \tag{5.2}$$
$$\pi^- \rightarrow \mu^- + \nu_\mu \tag{5.3}$$

Similar quantities of $\mu^-$ and $\mu^+$ reach the Earth (charge ratio is approximately equal to one). In 1990, Gaisser introduced a formula describing cosmic muons flux as a function of the energy and the zenit angle [21]. This formula is a good approximation for muons at

high energies ($E_\mu > 100/cos(\theta)\ GeV$) while it does not work properly at lower energies. Therefore, we used the CRY source in Geant4, since it was developed for this purpose. For the analysis of source distribution we used the data provided by Rastin in 1984 [50].

Finally, it is worth mentioning that generally muons at sea level are at the minimum of ionization. Therefore, their energy loss is almost constant (2 $MeVcm^2/g$).

## 5.2 Experimental data analysis

In this section we present the analysis of the signals acquired by the oscilloscope in the four configurations.

### 5.2.1 Qualitative analysis

An example of the shape of the signals acquired by the apparatus in the four different configurations is shown in figure 5.2. A steep rise is followed by an exponential fall (the contrary in the amplified case: a steep fall is followed by an exponential rise). However, some dissimilarities between the four acquisition setups can be noticed. The most visible difference is the effect of the amplifier: it inverts the polarity. In addition, the amplifier is able to tenfold the acquisition signal. Along the falling edge of CNA apparatus signals, a slight change in the slope can be seen. This is caused by the intrinsic RC circuit inside the silicon photomultiplier. Teflon signals are larger with respect to Cinefoil ones. This is because photons produced by the transit of charged particles could be reflected multiple times by the scintillator surfaces before being detected. This phenomenon produces a smoothing of the signal.

To visualize the main difference between the signals, a comparison of the overall shapes for the four configurations of the apparatus is shown in figure 5.3. Each line has been obtained by making the average, for each point in time, of the amplitude of all the signals of an apparatus setup (CNA, CA, TNA, TA) Clearly, the average has been performed after cleaning the dataset from spurious events (e.g. electronic noise). The description of the procedure is in Section 5.2.2. In this way, it was possible to highlight signal general characteristics due to the different setups.

In general, risetime is comparable for all the different signals. Teflon has the effect of smoothing the peak and stretching the falling time. As expected, Teflon signals were higher as compared with Cinefoil ones, as a result of an higher amount of photons that reach the SiPM.

In figure 5.4, two different characteristics of the signal shape are highlighted. In figure (a), a comparison of CA and CNA acquisition is shown. Signals have been normalized to highlight the similarities. It can be noticed that the amplifier is able to amplify the signal without distorting its shape: it can be noticed that the rising edge and the exponential decay are comparable. Figure (b), instead, is a comparison between TNA and CNA.

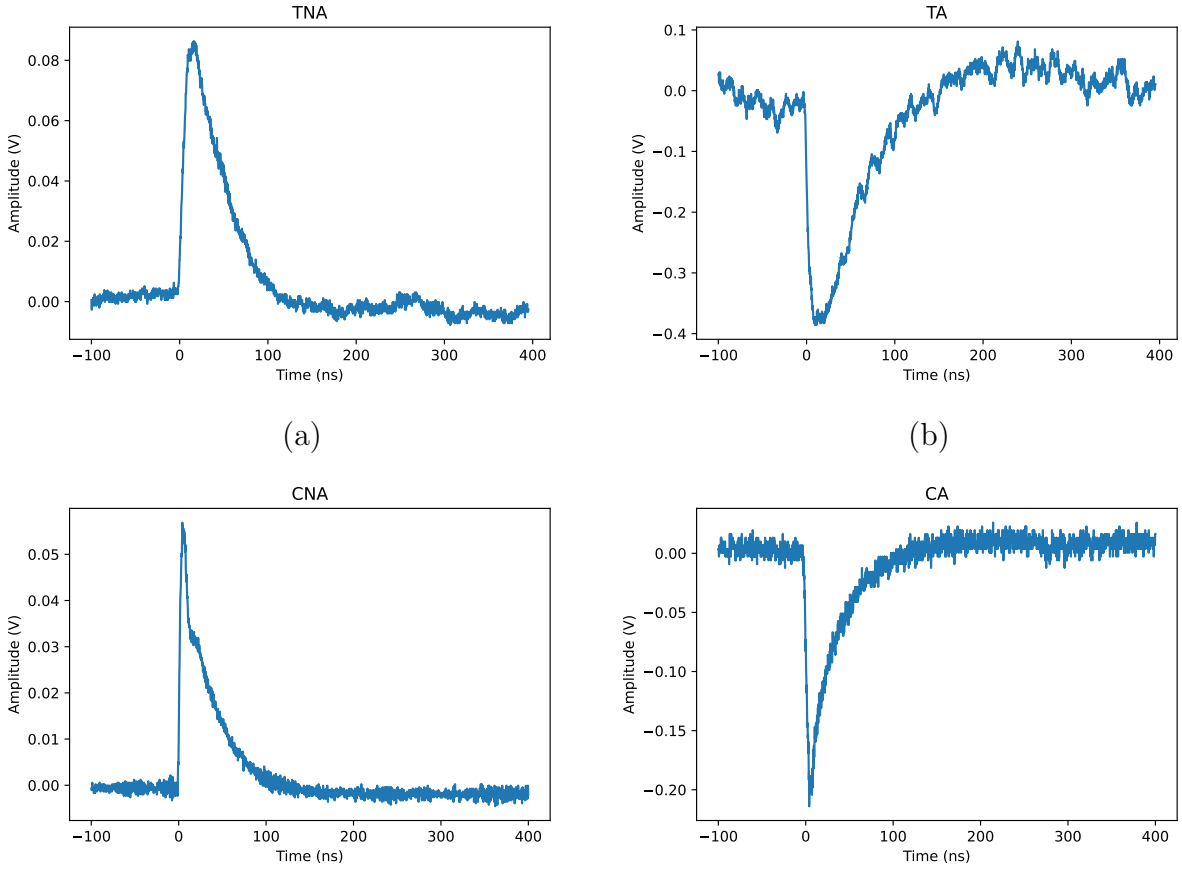


Figure 5.2: Typical signals acquired by the scintillator in the four different acquisition setup: (a) TNA, with Teflon without the amplifier; (b) TA, with Teflon with the amplifier; (c) CNA, with Cinefoil without the amplifier; (d) CA, with Cinefoil with the amplifier.

Teflon signals are higher in voltage and longer in time as compared to Cinefoil ones: the signal acquired with Cinefoil is on average a third than the one acquired with Teflon.

### 5.2.2 Quantitative analysis

For each acquisition, the moving average was used to highlight signal shape and easier distinguish signal from noise. The moving average is a technique that is commonly used in time analysis and it allows one to reduce the fluctuations. In this calculation, a time window is chosen (in our case we had a signal of around 180 ns and we used a 2 ns time window). The window is used as a time interval within which the mean of measures is

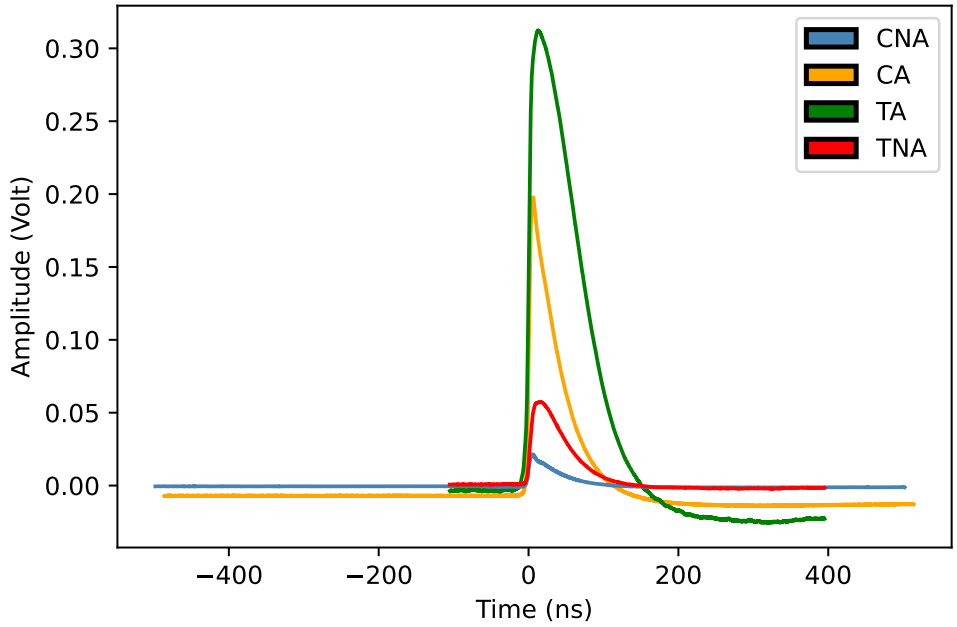


Figure 5.3: Overall signal shapes for the different acquisition setups (CNA, CA, TNA, TA).

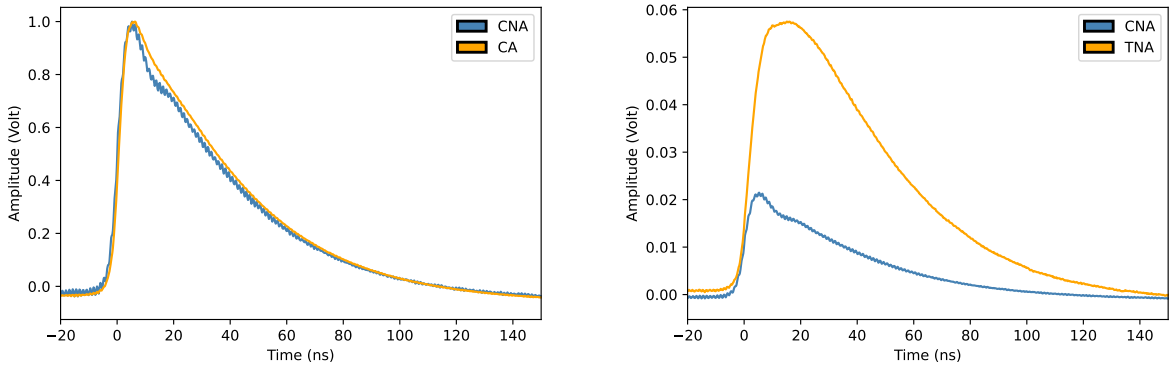


(a) (b)

Figure 5.4: (a) Comparison of CA and CNA (normalized). (b) Comparison of TNA and CNA (not normalized).

computed. As the word 'moving' suggests, the window is placed first at the beginning and it is slided through the whole signal. For each point, the mean is calculated. Obviously,

the larger is the time window, the smoother is the signal. With this technique, a local mean for each point is obtained and thus, the output of this operation will have a lower noise than the original signal (see figure 5.5).

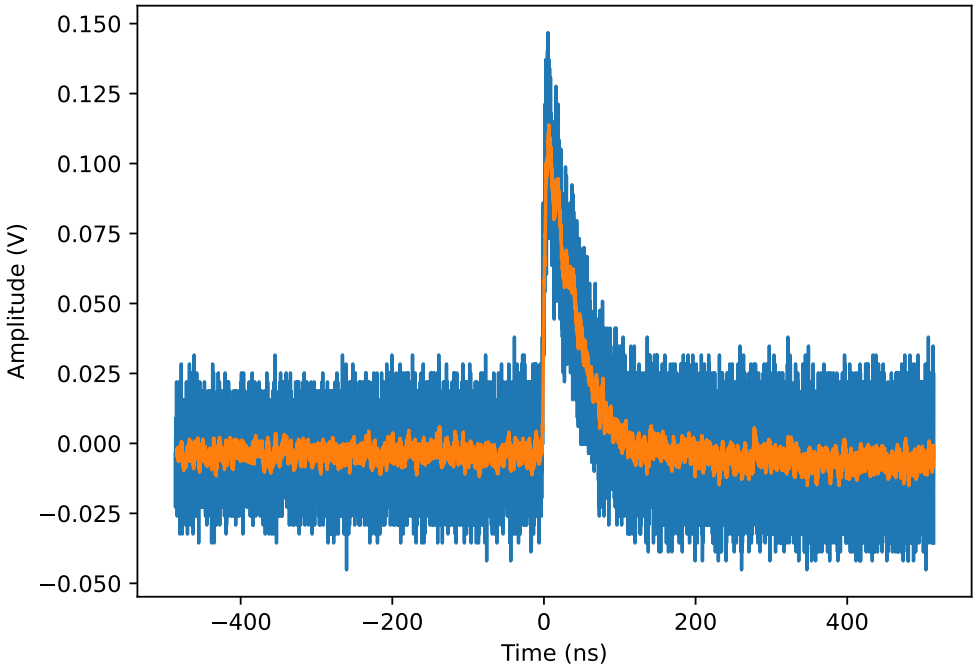


Figure 5.5: Effect of the moving average on noise reduction.

Two separate parameters have been used to filter out spurious signals: a threshold at lower amplitudes and the ratio between noise baseline and the maximum of the signal ($A_{max}/\sigma_{noise}$). Noise baseline has been calculated as the standard deviation of the values of amplitude before the signal, while $A_{max}$ is simply the signal maximum.

The parameters have been chosen separately for the different setup configurations. Moreover, it has been found that, in the CNA setup, some peaks were saturated, and therefore they were discarded.

Once the data were cleaned up, we extracted the basic features of the original signals: amplitude, noise baseline, risetime, decaytime FWHM, and FW10M, because the moving average has the effect of smoothing the signal. A graphic description of features extracted is given in figure 5.6.

To obtain peak height, first the position of the peak has been identified, then its amplitude has been computed as the difference between its amplitude and the baseline

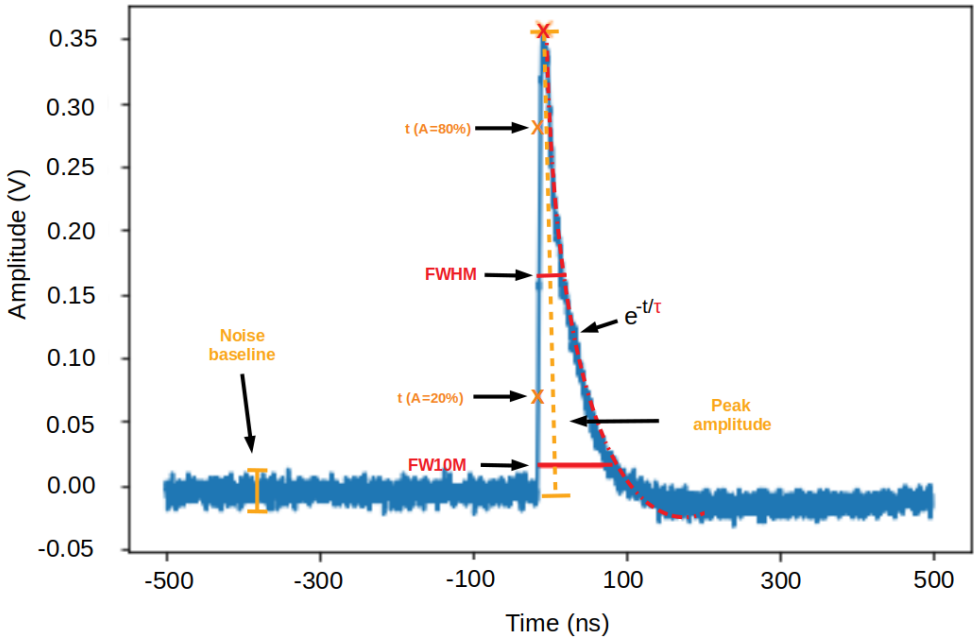


Figure 5.6: Signal parameters used in the analysis.

mean amplitude ($A_{peak} - A_{baseline}$). Signal risetime was defined for each event as the distance in time of the positions where the signal reached 20% and 80% of $A_{peak}$:

$$\Delta T = t_{(A=0.8A_{peak})} - t_{(A=0.2A_{peak})} \tag{5.4}$$

After the peak reaches its maximum, the signal experiences an exponential decay, and an exponential fit was performed ($e^{-t/\tau}$) to the falling edge of each signal from which decay time ($\tau$) was obtained. Finally, full width at half maximum (FWHM) and full width at 10% maximum (FW10M) were measured for each signal.

Mean and standard deviation of all these quantities are provided in table 5.1.

From the data in table 5.1, it is possible to notice some of the features we anticipated in Section 5.2.1. The amplifier increases the signal amplitude by about a factor ten, without great difference in risetime and falling time. This is especially evident between CA and CNA: peak amplitude passes from 0.02 to 0.2 V, but risetime and decay time do not change noticeably. Furthermore, Teflon signals have higher amplitudes if compared to Cinefoil and the signals are longer in time. Teflon wrapping spread the signal, as is especially evident for FWHM and FW10M.

Except for peak amplitude, the other distributions can be roughly compared to a

| | Peak amplitude (V) | Noise baseline (mV) | Risetime (ns) | Decay time $\tau$ (ns) | FWHM (ns) | FW10M (ns) |
|---|---|---|---|---|---|---|
| CNA | $0.02 \pm 0.01$ | $0.7 \pm 0.2$ | $3 \pm 1$ | $39 \pm 4$ | $150 \pm 40$ | $490 \pm 80$ |
| CA | $0.2 \pm 0.1$ | $5.4 \pm 0.4$ | $3 \pm 1$ | $39 \pm 4$ | $160 \pm 40$ | $490 \pm 60$ |
| TNA | $0.05 \pm 0.04$ | $1.5 \pm 0.3$ | $6 \pm 3$ | $42 \pm 6$ | $230 \pm 30$ | $530 \pm 90$ |
| TA | $0.4 \pm 0.1$ | $14 \pm 4$ | $5 \pm 3$ | $60 \pm 15$ | $310 \pm 70$ | $700 \pm 130$ |

Table 5.1: Mean and standard deviation of signal parameters resulting for the different acquisition setups.

normal distribution. In figure 5.7, risetime and falling time distribution of CA and CNA are shown.

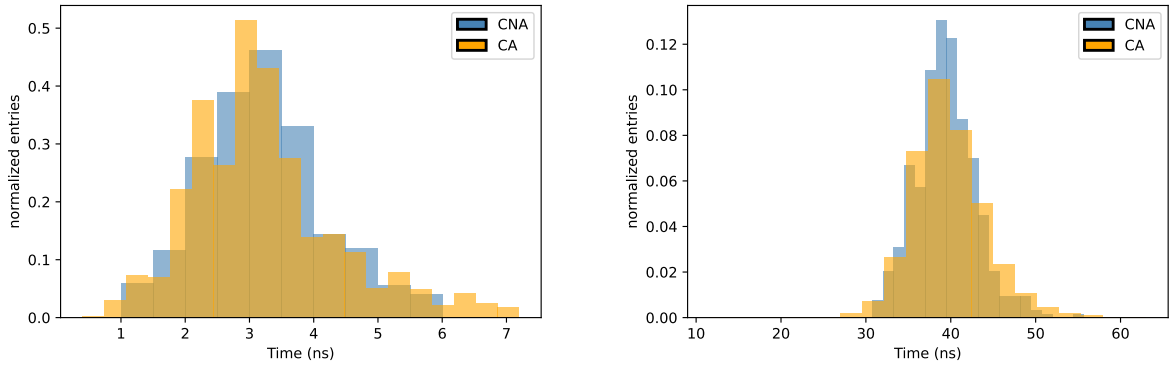


(a): risetime (b): decay time ($\tau$)

Figure 5.7: Comparison of CA and CNA (a) risetime and (b) decay time ($\tau$) distribution.

Below (figure 5.8), we provide peak amplitude distribution for the amplified and non amplified setup with Cinefoil (CA and CNA). In Section 5.3.3, these values will be compared with the result of the Monte Carlo simulation.

## 5.3 Monte Carlo simulations

Experimental data have been compared with Monte Carlo simulations. For this purpose, a model of our experimental setup has been built in Geant4 environment. The geometry of the scintillator is the same used in reality, and cosmic muons were simulated with the CRY library [26]. It is a library developed by Lawrence Livermore National Laboratory

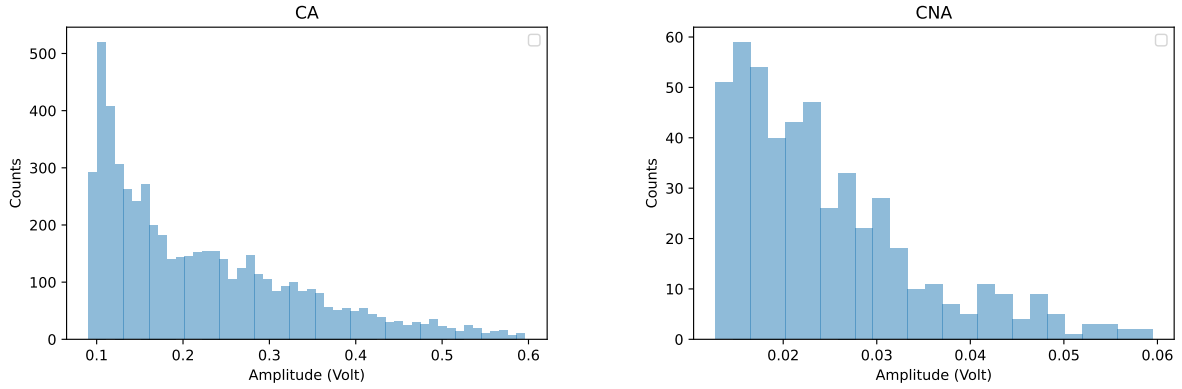


(a) (b)

Figure 5.8: (a) Cinefoil amplified peak amplitude distribution. (b) Cinefoil non-amplified peak amplitude distribution.

for the simulation of cosmic rays that reproduces the behaviour of cosmic radiation at determined spatial and temporal coordinates. To run the simulation, date, latitude, and altitude (0,2100 or 11300 m above sea level) of the experiment were defined.

### 5.3.1 Benchmarking the CRY source

CRY developers provided a study of the agreement of the library with experimental data [25]. However, we chose to assess the goodness of the source simulated with CRY. We thus generated $10^6$ events at an altitude of 0 meters above sea level, with the latitude of Bologna (44.5°) and we selected the date of the experiment (8/4/2022). We, then, verified that the characteristics of this source were comparable with the characteristics of cosmic muons at sea level described before (Section 5.1).

At first we measured charge ratio, obtaining $\mu^+/\mu^- \sim 1$. Then, the relation $I = I_v cos^2\theta_z$ was verified with a linear fit of our data (for simplicity we preferred to make our data linear instead of making a quadratic fit). From graph 5.9, the goodness of the relation is visible. We obtained a slope of $1.06 \pm 0.02$.

Finally, it was verified that the behaviour of the source was the same of experimental data. We used the data provided by Rastin in 1984 [50], to compare with (see figure 5.9).

### 5.3.2 Muons energy deposition in RIPTIDE scintillator.

Once the reliability of the source was verified, a Monte Carlo simulation of the muon source with the scintillator was run.

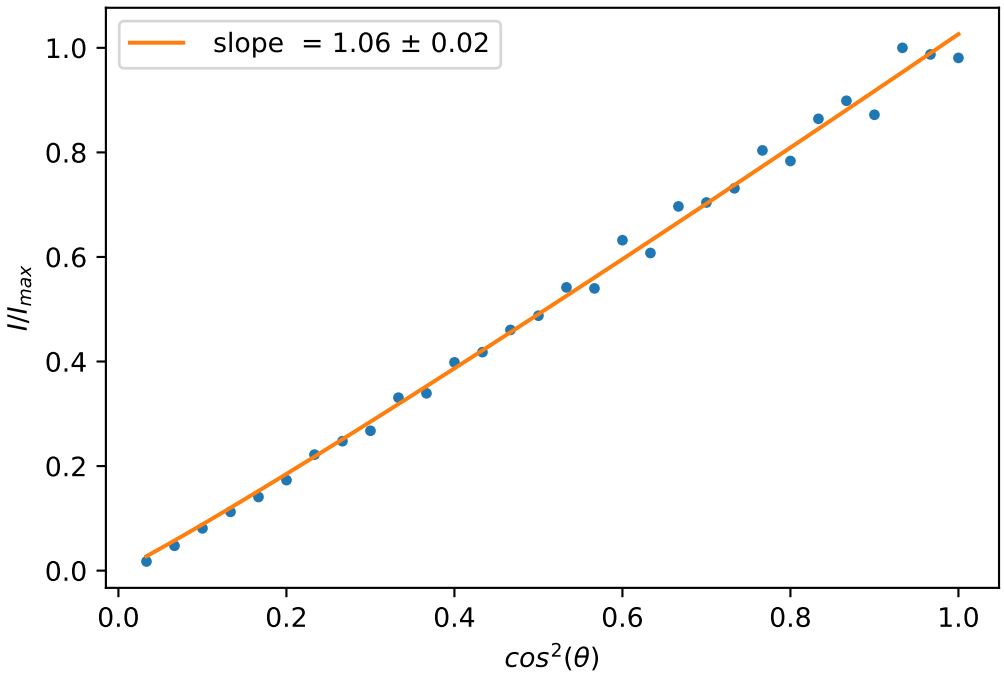


Figure 5.9: Distribution of cosmic muons with respect to the zenit angle. If $\theta = 0$, muons are perpendicular.

Muons were generated from a squared plane of 1 meter side placed at 0 meters above sea level (centered in the origin of the frame reference of Geant4). The cubic scintillator has been shifted 3 cm down with respect to the simulation of Chapter 4 in order to be entirely below the source. Figure 5.11 shows a sketch of the muons passing through the scintillator, where the chaotic distribution of the source produced by CRY can be appreciated. Being charged, muons can interact with the scintillator electrons, and therefore, some electrons can be obtained (see figure 5.11).

For each event, the energy released by each particle inside the scintillator has been stored. We were interested in the total energy released by a single event. Therefore, if an event consisted of many tracks (e.g. the source muon plus, say, a scattered electron), the energy deposition of the two tracks was summed up.

In the energy range at which they reach sea level, cosmic muons are around their minimum of ionization[1] and lose approximately 2 $MeV\text{cm}^2/\text{g}$. Our scintillator has a density of approximately 1 $\text{g/cm}^3$ and a side of 6 cm. Therefore, we can estimate that the amount of energy released for a muon passing vertically trough the scintillator is

[1] see appendix A

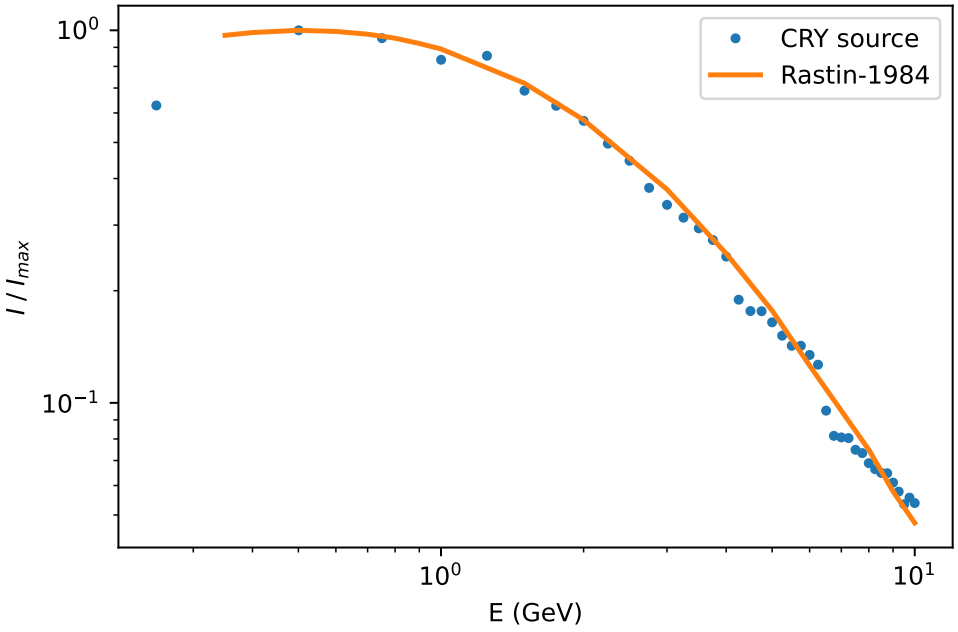


Figure 5.10: Comparison between the energy distribution of the muons produced with CRY-library and the experimental data measured by Rastin [50].

approximately 12 MeV.

Muons have larger probability to hit perpendicularly the upper surface of the scintillator ($\theta_z = 0$, thus $cos^2(\theta_z) = 1$) and to travel the whole thickness of the scintillator. Therefore, we expect a peak in the energy distribution at about 12 MeV. This peak can be seen clearly in figure 5.12.

The right tail is the energy released by muons that reach the scintillator obliquely, whose tracks inside the scintillator were longer than the scintillator thickness. The energies on the left of the peak are caused by muons that reached the scintillator sideways and traverse a smaller portion of the cube. The shorter and longer tracks can be identified also in figure 5.11. To verify this, another simulation of a 4 GeV monochromatic muons source perpendicularly falling through the scintillator surface ($\theta_z = 0$) has been produced, so to eliminate muons coming obliquely. The distribution of the energy deposition thus obtained has been superimposed to the previous graph. It is clear that the left tail is missing and the right tail has shrunk (figure 5.12 (b)).

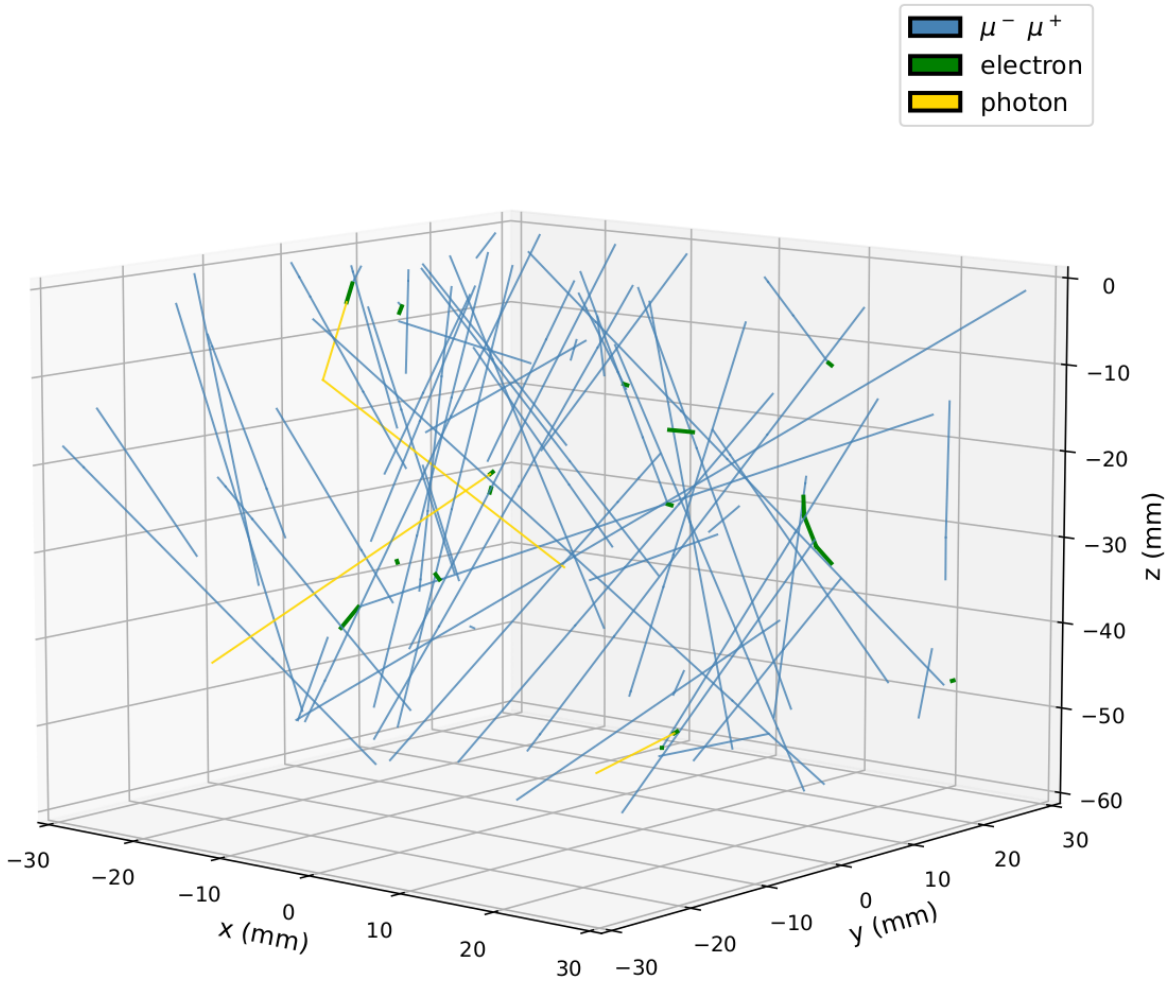


Figure 5.11: Monte Carlo simulation of cosmic muons trough the scintillator.

### 5.3.3 Comparison of Monte Carlo and experimental data

As already mentioned, the same experimental setup has been assembled twice: signal peak amplitudes were measured inside the scintillator (Section 5.2.2) and muons deposited energy was estimated with a Monte Carlo simulation (Section 5.3.2).

Therefore, the distributions shown in figures 5.8 and 5.12 (a) are expected to be similar. However, a structure at approximately 12 MeV is present only in figure 5.12 (a), whereas is not visible in figure 5.8. The lack of that peak in figures 5.8 could be attributed to a poor energy resolution of the system. To test this hypothesis, a convolution with a Gaussian distribution was performed. In the present case, different values of the standard deviation $\sigma$ were used to enlarge the initial distribution, to mimic different energy resolutions. Figure 5.13 displays the outcome of the initial distribution

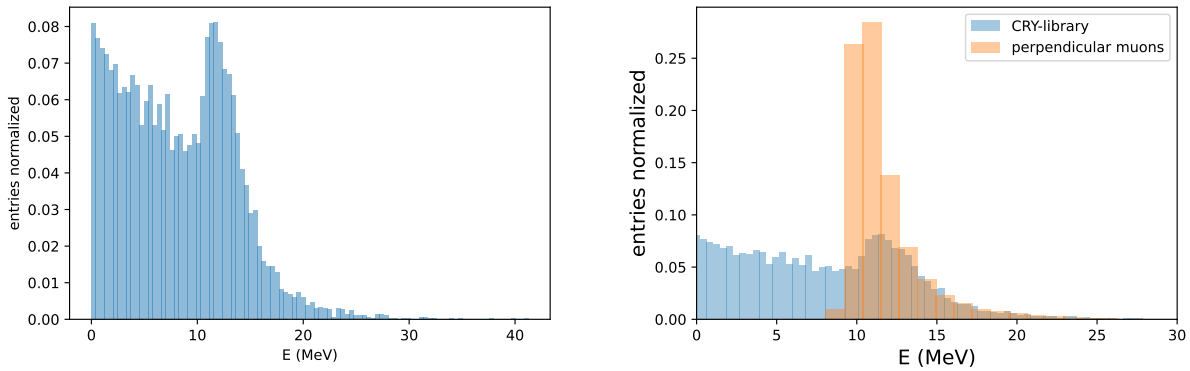


(a) (b)

Figure 5.12: (a) Monte Carlo simulations of muons energy deposition inside the scintillator. (b) Comparison of CRY source with perpendicular shower. Lower energy deposition is caused by muons that pass only a portion of the scintillator surface.

convoluted with three different $\sigma$. It can be noticed that with the increasing of $\sigma$ and therefore the worsening of energy resolution, the peak is lowered and the shape becomes wider.

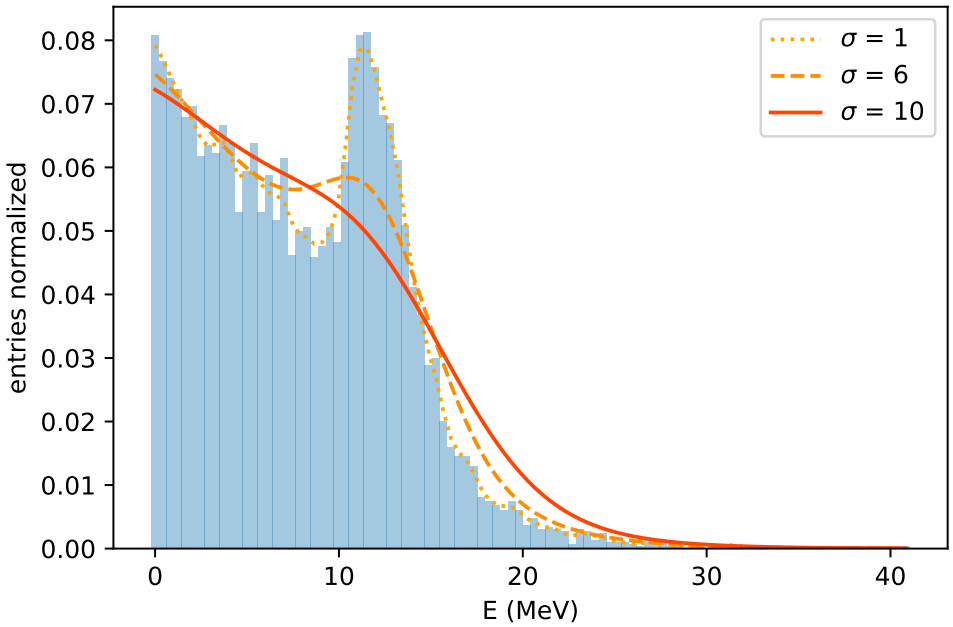


Figure 5.13: Convolution of the initial energy distribution with three Gaussian with different standard deviations.

# Conclusions

Numerous basic and applied research fields would benefit from a neutron detector with tracking capabilities. The quest for novel detection systems in the field of neutron detection clearly calls for the study on innovative setups. The proposed detector concept RIPTIDE has been conceived for the detection of fast neutrons using recoil proton track imaging technique (RPTI). From a three-dimensional reconstruction of recoil-protons, RIPTIDE aims to reconstruct neutron tracks, and therefore its momentum.

In this thesis, the working principle of RIPTIDE detector were described, and two preliminary studies for the construction of this novel device were presented.

First, neutron interaction probabilities inside the scintillator were studied via Monte Carlo simulations. Five monochromatic neutron sources were simulated, and the probability of neutron-to-proton single or double scattering were estimated. A threshold at low energies was imposed, in order to take into account spatial resolution limits of the optical system. Higher efficiencies have been found, particularly for single scattering, if compared with other RPTI techniques in literature. Then, the number of recoil protons escaped from the scintillator with a residual amount of kinetic energy was estimated. Because it is not possible to measure their energy, these protons cannot be used for neutron detection. In the energy range of RIPTIDE, this effect is mostly negligible. Furthermore, the effect of competing reactions inside the scintillator was taken into account. In particular, the interaction of a neutron with carbon ions and subsequently with protons is indistinguishable from a neutron-to-proton single scattering. A similar situation applies to double scattering. In the energy region of interest, it has been found that single scattering misclassification was lower than 10%. The misclassification is slightly higher for double scattering.

On Chapter 5, it has been studied the coupling of the scintillator with a silicon photomultiplier. To experimentally characterize the setup, cosmic muons have been used. The SiPM-scintillator system has been wrapped with a photo-absorbing material, Cinefoil, and the SiPM signal was compared with the one obtained with a reflective wrapping. Moreover, the distortions of the signal shape caused by a signal amplifier were measured. Pulse shape analysis of the signal from the two setups were performed to evaluate if scintillation light is correctly detected and if the pulse was sufficiently fast to allow real-time neutron detection. Cinefoil signals resulted to be lower in amplitude

but faster when compared to signals obtained with Teflon setup. Amplifier distortions were small, in particular for Cinefoil signals. Then, the experimental data have been compared with Monte Carlo simulations built with Geant4 toolkit. After an evaluation of the library that was used to generate the source, the energy distribution inside the scintillator was obtained. Finally, it was possible to compare the experimental peak amplitude distribution with the energy distribution of the simulation.

In summary, the goal of RIPTIDE is to develop an innovative neutron detection method. If successful, this novel approach might be a pioneering technological advancement for a number of scientific, medical, and industrial applications.

# Ringraziamenti

Alcuni studenti affermano, non sempre a torto, di essere loro stessi gli unici da ringraziare per aver portato a termine la propria tesi. Io di certo non posso identificarmi con questa affermazione. Pertanto, come è opportuno, mi accingo a ringraziare chi ha permesso che arrivassi a questo punto quantomeno sana e salva. Essento la lista molto lunga (manco fossi Benigni agli Oscar), avrei potuto risparmiare inchiostro e fare un elenco puntato di una sola paginetta, ma dato che non sono stata dotata del dono della sintesi (e non mi va), mi dilungherò per le prossime due o tre pagine almeno. E poiché i ringraziamenti, come l'appendice, non li legge mai nessuno, non mi curerò dei pochi limiti che ho cercato di impormi nella stesura della tesi e mi sono permessa una serie di licenze rispetto alle regole più stringenti proprie della letteratura scientifica (Con ciò non voglio far credere di ritenere il mio lavoro impeccabile dal punto di vista stlistico, s'intende). Fatta questa premessa, possiamo incomiciare.

É d'uopo cominciare col ringraziare relatore e correlatore: il Prof.[2] Cristian Massimi [54] e il Dott. Patrizio Console Camprini [63]. Li ringrazio, innanzitutto, per la pazienza nel sopportare gli errori spesso reiterati e per la minuzia nelle correzioni, assolutamente non dovuta ma sicuramente molto gradita (alcune pagine di tesi erano talmente fitte di correzioni che non si vedeva più il bianco del foglio). In ultimo (but not least), li ringrazio per tutto quello che sono riuscita ad imparare in questi mesi, soprattutto che il Knoll dà la risposta alla domanda fondamentale sulla vita l'universo e tutto quanto [42], a come usare git senza distruggere il lavoro altrui, all'importanza di essere precisi (questa è decisamente una skill ancora da acquisire) sia nella programmazione sia nella scrittura.

Passiamo oltre. Non posso non ringraziare poi i professori Mauro Villa [35] e Roberto Spighi [41]. Il primo perché, delle poche parole scambiare (rispetto ai miei standard), non ne ho sentita una che non avesse lo scopo di aiutarmi a migliorare; il secondo per la sua disponibilità nell'interrompere qualunque delle proprie attività, anche se importanti, per dare una mano a chiunque bussasse alla porta del suo ufficio chiedendo qualcosa.

Avanti. Non è possibile non ringraziare tutti gli inquilini dell'ufficio ~~Atlas~~FOOT:

[2] n.d.r. (che poi sono sempre io). Ho assegnato ad ognuno il proprio titolo, sperando di non averne sbagiato nessuno. Anche se così fosse, penso (e credo che su questo siamo tutti d'accordo) che la stima non si dimostra mettendo il titolo corretto, bensì con i fatti.

Dott. Riccardo Ridolfi [56], che ha sempre l'immagine perfetta per qualunque esigenza (vedi figura 1.1), Prof, Matteo Franchini [40], che sono sicura che apprezzerà l'opera a lui dedicata, Dott. Roberto Zarrella [48] che è l'unica persona a cui ho visto brillare gli occhi parlando in un programma in C++ e Dott. Giacomo Ubaldi [15], che è forse colui che è uscito più provato dall'avermi incontrato (tranquillo... a breve me ne vado). Metto nello stesso ufficio anche la Dott.ssa Sofia Colombi [64], un punto di riferimento costante e fonte inesauribile di consigli anche ora che non lavora più all'università. Non posso poi non ringraziare (soprattutto per la pazienza) le mie due compagne di banco Dott.ssa Lucia Salvi [5] e Dott.ssa Chiara D'Orazio [65]. Attendo con ansia il momento (molto prossimo) in cui Chiara sbroccherà.

Come quando a 'La Posta di Sonia' si salutava 'tutti quelli che mi conoscono' (citazione solo per i laziali), voglio ringraziare tutto il resto del corridoio [43], chi per un caffè offerto, chi per una bustina di thé prestata, chi per un consiglio, chi per una (o più plausibilmente più) chiacchiere; chi in quel corridoio ci lavora da anni e chi ci è passato solo una volta.

Infine vorrei ringraziare anche un pochino me stessa [17], perché se è uscito un lavoro discreto il merito è anche in parte mio.

# Appendix A

# Heavy charged particles interactions with matter: From Bethe Bloch formula to Bragg curve

An in-depth description of the behavior of heavy charged particles in matter has a triple utility in this thesis: (1) to understand hadrontherapy mechanism (Section 1.1) and (2) to understand the behaviour of recoil protons and (3) muons inside the plastic scintillator (Section 3) and 5).

In the interaction of heavy charged particles with matter, by far the most dominant interaction is with nuclear electrons, reaching values of cross sections of $10^6$ barns. These large values make the treatment in terms of cross section unnecessarily complicated. For this reason it is customary to describe the phenomenon in terms of energy loss in the medium ($\frac{dE}{dx}$).

Energy loss due to electromagnetic interactions is described by the Bethe Bloch formula, firstly introduced by Hans Bethe in 1930:

$$-\frac{dE}{dx} = \frac{\rho Z}{A}\frac{4\pi N_A m_e c^2}{M_u}\left(\frac{e^2}{4\pi\epsilon_0 m_e c^2}\right)^2 \frac{z^2}{\beta^2}\left[ln\left(\frac{2m_e c^2\beta^2}{I(1-\beta^2)}\right) - \beta^2 - \frac{\delta}{2} - \frac{C}{Z}\right] \quad \text{(A.1)}$$

In this formula $\rho$, $Z$ and $A$ are respectively density, atomic number and atomic weight of the absorbing material. Another medium parameter is the average ionization potential ($I$). On the other hand, the beam characteristics is defined by the particle beam atomic number ($z$) and speed ($\beta$). $\delta/2$ and $C/Z$ are respectively density and shell correction. The first one has an important role at higher energies, the other corrects the formula at lower ones. The other quantities are constants: Avogadro's number ($N_A$), electron mass ($m_E$), light speed ($c^2$) and nucleon mass ($M_U$). .

In the following sketch (A.1) we can underline the main features of this formula.

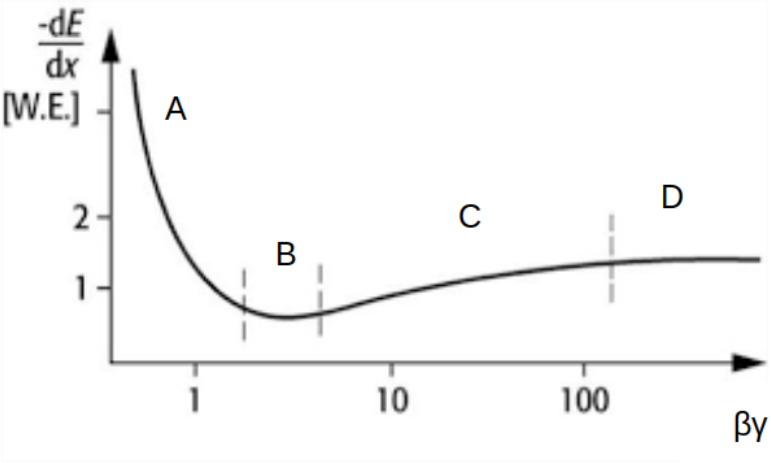


Figure A.1: Sketch of energy loss with respect to $\beta\gamma$. After a fast decrease (A) energy loss reaches its minimum (B). Then a logarithmic rise (C) and a subsequent plateau (D) can be seen.

At lower energies ($\beta\gamma < 1$) energy loss decreases as $\frac{1}{\beta^2}$ (region A). The subsequent energy range (B), where $\beta\gamma \sim 3-4$ is where the energy loss is at its minimum. Particles in this energy range are called minimum ionizing particles (MIP) and are able to travel large depths of matter without losing too much energy. At higher particle velocities ($\beta\gamma > 4$), relativistic effects take place. Therefore, energy loss in this range experiences a so called relativistic rise. At even faster speeds (D), it is possible to observe a curve flattening known as Fermi plateau.

We can also refer to $\frac{dE}{dx}$ as the stopping power of the material with respect to the particle of the beam: the lenght that a specific particle beam travels inside a certain material depends on the beam itself and also by the medium characteristics.

For this thesis, we need to focus on the trend of energy loss at lower energies and at the minimum of ionization. To understand the behaviour of the end of the energy loss at low energies is useful both to figure out Ion Beam therapy principle (Section 1.1) and the behaviour of recoil protons inside RIPTIDE scintillator (Chapter 3). On the other hand, cosmic muons that reach sea level (Chapter 5) can be considered are at the minimum of ionization.

With regard to minimum ionizing particles (MIP), it worth to mention the fact that these particles lose only a little of their energy (for muons it is about 2 $MeVcm^2/g$) and thus, travel trough large thicknesses of the material unstopped.

A more complex analysis should be done for particles less energetic than MIPs. We saw that at these energy ranges, $\frac{dE}{dx}$ goes as $\frac{1}{\beta^2}$. That means that the slower the particle goes, the larger will be the energy released in the medium.

By losing its energy, however, a particle will also reduce its speed until it is completely

stopped by the medium. A particle being slowed down by its medium, therefore, will lose progressively increasing amount of energy, and releases the greatest amount of energy at the end of the path.

reaching the maximum of its energy lost at the end of its path. This peculiar behaviour takes the name of Bragg curve and is shown in figure A.2 and its characteristic peak is called Bragg peak.

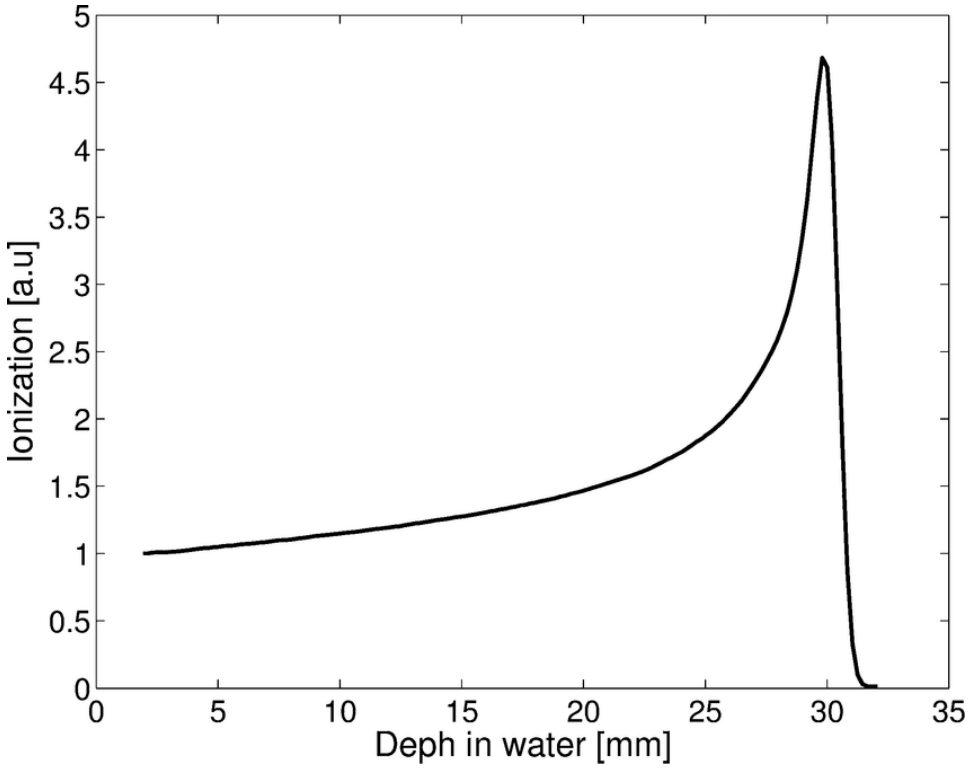


Figure A.2: Bragg curve. The maximum of the energy loss is at the end of particle path. [10]

An information that is useful to extract from the interaction of charged particles with matter is the average length that the particles travel through a certain medium (*Range*).

From the value of initial energy it is possible to link a particle range with its energy. This is because:

$$R = \int_0^R dx = \int_{E_0}^0 \frac{dE}{-\frac{dE}{dx}} = \int_0^{E_0} \frac{dE}{\frac{dE}{dx}} \tag{A.2}$$

By solving this integral we find, in case of protons, the general relation [29]:

$$R(E_0) = \alpha E_0^p \tag{A.3}$$

where $\alpha$ depends on the material and $p$ depends on particle energy. RIPTIDE detection mechanism aims to exploit this relation: by measuring the length of recoil proton tracks (proton range) it is possible to obtain proton initial energy, that is needed to estimate neutron energy.

Moreover, the range of a generic charged particle of certain charge and mass (Z,M) given proton energy is given by the formula [29]:

$$R_{Z,M}(E) = \frac{M R_p(E/M)}{Z^2} \tag{A.4}$$

These last relations are fundamental because they say that, if the initial Energy is known, also its range is. Eq. A.4 shows that the range for a generic particle is inversely proportional to $Z^2$. This implies that if we e.g. consider a carbon ion ($^{12}C$), with a mass M = 12 and charge Z = 6, it will have a range that is $(12/6^2) = 0.33$ times that of a proton with the same energy.

# Appendix B

# 90° criterion

Here we describe a particular feature of classical mechanics elastic collision between particles of equal masses. In nuclear scattering, for the energies involved in RIPTIDE (up to 20 MeV), we can assume neutrons and protons as classical particles and the relativistic and quantum effects can be neglected.

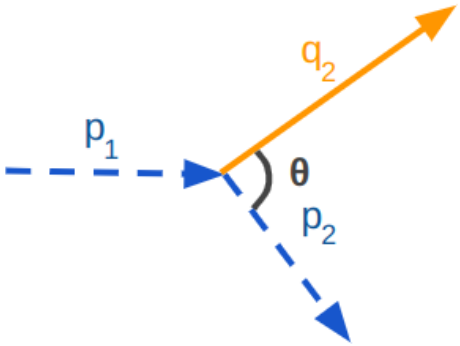


Figure B.1: Sketch of elastic collision of a single scattering between particles of equal masses. $\vec{p_1}$, $\vec{p_2}$ are initial and final momentum of particle $p$ and $\vec{q_2}$ is the final momentum of particle $q$. Particle $q$ is initially at rest ($\vec{q_1} = 0$).

In classical mechanics elastic collisions, both momentum ($p = m\vec{v}$) and kinetic energy ($K = \frac{1}{2}mv^2$) are conserved.

By imposing the momentum conservation with the notation as in B.1, we have:

$$\vec{p_1} + \vec{q_1} = \vec{p_2} + \vec{q_2}$$

or

$$m_1\vec{v_{1p}} + m_2\vec{v_{1q}} = m_1\vec{v_{2p}} + m_2\vec{v_{2q}}$$

but particle $q$ is initially at rest, therefore $\vec{q_1} = 0$. We are also assuming that the two particles have equal masses, therefore $m_p = m_q = m$:

$$m\vec{v_{1p}} = m \cdot (\vec{v_{2p}} + \vec{v_{2q}})$$

or

$$\vec{v_{1p}} = (\vec{v_{2p}} + \vec{v_{2q}})$$

By applying the scalar product of a vector for itself, we have that $\vec{v} \cdot \vec{v} = v^2$. So,

$$\vec{v_{1p}} \cdot \vec{v_{1p}} = v_{1p}^2 = (\vec{v_{2p}} + \vec{v_{2q}}) \cdot (\vec{v_{2p}} + \vec{v_{2q}}) = v_{2p}^2 + v_{2q}^2 + 2(\vec{v_{2p}} \cdot \vec{v_{2q}})$$

We have therefore:

$$v_{1p}^2 = v_{2p}^2 + v_{2q}^2 + 2(\vec{v_{2p}} \cdot \vec{v_{2q}}) \tag{B.1}$$

We can now impose energy conservation ($K_i = K_f$):

$$\frac{1}{2}mv_{1p}^2 = \frac{1}{2}m(v_{2p}^2 + v_{2q}^2)$$

Therefore,

$$v_{1p}^2 = v_{2p}^2 + v_{2q}^2 \tag{B.2}$$

The speeds in equations B.1 and B.2 must be the same. This implies that the dot product of B.1 must be equal to zero. The only way in which the scalar product between two non-zero vectors can be equal to zero is that they are mutually perpendicular. Therefore, we have to assume that the angle $\theta$ in figure is always a right angle. This must be true also in the case of proton neutron scattering because we can assume with a good approximation that they have equal mass.

In case of non-relativistic elastic scattering between a proton and a neutron, the two particles will be emitted at an angle of $\frac{\pi}{2}$.

Q.E.D.

# Bibliography


[1] Nuclear Energy Agency. `https://www.oecd-nea.org/jcms/pl_39910/janis`.

[2] et al. Agostinelli, Sea. Geant4—a simulation toolkit. *Nuclear instruments and methods in physics research section A: Accelerators, Spectrometers, Detectors and Associated Equipment*, 506(3):250–303, 2003.

[3] et al. Alberts, WG. Neutron dosimetry. *Radioprotection*, 31(1):37–65, 1996.

[4] AV Alevra and DJ Thomas. Neutron spectrometry in mixed fields: multisphere spectrometers. *Radiation Protection Dosimetry*, 107(1-3):33–68, 2003.

[5] Johann Sebastian Bach. *Suite per Violoncello n. 1 in Sol Maggiore, BWV 1007*.

[6] Giuseppe Battistoni, Marco Toppi, and Vincenzo Patera. Measuring the impact of nuclear interaction in particle therapy and in radio protection in space: the foot experiment. *Frontiers in Physics*, 8:568242, 2021.

[7] et al. Bravar, Ulisse. Atmospheric neutron measurements with the sontrac science model. In *IEEE Nuclear Science Symposium Conference Record, 2005*, volume 2, pages 634–638. IEEE, 2005.

[8] P Console Camprini, F Leone, C Massimi, A Musumarra, MG Pellegriti, C Pisanti, F Romano, R Spighi, N Terranova, and M Villa. A proton-recoil track imaging system for fast neutrons: the riptide detector. *arXiv preprint arXiv:2210.17431*, 2022.

[9] James Chadwick. Possible existence of a neutron. *Nature*, 129(3252):312–312, 1932.

[10] et al. Cirrone, GAP. A 62-mev proton beam for the treatment of ocular melanoma at laboratori nazionali del sud-infn. *IEEE Transactions on Nuclear Science*, 51(3):860–865, 2004.

[11] et al. Combe, Rodolphe. Conception of a new recoil proton telescope for real-time neutron spectrometry in proton-therapy. In *EPJ Web of Conferences*, volume 170, page 09001. EDP Sciences, 2018.

[12] Saint-Gobain Crystals. bc-400, bc-404, bc-408, bc-412, bc-416 premium plastic scintillators. *Saint-Gobain Crystals, Nemours*, 2005.

[13] et al. De Marzi. Exploiting the full potential of proton therapy: An update on the specifics and innovations towards spatial or temporal optimisation of dose delivery. *Cancer/Radiothérapie*, 24(6-7):691–698, 2020.

[14] et al. De Nolfo, GA. Solar neutron tracking (sontrac) concept. In *36th International Cosmic Ray Conference (ICRC2019)*, volume 36, page 1074, 2019.

[15] Claude Debussy. *La cattedrale sommersa*.

[16] et al. Deveaux, M. Observations on mimosis-0, the first dedicated cps prototype for the cbm mvd. *Nuclear Instruments and Methods in Physics Research Section A: Accelerators, Spectrometers, Detectors and Associated Equipment*, 958:162653, 2020.

[17] Paul Dukas. *L'apprendista stregone*.

[18] D.A. Brown et al. Endf/b-viii.0: The 8th major release of the nuclear reaction data library with cielo-project cross sections, new standards and thermal scattering data. *Nuclear Data Sheets*, 148:1–142, 2018. Special Issue on Nuclear Reaction Data.

[19] et al. Farah, J. Measurement of stray radiation within a scanning proton therapy facility: Eurados wg9 intercomparison exercise of active dosimetry systems. *Medical physics*, 42(5):2572–2584, 2015.

[20] et al. Filipenko, Mykhaylo. Three dimensional photograph of single electron tracks through a scintillator. *arXiv preprint arXiv:1404.3841*, 2014.

[21] Thomas K Gaisser, Ralph Engel, and Elisa Resconi. *Cosmic rays and particle physics*. Cambridge University Press, 2016.

[22] et al. Giacometti, V. Characterisation of the mondo detector response to neutrons by means of a fluka monte carlo simulation. *Radiation Measurements*, 119:144–149, 2018.

[23] Peter KF Grieder. *Cosmic rays at Earth*. Elsevier, 2001.

[24] et al. Gunzert-Marx. Secondary beam fragments produced by 200 mev u- 1 12c ions in water and their dose contributions in carbon ion radiotherapy. *New journal of physics*, 10(7):075003, 2008.

[25] CA Hagmann, DJ Lange, and DM Wright. Monte carlo simulation of proton-induced cosimc ray cascades in the atmosphere. Technical report, Lawrence Livermore National Lab.(LLNL), Livermore, CA (United States), 2007.

[26] et al. Hagmann, Chris. Cosmic-ray shower library (cry). *Lawrence Livermore National Laboratory document UCRL-TM-229453*, 2012.

[27] HAMAMATSU. `https://www.hamamatsu.com/eu/en/product/optical-sensors/mppc/mppc_mppc-array/S13360-3025CS.html`.

[28] et al. Hu, Jing. Recoil-proton track imaging as a new way for neutron spectrometry measurements. *Scientific Reports*, 8(1):1–8, 2018.

[29] Glenn F Knoll. *Radiation detection and measurement*. John Wiley & Sons, 2010.

[30] Gerhard Kraft. Tumor therapy with heavy charged particles. *Progress in particle and Nuclear Physics*, 45:S473–S544, 2000.

[31] Kenneth S Krane. *Introductory nuclear physics*. John Wiley & Sons, 1991.

[32] et al. Langford, TJ. Development and characterization of a high sensitivity segmented fast neutron spectrometer (fans-2). *Journal of Instrumentation*, 11(01):P01006, 2016.

[33] William R Leo. *Techniques for nuclear and particle physics experiments: a how-to approach*. Springer Science & Business Media, 2012.

[34] Ute Linz. *Ion beam therapy: fundamentals, technology, clinical applications*. Springer Science & Business Media, 2011.

[35] Gustav Mahler. *Sinfonia n. 1 in Re maggiore*.

[36] VN Manokhin. Brond: Ussr evaluated neutron data library. Technical report, International Atomic Energy Agency, 1991.

[37] C Massimi, A Musumarra, F Leone, MG Pellegriti, F Romano, R Spighi, and M Villa. "riptide"—an innovative recoil-proton track imaging detector. *Journal of Instrumentation*, 17(09):C09026, 2022.

[38] Cristian Massimi, Nikolas Patronis, and Agatino Musumarra. Measurement of the neutron-neutron scattering length at the cern n_tof facility. Technical report, 2020.

[39] et al. Miller, Richard S. Sontrac: An imaging spectrometer for mev neutrons. *Nuclear Instruments and Methods in Physics Research Section A: Accelerators, Spectrometers, Detectors and Associated Equipment*, 505(1-2):36–40, 2003.

[40] Wolfgang Amadeus Mozart. *Difficile lectu K 559*.

[41] Wolfgang Amadeus Mozart. *Il flauto magico K. 620. Ouverture*.

[42] Wolfgang Amadeus Mozart. *Il Guida galattica per autostoppisti (che ovviamente non è di Mozart ma volevo che capitasse al numero 42).*

[43] Wolfgang Amadeus Mozart. *Le nozze di Figaro. Esci ormai, garzon malnato.*

[44] Agatino Musumarra, Franco Leone, Cristian Massimi, Maria Grazia Pellegriti, Francesco Romano, Roberto Spighi, and Mauro Villa. Riptide: a novel recoil-proton track imaging detector for fast neutrons. *Journal of Instrumentation*, 16(12):C12013, 2021.

[45] Nooelec. *LaNA HF Barebones - Ultra Low-Noise LF, MF and HF Amplifier (LNA) Module. 50kHz-150MHz Frequency Capability w/ Bias-Tee, USB and DC Power Options*, 2022.

[46] nTOF. `https://ntof-exp.web.cern.ch/`.

[47] Domenico Pacini. La radiazione penetrante alla superficie ed in seno alle acque. *Il Nuovo Cimento (1911-1923)*, 3(1):93–100, 1912.

[48] Niccolò Paganini. *Capriccio n. 24 in La minore.*

[49] et al. Pietropaolo, A. Neutron detection techniques from $\mu$ev to gev. *Physics Reports*, 875:1–65, 2020.

[50] BC Rastin. An accurate measurement of the sea-level muon spectrum within the range 4 to 3000 gev/c. *Journal of Physics G: Nuclear Physics*, 10(11):1609, 1984.

[51] Donald V Reames. *Solar energetic particles: a modern primer on understanding sources, acceleration and propagation.* Springer Nature, 2021.

[52] Claire-Anne Reidel. *Applications for CMOS pixel sensors in ion-beam therapy.* PhD thesis, Université de Strasbourg, 2020.

[53] Ivan Reitman. Ghostbusters, 1984.

[54] Gioacchino Rossini. *Il Barbiere Di Siviglia. Overture.*

[55] et al. Ryan, James M. A scintillating plastic fiber tracking detector for neutron and proton imaging and spectroscopy. In *1999 IEEE Nuclear Science Symposium. Conference Record. 1999 Nuclear Science Symposium and Medical Imaging Conference (Cat. No. 99CH37019)*, volume 1, pages 483–488. IEEE, 1999.

[56] Camille Saint Saens. *Introduzione e Rondò Capriccioso op. 28.*

[57] Robert Serber. Nuclear reactions at high energies. *Physical Review*, 72(11):1114, 1947.

[58] Sony. https://www.sony.it/electronics/obiettivi-fotocamera/sel30m35.

[59] Eljen Technology. General purpose plastic scintillators ej-200, ej-204, ej-208, ej-212, 2016.

[60] Francesco Tommasino and Marco Durante. Proton radiobiology. *Cancers*, 7(1):353–381, 2015.

[61] AS Tremsin and JV Vallerga. Unique capabilities and applications of microchannel plate (mcp) detectors with medipix/timepix readout. *Radiation Measurements*, 130:106228, 2020.

[62] et al. Valle, SM. The mondo project: A secondary neutron tracker detector for particle therapy. *Nuclear Instruments and Methods in Physics Research Section A: Accelerators, Spectrometers, Detectors and Associated Equipment*, 845:556–559, 2017.

[63] Ludwig van Beethoven. *Sinfonia n. 7 in La maggiore Op. 92.*

[64] Antonio Vivaldi. *Griselda. Agitata da due venti.*

[65] Antonio Vivaldi. *Sonata op. 1 n. 12. La Follia.*

[66] V.Patera. http://arpg-serv.ing2.uniroma1.it/patera/didattica/fis_mod/trasp_riv/Tipi/PM/MCP.html.

[67] Nick Waltham. Ccd and cmos sensors. In *Observing photons in space*, pages 423–442. Springer, 2013.

[68] Zhehui Wang and Christopher L Morris. Tracking fast neutrons. *Nuclear Instruments and Methods in Physics Research Section A: Accelerators, Spectrometers, Detectors and Associated Equipment*, 726:145–154, 2013.

[69] ZWO. https://astronomy-imaging-camera.com/product/asi294mm-pro.